Effect of Cerium addition on the electrochemical behaviour of carbon alloyed Fe_3Al based intermetallics

By

Sriram Srinivasan

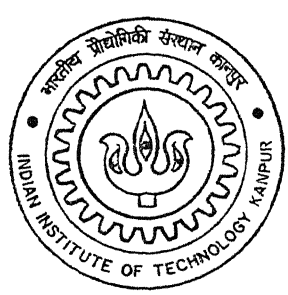

DEPARTMENT OF MATERIALS AND METALLURGICAL ENGINEERING

INDIAN INSTITUTE OF TECHNOLOGY KANPUR

FEBRUARY, 2004

Effect of Cerium addition on the electrochemical behaviour of carbon alloyed Fe_3Al based intermetallics

A Thesis submitted

In partial Fulfillment of the Requirements
For the Degree of

MASTER OF TECHNOLOGY

by

Sriram Srinivasan
(Y120618)

to the

DEPARTMENT OF MATERIALS AND METALLURGICAL ENGINEERING

INDIAN INSTITUTE OF TECHNOLOGY, KANPUR
INDIA 208016

February 2004

Certificate

This is to certify that the present thesis work entitled **"EFFECT OF CERIUM ADDITION ON THE ELECTROCHEMICAL BEHAVIOUR OF CARBON ALLOYED Fe_3Al BASED INTERMETALLICS"**, has been carried out by Sriram Srinivasan, under our supervision and to the best of our knowledge it has not been submitted elsewhere for a degree

(Dr R Balasubramaniam)
Professor
Dept of Mat and Met Engg
Indian Institute of Technology,
Kanpur 208016

(Dr Sanjeev Bharagava)
Professor
Dept of Mat and Met Engg
Indian Institute of Technology,
Kanpur 208016, India

27th February 2004

Dedicated to

My wife Anuradha and my daughter Sreenidhi

ACKNOWLEDGEMENTS

I acknowledge with sincerity and deep sense of gratitude the expert guidance and continuous encouragement provided by my thesis supervisors Dr.R.Balasubramaniam and Dr.Sanjeev Bhargava.

I wish to express my sincere appreciation of the valuable help and suggestions obtained from Dr.M.N.Mungole.

I am obliged very much to Dr.R.Baligidad, Deputy Director, DMRL, Hyderabad, India for furnishing immense literature on iron aluminide alloys. I would also like to acknowledge Dr.D.Banerjee, DMRL, Hyderabad for providing the samples.

I am immensely thankful to Harish, Lab assistant for helping me in my experimental work. I am also grateful to Mr. Sairam of the glassblowing section.

I am also thankful to my friends M.Surendar, Anup Shukla, Indrani, Tapas Laha and all other friends who have helped me in various capacities throughout my thesis at IIT Kanpur.

At this juncture I would like to express my deep sense of gratitude to my wife Anuradha for her patience and moral support, courage and inspiration during this research programme.

I am indebted to IIT Kanpur for providing me the best environment to stay and do research in the most fruitful way.

Sriram Srinivasan
IIT Kanpur
28th February 2004

ABSTRACT

The effect of addition of Ce on the microstructures and electrochemical behaviour of carbon-alloyed iron aluminides was studied. The corrosion behaviour of Ce-alloyed iron aluminide has been analysed in comparison with that of non Ce-alloyed iron aluminides. These alloys were obtained from Defence Metallurgical Research Laboratory, Hyderabad. They possessed the composition (in atom percent), Fe-20.0Al-2.0C (referred as ESR74), Fe-18.5Al-3.6C (referred as ESR127) and Fe-19.2Al-3.3C-0.07Ce (referred as ESR137). The composition of these alloys in weight percent, were Fe-11.0Al-0.5C (ESR137), Fe-10.5Al-0.9C (ESR127) and Fe-10.5Al-0.8C-0.2Ce (ESR137). These alloys were processed by arc induction melting and eletro-slag remelting at DMRL, Hyderabad. A mild steel of composition (in wt %) Fe-0.062C, 0.005Si, 0.006P, 0.02Ni, 0.004Co, 0.185Mn, 0.042Cr, 0.005Mo, 0.024Cu, 0.0007Ti, 0.032Al, 0.012S was also studied for comparison purpose.

The microstructures of the carbon-alloyed iron aluminides were typical two phase structures with Fe_3AlC precipitates in an Fe_3Al matrix. In the alloys ESR127 and ESR74, large bulky carbides were distributed throughout the matrix with many smaller precipitates interspersed in between. In the Ce-added alloy, ESR137, the carbide grain sizes were finer, and they were uniformly distributed throughout the matrix. Therefore, the addition of Ce to the iron aluminides affected the morphology of the carbides. The effect of Ce on the microstructure has been explained by considering the known effect of Cerium in modifying carbide/graphite morphologies in cast iron. X ray diffraction patterns confirmed that the presence of carbon leads to the formation of Fe_3AlC precipitates in the matrix. The alloyed intermetallics did not exhibit any additional diffraction peaks apart from the peaks that were obtained for the base intermetallics. Therefore, Ce additions essentially enter into the solid solution in Fe_3Al matrix or in the interfacial region between the carbide and the matrix.

The electrochemical polarisation behaviour of the alloys was evaluated in freely aerated 0.5N H_2SO_4 (pH=0.74) and borate buffered (pH=7.6) solutions. The free corrosion potential (FCP) was stabilized before conducting polarisation experiments. The FCP of the intermetallics stabilized in the range of -0.50V to -0.54V vs SCE. The nature of stabilization curve for the Ce-alloyed intermetallic ESR137 was slightly different when

compared to the non Ce-alloyed intermetallics. This indicated subtle differences in the surface condition of the alloys on immersion in the electrolyte.

Electrochemical polarization studies indicated that all the three aluminides exhibited active-passive behaviour in the acidic solution (0.5N H_2SO_4) whereas they exhibit stable passivity in pH=7.6 buffered solution (1.5N H_3BO_3 + 0.1N $Na_2B_4O_7.10H_2O$ + 0.01N KNO_3). On comparison of the passivation parameters of ESR127 and ESR74 alloys,it was observed that the critical current density $i_{crit,}$ increased with the increase in carbon addition. However the other passivation parameters were not significantly different, and generally comparable. This is reasonable because the carbon contents are not significantly different and moreover the carbide distribution in the alloys was similar.

On comparing the passivation parameters of the Ce-alloyed iron aluminide (ESR137) with the non Ce alloyed iron aluminides (ESR74 and ESR127) the most important difference observed was the lower passive range in the Ce-alloyed aluminide. The polarisation behaviour of all the sections of the Ce-added aluminide was also understood. The passive current density $i_{pass,}$ for the rolling plane and the long transverse plane were lower when compared to the non Ce-added alloys. This indicates that the addition of Ce influenced the nature of the passive film.

Corrosion rates were determined by short term immersion test and long term immersion tests. In the case of the non Ce added samples ESR74 and ESR127, the initial rate of corrosion was high, and, thereafter, the corrosion rate decreased and was almost constant. However for the Ce-alloyed aluminide ESR137 the corrosion rates were almost constant throughout the experiment period and lower corrosion rates were observed for this alloy. The corrosion rates were also estimated using Tafel extrapolation technique. The results agreed with the corrosion rates determined by the weight loss method. Modifications in the surface film by the addition of Ce has been suggested to explain the lower corrosion rates observed with the Ce additions.

The effect of Ce on the corrosion of carbon-alloyed intermetallics can be summarised as follows: The initial fast rate of corrosion of matrix may lead to Ce enrichment on the surface. Ce enrichment probably induces a more protective film formation on the surface. Therefore, the corrosion rate is lowered. This effect becomes more apparent with increasing immersion time.

CONTENTS

List of Figures

List of Tables

CHAPTER 1

INTRODUCTION

1.1 Intermetallics

Ordered intermetallics constitute a unique class of advanced materials that form long range ordered crystal structure below a critical temperature termed as critical ordering temperature (T_c) [1]. These intermetallics usually exist in narrow or fixed compositional ranges around simple stoichiometric ratios (similar to inorganic compounds). The research on ordered intermetallic alloys was motivated by the need to develop materials possessing high specific strength for structural applications at elevated temperatures.

Intermetallics is the short and summarizing designation for the intermetallic phases and compounds which result from the combination of various metals and which form a tremenderously numerous and manifold class of materials.(Table 1). Intermetallics became a subject of scientific research during the 19^{th} century with the development of physical metallurgy and the first validated instance of intermetallic compound formation was reported by Karsten (1839) in Germany. The early work on intermetallics during the first decades of the 20^{th} century included studies of phase stabilities, phase equilibria and phase reactions in order to establish phase diagrams, as well as studies of various properties i.e chemical and electrochemical properties, mechanical properties and physical properties including magnetism and superconductivity. With respect to mechanical behaviour, it was realized that the outstanding hardness of intermetallics is accompanied by an unusual brittleness.

Intermetallics were used in 20^{th} century primarily for applications as functional materials as is exemplified in Table 1. Indeed the first industrial application relied on the special magnetic behaviour of certain phases, and respective materials developments led to Sendust, which shows outstanding magnetic properties and wear resistance and is

widely used for magnetic heads of tape recorders. [2]. In the second half of the 20th century another important application resulted from the development of new superconducting materials based on A15 compounds which are used as superconducting magnets. A third group of functional materials, the shape memory alloys, makes use of a martensitic phase transformation and has again found manifold applications during the last three decades. An important group of functional materials is formed by the III-V compounds, e.g InSb, InAs, GaAs, which have found applications in electronics and in thermoelectric power generation.

Intermetallics did not find application as structural materials in the past because of their brittleness. The only noteworthy exception is the continuing use of amalgams as dental restoratives. On the other hand various intermetallics were successfully used as strengthening second phases in conventional alloys for structural applications. Thus it was clear that intermetallics are promising materials for applications as structural materials at high temperatures because of their high hardness and stability.

Intermetallic aluminides exhibit many interesting features that project them as the candidate material for high temperature structural applications [3]. They contain enough aluminium that forms a stable thin film of aluminium oxide in the oxidizing environment. They are characterised by low densities, relatively high melting points and good mechanical properties at elevated temperatures. (Table 3). However there are two limitations in using these alloys: 1) Lack of appreciable ductility at ambient temperature and 2) Lack of adequate creep resistance at high temperatures. Efforts are being made by the scientific community to find solution to the above said demerits of these materials.

The aluminides that have attracted attention as potential candidates for high temperature applications include titanium, nickel and iron aluminides. Continuous research is in progress to develop these materials by effecting modifications on the existing systems (either by alloying or by the modifications in the processing methodology) in order to optimise their properties. Limited work has been reported by the scientific community on the effect of rare earth metals in the electrochemical behaviour of iron aluminides. In the present thesis the effect of Ce addition on the electrochemical behaviour of iron aluminides has been addressed.

Table 1 Some past and present applications of intermetallics [4]

2500 B C	Cementation	Cu_3As	Coating of bronze tools. (Egypt, Britain)
100 B C	Yellow brass	CuZn	Coins, ornamental parts (Rome)
0	High tin bronze	Cu_{31} Sn_8	Mirror (China)
600	Amalgam	Ag_2Hg_3, Sn_6Hg	Dental restoratives (China)
1500	Amalgam	Cu_4Hg_3	Dental restorative (Germany)
1505	Amalgam	Sn_8Hg	Mirror surface (Venice)
1540	Type metal	SbSn	Printing
1910	Acutal	$(Cu,Mn)_3Al$	Fruit knife (Germany)
1921	Permalloy	Ni_3Fe	High permeability magnetic alloy
1926	Permendur	FeCo(-2V)	Soft magnetic alloy
1931	Alnico	NiAl-Fe-Co	Permanent magnet material
1935	Sendust	$Fe_3(Si,Al)$	Magnetic head material
1938	Cu-Zn-Al &	CuZn-Al	Shape memory alloys
	Cu-Al-Ni	$(Cu,Ni)_3Al$	
1950	Pack aluminide	NiAl,CoAl	Surface Coating Materials
1956	Kanthal Super,	$MoSi_2$	Electric heating elements
1961	A 15 compound	Nb_3Sn	Superconductors
1962	Nitinol	NiTi	Shape memory alloy
1967	Co-Sm magnets	Co_5Sm	Permanent magnets

Table 2 Potential applications of Iron aluminides [56]

Application	Component System
Wrapping wire	Insulation wrapping for investment casting moulds.
Heating elements	Toaster, stoves, ovens,cigarette lighters and dryers
Regenerator disks	Automotive gas-turbine engines.
Hot-gas filters	Coal-gasification systems.
Tooling	Dies for superplastic forming of titanium based alloys
Automotive	Exhaust manifolds, and catalytic converters
Molten metals	Sensor sheathing material for molten Al, Zr and Cd

1.2 Iron aluminides

Iron aluminides have been of interest since 1930's when their excellent oxidation resistance was first noted [5,6]. These aluminides has exhibited attractive properties for application at elevated temperatures and severe environments over conventional structural materials like stainless steel and nickel based super alloys. Specific advantages of iron aluminides over stainless steel are, excellent sulphidation resistance, very good oxidation resistance, lower density (5400 – 6700 Kg/m^3) which is 30% of that of the commercially available high temperature materials, good wear resistance, good cavitation erosion resistance, potentially lower cost and reduced consumption of strategic element such as chromium [7]. One of the key factors in increasing the maximum use temperature is the enhanced oxidation resistance. Iron aluminides are therefore considered as candidate materials to replace stainless steels in structural parts for many industrial applications. (Table 2).

The major obstacle to their widespread use is their lack of ductility, susceptibility to brittle fracture at ambient temperatures and a rapid drop of strength and poor creep resistance at high temperatures. This poor ambient temperature ductility has been identified to be caused by an extrinsic effect, namely environmental embrittlement due to hydrogen [8]. Hydrogen is produced as a result of the reaction that happens between the fresh surfaces of iron aluminide with moisture and diffuses into the material to cause embrittlement, and therefore the poor room temperature ductility has been attributed to moisture induced embrittlement. Most of the methods proposed to tackle hydrogen embrittlement (HE) rely on restricting the entry of hydrogen into the lattice. This is achieved either by thermo mechanical treatments [9] or by surface modifications (directly by coatings [10] or indirectly by alloying with passivity inducing elements [11,12]. In addition, alloying could also be effective in enhancing other mechanical properties of these intermetallics.It has been proposed that alloying with passivity inducing elements in appropriate proportion (less than solubility limit) to iron aluminides would reduce the hydrogen liberation rates on the surface and passive layer would further hinder the diffusion of hydrogen into the intermetallic, thereby minimising hydrogen embrittlement. [11].

1.3 Carbon alloyed iron aluminides

Since carbon is known to embrittle iron aluminides and cause significant reduction in ductility, most of the earlier studies have been conducted on iron aluminide compositions with very low (0.01wt%) carbon contents. For the first time, Baligidad et al reported that addition of carbon in the range of 0.14 to 0.50 wt % significantly increases the room temperature strength of Fe-16 wt% (28 at%) Al alloys [13]. These alloys also exhibited some room temperature ductility probably due to the entrapment of hydrogen by Fe_3AlC particles, which were supposed to lower hydrogen diffusivity in these alloys and reduce the susceptibility to environmental embrittlement [13]. The increase in room temperature yield strength was attributed to the solid solution strengthening by the interstitial carbon, as well as precipitation hardening due to the presence of Fe_3AlC precipitates [14]. These carbon alloyed iron aluminides have been produced in Defence Metallurgical Research Laboratory, Hyderabad, by a combination of air induction melting and electroslag remelting (ESR). The melting practice has been described in detail in chapter 2

1.4 Objectives of the present study

The present study is specifically concerned with the evaluating and understanding of ambient temperature electrochemical behaviour of Ce containing carbon alloyed iron aluminide. An earlier study by Yangshan *et al* has reported that small additions of Ce to Fe_3Al based alloys results in enhancement of ductility and strength of iron aluminides at ambient temperature. Moreover, they also observed improvements in tensile properties and creep resistance at high temperature of 600°C. Improvements were observed at the combined addition of Ce with molybdenum, zirconium and niobium. [15]. Addition of Ce in small amounts modifies surface passive layers and therefore is expected to affect the corrosion behaviour. The present study was, therefore motivated by the need to understand the electrochemical and corrosion behaviour of Ce containing intermetallics in a relatively strong sulphuric acid environment, at ambient temperatures.

1.5 Plan of work

The following plan of work has been adopted for the thesis.

1. Procurement of carbon alloyed iron aluminide samples (both with and without Ce) from the Defence Metallurgical Research Laboratory, Hyderabad.
2. Preparation of the as received samples for microstructural characterisation.
3. Microstructural characterisation of the samples by optical and scanning electron microscopy and structural characterization by X ray diffraction.
4. Polarisation behaviour of the samples in 0.5N H_2SO_4 solution and borate buffered solution.
5. Corrosion kinetics by long term and short term immersion testing.
6. Analysis of data.

CHAPTER 2

LITERATURE REVIEW

The phase diagram and structure of iron aluminides would be briefly reviewed in the beginning of the chapter. The room temperature mechanical properties of iron aluminides would be addressed and the hydrogen embrittlement mechanism shall be highlighted. An overview of the effect of alloying elements on the mechanical properties and corrosion behaviour of the Fe_3Al based alloys is given with a special focus on the effect of Ce as an alloying element in the carbon-alloyed iron aluminides. Finally, the chapter ends with a brief survey of room temperature aqueous corrosion behavior of iron aluminides.

2.1. Fe-Al phase diagram and crystal structure

2.1.1. Iron aluminides

Ordered iron aluminides exist in relatively narrow compositional ranges around simple stoichiometric ratios. The phase diagram of Fe-Al system is shown in Figure 1. Iron aluminides based on Fe_3Al and FeAl can exist in two crystal allotropic modifications. These structures (DO_3 and B2) are both ordered BCC structures and these are presented in Figure 2. Fe_3Al can exist both in B2 and DO_3 ordered structure (depending upon the temperature) while FeAl can exist only in the B2 ordered form. The crystal structure of Fe_3AlC is perovskite and is shown in the Figure 3. Table 3 presents some typical room temperature properties and critical ordering temperatures for different allotropic modifications of Fe_3Al [7]. The room temperature strength and room temperature ductility of iron aluminides are low.

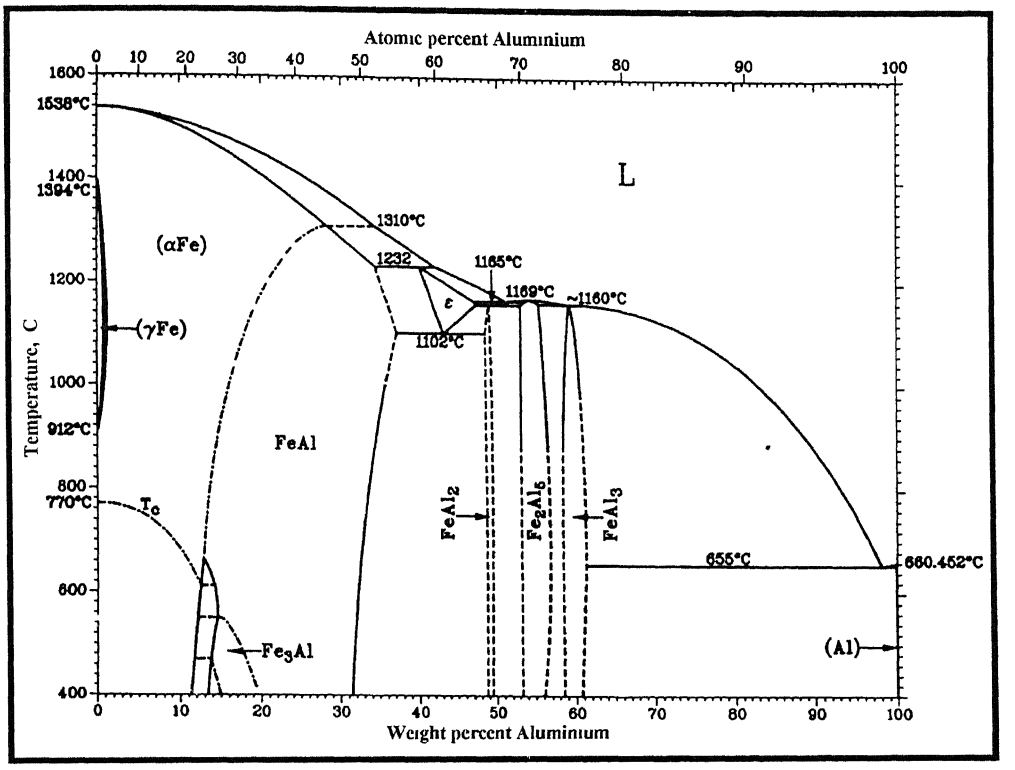

Figure 1 The Fe-Al phase diagram

Table 3 Typical room temperature properties of Iron aluminides [7]

Alloy	Crystal structure	Ordering temp °C	Melting point °C	Density (gm/cc)	Y.S. (Mpa)	Elongation (%)
Fe_3Al	DO_3	540	1540	6.72	300	3.7
Fe_3Al	B2	760	1540	6.72	380	4.1
FeAl	B2	1250	1250	5.56	360	2.2

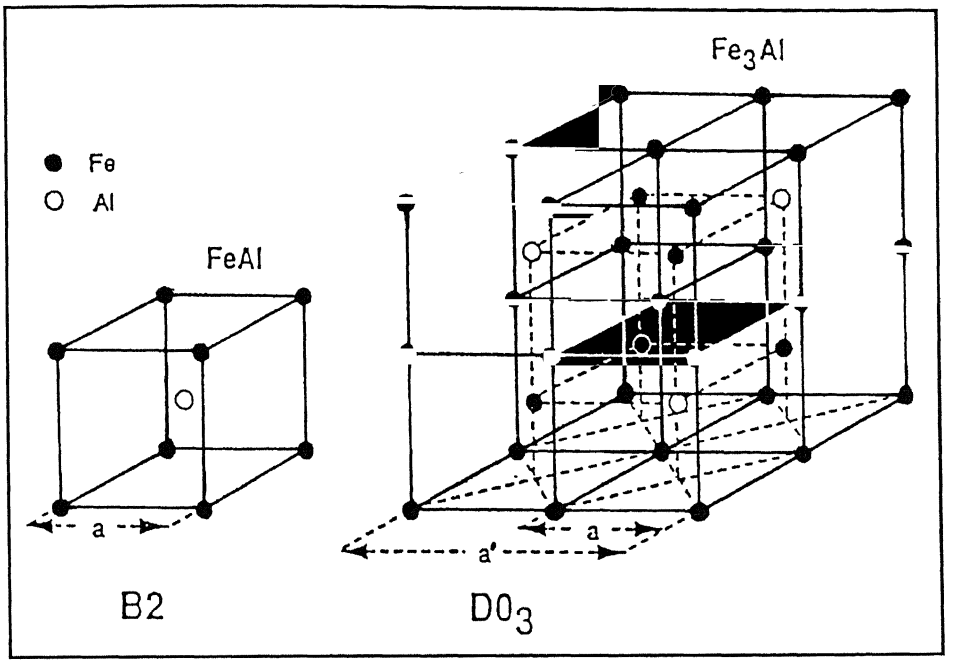

Figure 2. The DO3 and B2 ordered crystal structure of Fe_3Al and FeAl

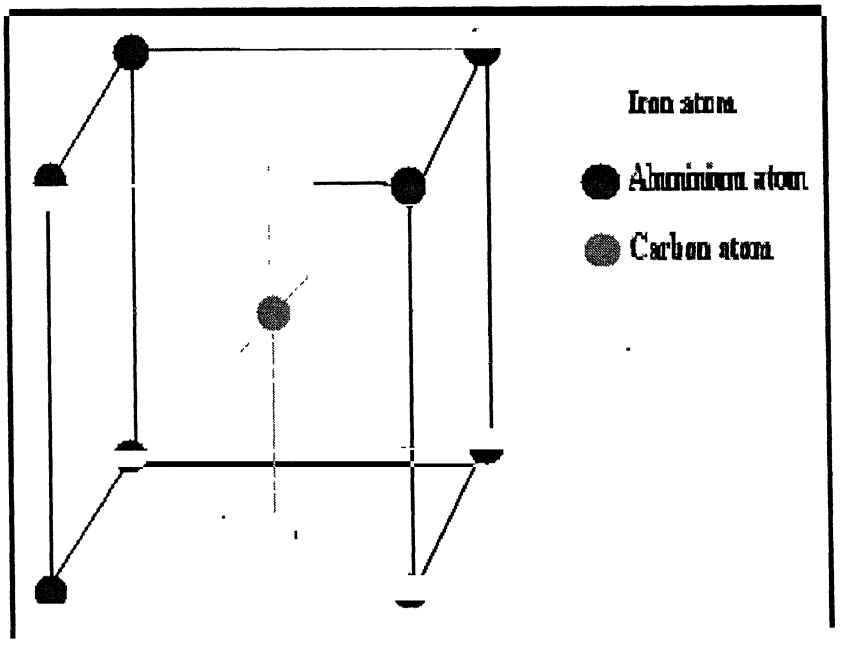

Figure 3 The perovskite crystal structure of Fe_3AlC

2.1.2. Phase equilibria in the Fe-Al-C system

The phase equilibria of Fe-Al-C system were determined from electron microprobe analysis (EPMA) of quenched samples. There are four phases of primary crystallization viz. κ, α, γ and graphite [3,16]. The extent of the field of primary crystallization of κ shown is tentative in Figure 4 . Figures 5 and 6 show the Fe-Al-C isotherms at 25°C and 1000 °C, respectively. Al increases the temperature of the graphitic eutectic reaction, as Al is a graphitic stabilizer [17]. At low carbon contents, the BCC (α) phase exists in the disordered state A2 as well as in the long range ordered states of type B2 and DO_3. At higher carbon contents, the FCC (γ) solid solution is stable and a ternary intermetallic phase, denoted by κ-phase, exists which is based on the perovskite structure [3,16 ,17].

The κ phase

κ phase can be considered as an ordered FCC arrangement of type Ll_2, with carbon atom in the octahedral interstices rather than regarding it as carbide. A perfect atomic arrangement of this type would correspond to the formula Fe_3AlC.(refer to Fig 3) In fact, this particular stoichiometry has never been observed. Recently, the formula $Fe_{4-y}Al_yC_x$ was suggested for the κ phase by Palm *et.al* , where x may vary between 0.8 to 1.2 and y between 0.42 and 0.71 [16]. While, Baligidad *et.al* [18] suggested the formula of the carbide as $Fe_3AlC_{0.5}$. The phase diagram and, in particular, the existence domain of this phase are not well known. It is difficult to determine the exact composition of κ phase. The solubility of carbon in iron aluminide melts decreases with increasing temperature leading to the precipitation of primary graphite. At the ideal composition of the κ-phase Fe_3AlC, the precipitation of graphite starts already at 2150°C, while the κ-phase might form at 1400°C. Even by rapid quenching, it is not possible to avoid graphite precipitation. Therefore, single-phase material of the κ phase can not be obtained directly from the melt. The homogeneity range of κ phase is markedly shifted to higher carbon concentration with decreasing temperature. Upon quenching the alloy may thus hit and penetrate into two-phase field α+κ. Therefore, at compositions where single-

phase material of the κ phase would be expected, in fact three phases may be observed, the κ phase plus primary graphite and ferrite [16 ,17].

The α solid solution

There is a noticeable solubility for carbon in the BCC (α) solid solution of up to 1 5 at wt % carbon. With increasing Al content the transition temperature of A2/B2 transformation increases with respect to the carbon-free crystals from about 40°C at 25 at % Al, to up to 100°C at 35 at % Al. This means that by the introduction of carbon the ordered B2 structure is stabilized with respect to the disordered A2 structure. This has been suggested to be because the B2 structure offers favorable surroundings of six iron atoms for carbon [16,17].

The γ solid solution

The extension of the stability range of the γ phase varies considerably as a function of temperature. With increasing temperature, the aluminium content increases from 7.5 at % at 800°C to 24 at % at 1315°C while the solubility for carbon is about constant. During cooling to room temperature, the γ phase undergoes a martensitic transformation. The temperature for this transformation is yet to be determined. The hardness of the martensite is considerably higher than that of the κ-phase [16].

Little is known about the Al-C system. The solubility of C in both liquid and solid Al is very limited (0.32 wt.% at 1227°C, decreasing to 0.10 wt.% at 830°C and extrapolating to 0.07 wt.% at 660°C. The only known compound of the system is Al_4C_3 [17].

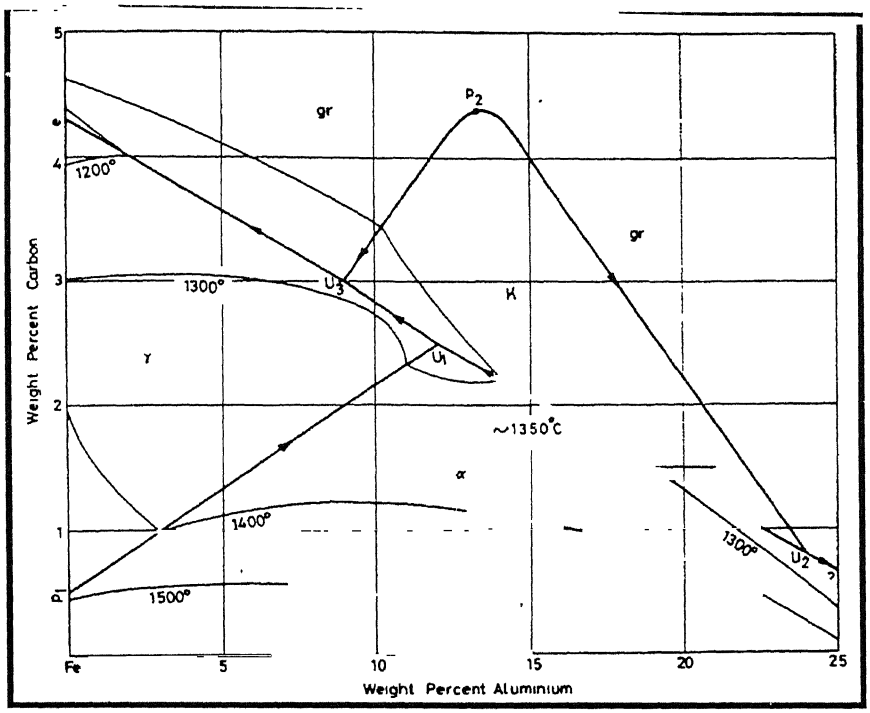

Figure 4 Al-C-Fe liquidus in weight percent

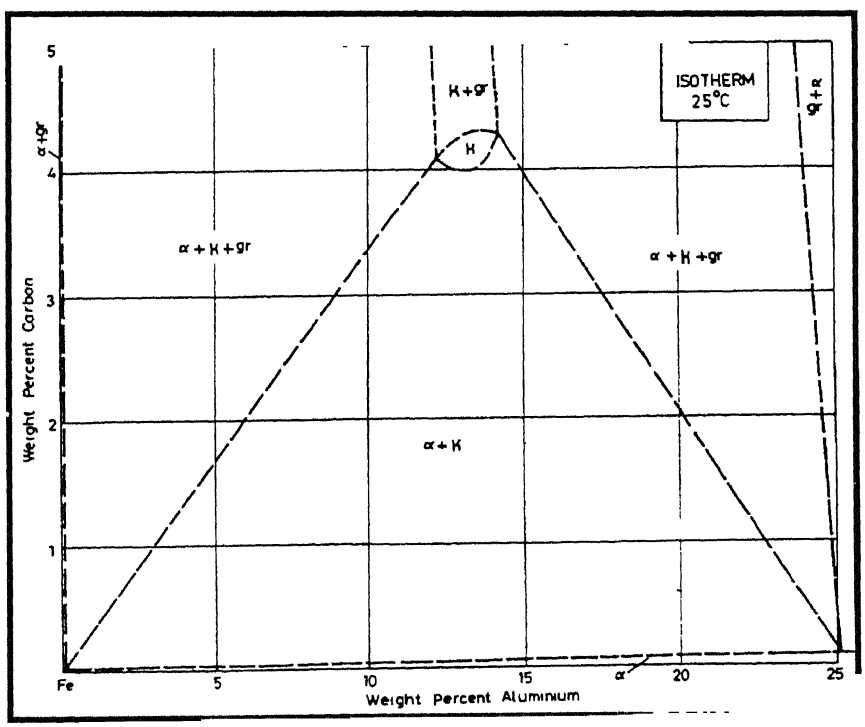

Figure 5 Fe-Al-C isotherms at 25°C in weight percent

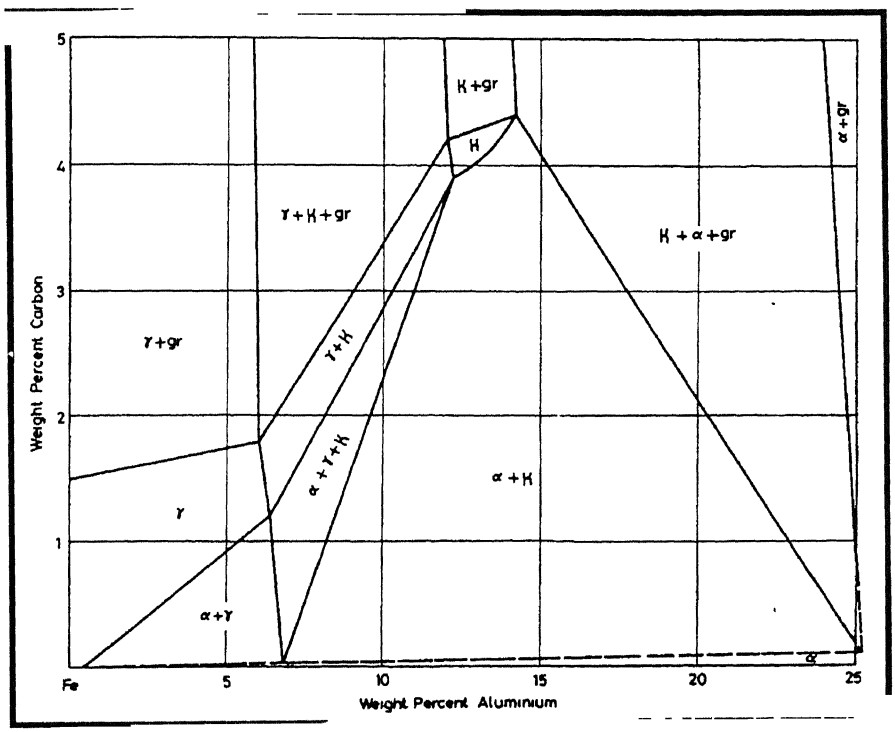

Figure 6 Fe-Al-C isotherms at 1000°C in weight percent.

2.2. Hydrogen embrittlement mechanism

Iron aluminides have been known to be brittle at room since the first study was conducted in 1930 [6,20]. However, the major cause of their low ductility and brittle fracture was not known for a long time. Liu *et al* have proposed an environmental effect as the major cause for room temperature embrittlement in iron aluminides [21]. They proposed that the embrittlement involves the reaction of water vapour with aluminium and the reaction product, atomic hydrogen enters the lattice and causes embrittlement.

$$2Al + 3H_2O \rightarrow Al_2O_3 + 6H \qquad \text{Eqn.1}$$

Direct evidence has also been provided recently for the production of hydrogen by reaction of iron aluminide with water vapour by Zhu *et al* [22] by a laser mass spectroscopic technique. The propensity of this reaction increases with increasing aluminium concentration in iron aluminides [21]. The reaction of condensed moisture from ambient environments with aluminium at crack tips and freshly created metal surfaces (due to oxide spallation) results in the generation of high fugacity atomic hydrogen that causes embrittlement. Fracture is observed to be essentially of cleavage type suggesting that "decohesion" as the possible mechanism of hydrogen embrittlement. In this mechanism, the hydrogen enters the material and is transported to potential flaw sites by bulk or grain boundary diffusion or by dislocations sweeping in of hydrogen. This hydrogen is supposed to lower the bond strength in iron aluminides leading to cracking by decohesion.

That hydrogen is the main damaging agent causing poor ductility was confirmed from tensile tests conducted in different environments. These results are summarized in Table 4 and 5. The effect of various test environments on the room temperature stress-strain behavior of iron aluminide is shown schematically in Figure 7. As evident from the figure, ductility is higher in Ar+4%H_2 environment rather than humid air. This is because molecular hydrogen does not cause embrittlement in Fe_3Al, because of its lower activity as compared with atomic hydrogen produced from water vapour reaction. As seen in this figure, testing in water vapour environment show the least ductility and vacuum/oxygen environments provide high ductility. Liu *et al* have shown that higher ductilities are

observed in a dry oxygen environment rather than in vacuum because oxygen reacts with aluminium to form Al_2O_3 directly [21]

$$2Al + 3/2\ O_2 \rightarrow Al_2O_3 \qquad \text{Eqn 2.}$$

thereby suppressing the aluminium-moisture reaction which provides nascent hydrogen. Generation of atomic hydrogen (Eqn 1) is suppressed and thus higher ductility is observed in dry oxygen environment.

2.3 Minimising hydrogen embrittlement

The crucial factor in improving the room temperature mechanical properties of iron aluminides, i.e. the ductility, is to restrict the entry of hydrogen into the material and to possibly irreversibly trap diffusive hydrogen. In order to obtain the desired properties of metals, alloying with additional elements is generally attempted. The type alloying addition would depend upon the property that is being addressed. For providing strength, elements that lead to solid solution strengthening or to the precipitation of age hardenable phases are added. This could also be increased by adding elements that refine the grain size and hence provide grain strengthening. In case the corrosion resistance of the metal has to be enhanced, passivity-inducing elements should be added. It should be emphasized that the alloying element that is added should not lead to the deterioration in some property where it is not intended. For example, if an element primarily added to enhance passivity, leads to the precipitation of ternary brittle intermetallics, especially at the grain boundaries, the property of strength would be very severely affected. therefore, the possible deleterious effects of alloying should also be understood [12].

Table 4 Room temperature tensile properties of iron aluminides after heat treatment for 2 hr at 700°C (B2 structure) [21]

Environment	Y.S. (Mpa)	U.T.S. (Mpa)	Ductility (%)
Vacuum	387	851	12.8
Oxygen	392	867	12.0
Air	387	559	4.1
H_2O vapour	387	475	2.1

Table 5 Room temperature tensile properties of iron aluminides after heat treatment for 120 h at 500°C (DO_3 structure)

Environment	Y.S. (Mpa)	U.T.S. (Mpa)	Ductility (%)
Vacuum	316	813	12.4
Oxygen	298	888	11.7
Air	279	514	3.7
H_2O vapour	322	439	2.1

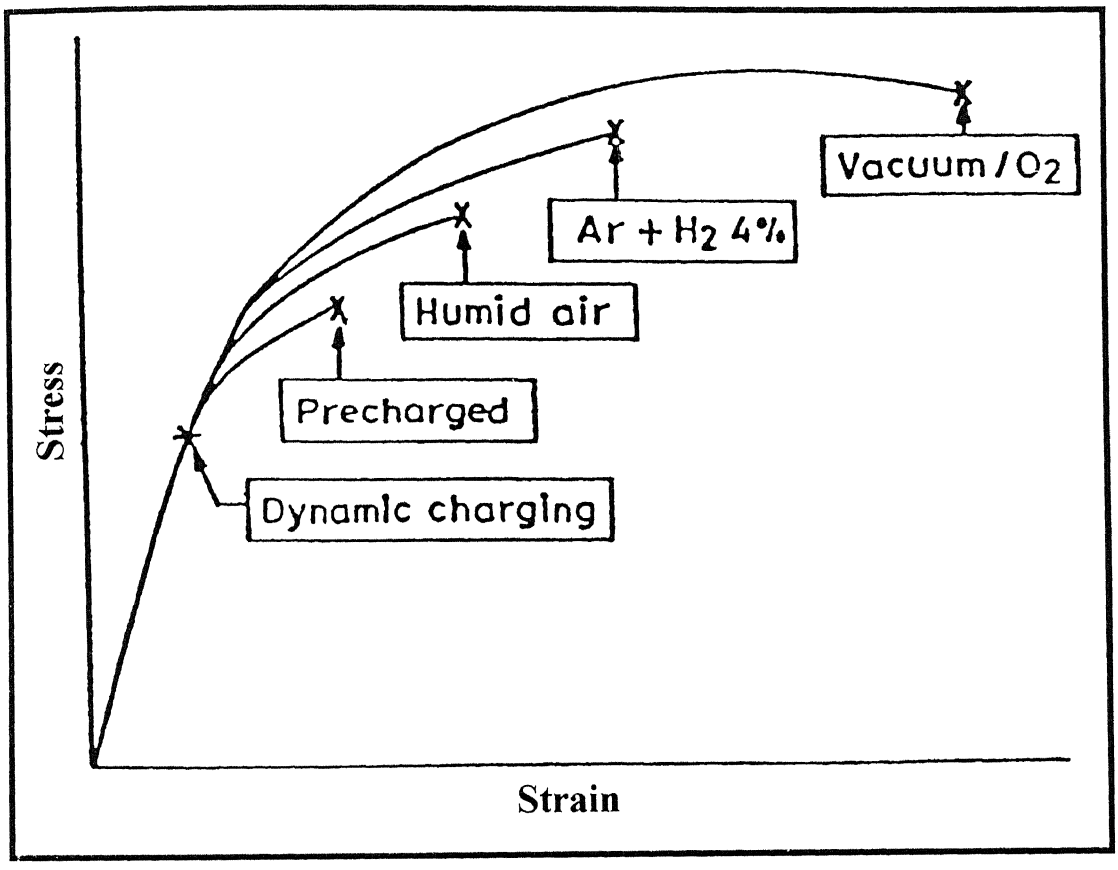

Figure 7. Schematic tensile stress-strain behavior of iron aluminides in various environments at ambient temperature

2.4 Effect of alloying elements

Alloying addition has been one of the schemes to improve the ductility of iron aluminides. Alloying control surface condition, reduction in hydrogen solubility and diffusion, refinement of grain structure,enhancement of grain boundary cohesion, grain shape and recrystallisation condition [7].

Several passivity inducing elements (Ti, Zr, V, Nb, Ta, Cr, Mo, W, Si, and Ni) have been alloyed to the base Fe_3Al intermetallic (to produce Fe_3Al-5M intermetallics) in order to test the ductility enhancement philosophy [23]. Ni could not be alloyed due to a violent reaction with the intermetallic on mixing, which is possibly due to the large exothermic heat of mixing between Ni and Al [24]. Electrochemical polarization studies of the alloyed intermetallics in acidic 0.05mol/l H_2SO_4 solution indicated that all the intermetallics except the V-alloyed one, induced passivity to the base iron aluminide, which exhibited active corrosion in this medium. Therefore, passivity enhancement by the addition of these elements has been verified. In view of the beneficial effect of the surface passive films in lowering the HE on iron aluminides [25], an alloy development philosophy was proposed wherein it was stated that elements that induce passivity in iron when added to Fe_3Al would inhibit hydrogen reduction and its entry by maintaining a passive layer [12,26].

2.4.1 Effect of Chromium

Among the metals alloyed with iron aluminide, the most effective alloying addition that results in ductility enhancements is Cr. Even Cr additions as low as 2% has been reported to be effective in providing ductilities [27]. The mechanism for the increase in ductility by Cr addition has been elucidated by the mixed potential theory by Balasubramaniam [12]. The potentiodynamic polarization curves of the base Fe_3Al and Cr-alloyed Fe_3Al have been theoretically deciphered and it was now clear that on alloying with Cr the mixed potential of the intermetallic is established in the passive region at a potential noble to the reversible hydrogen potential [28] suggesting that Cr induces passivity which results in reduction in the rate of hydrogen liberation rates on the surface of Cr alloyed iron aluminides. Moreover the passive layer would also hinder hydrogen entry into the lattice to cause embrittlement. This mechanism, hence, suggests

that the entry of hydrogen into the lattice can be checked and HE minimized by alloying passivity inducing elements into iron aluminides. McKamey and Liu have earlier suggested that the beneficial effect of Cr comes from surface oxide modification, rather than modification of bulk properties [9]. They suggested a change in oxide chemistry and properties or a change in kinetics of oxide formation, thereby reducing the water vapour reaction

2.4.2 Effect of Zirconium

Zirconium, has been alloyed to Fe_3Al to strengthen grain boundaries and to prevent recrystallisation [29]. McKamey and Pierce have confirmed that, a partially recrystallised microstructure reduces hydrogen embrittlement [29]. Therefore, zirconium additions can help in minimizing hydrogen embrittlement.

2.4.3 Effect of Titanium

Liu *et al* have studied the effect of Ti addition to Fe_3Al on the mechanical behaviour of at high temperatures [30]. They have demonstrated superplastic behaviour in the Fe_3Al-2Ti alloy at high temperature. Interestingly, this alloy showed superplastic behaviour even at a grain size of 100 microns. This has been ascribed to the process of dynamic recovery and recrystallisation occurring in Fe_3Al-2Ti intermetallic at high temperature.

The base Fe_3Al [31] and the abovesaid alloyed intermetallics [23] were thermomechanically processed at 1000°C by multipass rolling after a homogenization treatment (in order to make the composition of the buttons uniform). It was observed that only the Fe_3Al, Fe_3Al-5Cr and Fe_3Al-Ti intermetallics could be rolled successfully to 80% deformation in multipasses at 1000°C. The Cr and Ti alloyed intermetallic cracked after 50% deformation and the Fe_3Al-5Nb intermetallic cracked after 40% deformation. The Fe_3Al-5Mo, Fe_3Al-5Si and Fe_3Al-5V could not be rolled as they cracked in the first rolling pass itself. Thermomechanical processing of the intermetallic is also an important aspect of alloy development as the material should be amenable to deformation processing from a commercial angle. though the passivation inducing alloy additions induce passivity in the base intermetallic, the thermomechanical response of the

intermetallics alloyed with Ta, Nb, Mo, Si and V was poor due to the formation of brittle phases. A detailed fractographic and microstructural study of other intermetallics revealed the precipitation of brittle phases on the alloying Ta, Mo, V, Nb and Si to Fe_3Al [32]. It is therefore important that the addition of passivity inducing elements should not lead to brittle intermetallic precipitation. If this aspect can be taken care of by various compositional and structural modifications, then higher room temperature ductilities can be achieved with minimum hydrogen embrittlement. Moreover these alloying elements would also provide additional solid solution strengthening to these intermetallics.

2.4.4 Effect of Boron

Boron addition (in ppm range) has been found to be very effective in increasing the grain boundary cohesiveness in ordered intermetallic alloys [33]. Boron has also been effective for Fe-Al class of aluminides. Boron segregates at grain boundaries and reduces intrinsic brittleness of B2 iron alumindes [34].

2.4.5 Effect of Cerium

Yangshan *et al* [15] have shown that Ce addition in a very small amount increases significantly the ductility of base Fe-28Al and Cr alloyed iron aluminides. They proposed that Ce additions accelerated the formation of aluminium and chromium oxides which passivated the specimen surface, thus preventing hydrogen from diffusing into the specimen. Their observation was that small amounts of Ce additions caused primarily ductile failure instead of brittle failure as in the case of iron aluminides without Ce addition. Addition of Ce also produced a fine grain structure after complete recrystallisation in contrast to the large grain size observed without Ce additons. Therefore, strength was not significantly reduced upon complete recrystallisation in the Ce-alloyed iron aluminides. They also observed precipitates rich in Fe, Al and Ce to form in the grain boundary regions of Ce-alloyed intermetallics. It is reasonable to assume that the Ce containing phases acts as irreversible traps for hydrogen and therefore lowers the amount of hydrogen present in the material, thereby, delaying embrittlement. Therefore, the presence of strong hydrogen trapping compounds, homogeniously distributed throughout the iron aluminide matrix, could also be beneficial in delaying embrittlement.

Interestingly, the addition of Ce had also changed the composition of the surface passive film. With the addition of Ce, the surface layer contained a larger amount of Al_2O_3 and Cr_2O_3 and a lower amount of Fe_2O_3 than that of the Fe-28Al-2Cr alloy without Ce addition.

In view of this, studies were performed by Banerjee by addition of Mm (Indian mischmetal, a mixture of rare earth elements). Mm was added in small amounts to the Cr- and Ti alloyed iron aluminides [35,36]. The Mm added had the composition, in weight percent, 43Ce, 23La, 18Nd, 5Pr, 3Sm and 8Fe. The main aim of adding the Mm was to observe if enhanced room temperature ductilities would be obtained. However, the Mm added intermetallics were fairly brittle. Microstructural analysis indicated that several grain boundaries had cracked after the thermomechanical processing operation. The major elements that constituted Mm (namely Ce, La, and Nd) were enriched at the grain boundaries. Infact, La was analysed to be present only at grain boundaries. The poor ductilities obtained in the alloyed aluminides has been attributed to the presence of these elements (either in their elemental form or in the form of precipitates) along the grain boundaries which resulted in grain boundary weakening and to initiation of surface cracks during milling operation. Therefore, careful control of Mm (or Ce) addition may be required to render the iron aluminides ductile. [35].

The improvement of oxidation behaviour of Fe_3Al based alloys with Ce addition at 1000°C was reported by Yu *et al.* [37]. They observed that the oxidation resistance of Fe_3Al based alloy was significantly improved by Ce addition at temperatures above 1000°C. Compared with Ce-free alloys, the oxidation rate of Ce-containing alloy was much lower and no cracks or signs of spallation existed on the surface of oxide scale. The oxide scales on the alloy with Ce addition were smooth and flat in the whole duration of 120 hour oxidation at 1200°C. Ce addition results in significant refinement of oxide grains and reduction of iron or chromium oxides in alumina scale, both of which are beneficial to the improvement of strength for an alumina scale, and prevent the crack formation on the scale. The fine grains and almost pure alumina will also improve the compactness and continuity of oxide scales for alloy containing Ce, thereby effectively hindering further reaction between substrate and air after forming a continuous scale in the initial stage, This resulted in significant decrease of the oxidation rate.[37]. The

beneficial aspects of alloying Mm on the oxidation rate of iron aluminides has also been explored by Babu *et al* [38]. They observed that the addition of Ti and Mm changed the nature,colour and morphology of the scale leading to improved adherence.

2.5 Effect of carbon

Most of the reported literature is on iron aluminides containing very low (<0.01 wt %) carbon content, produced using very high purity raw material because carbon was believed to embrittle these alloys [7]. It was recently reported that addition of carbon to the Fe-16 wt % Al alloy results in improved strength, machinability, resistance to environmental embrittlement and creep resistance [40,41]. Carbon additions of 0.03 wt % or more result in precipitation of $Fe_{4-y}Al_yC_x$ phase (where x may vary between 0.8 to 1.2 and y between 0.42 and 0.71 [16]) in these alloys, which imparts significant dispersion strengthening and leads to improved creep resistance. Though $Fe_{4-y}Al_yC_x$ is a hard and brittle phase, its presence in the alloys matrix did not lead to reduction in ductility. This is because $Fe_{4-y}Al_yC_x$ precipitates were supposed to act as hydrogen traps, reducing the susceptibility of the alloy to hydrogen embrittlement [42]. This susceptibility to embrittlement in moist environments is a major cause for poor room temperature ductility and machinability. Addition of carbon has been reported for alloys with low (16 wt.%) Al-contents. In these alloys the addition of 1 wt.% carbon was found to lead to the best combination of mechanical properties [43]. The addition of carbon (in the range of 0.5 to 1.1 wt %) to the Fe-Al alloy (the range of Al content is 16 to 20 wt %) also allowed the use of low cost processing techniques such as air induction melting (AIM) followed by electro slag remelting (ESR) [40,42]. Cheap raw material such as steel scrap (which may contain significant amount of carbon) and commercial aluminium were used for melting of these alloys. The AIM and ESR ingots exhibited significant amount of precipitate $Fe_{4-y}Al_yC_x$ (where x may vary between 0.8 to 1.2 and y between 0.42 and 0.71 [16]). These precipitates form a continuous network resulting in a duplex Fe_3Al - $Fe_{4-y}Al_yC_x$ structure (Figure 8) [40]. Tensile testing was carried out for Fe-8.5Al-C alloys (where the range of carbon varied from .04 to 1.1 wt %) by Baligidad *et al* [45]. According to them, the

alloys showed cleavage mode fracture at room temperature. The fracture changed to mixed (cleavage + dimple) mode at 400°C and finally to dimple mode fracture at 600°C

The reduced susceptibility to cracking of high carbon alloys was attributed [42,43] to (i) likely decrease in hydrogen solubility with increasing carbon content of the alloy and (ii) hydrogen entrapment by the precipitates. The surface cracking has been attributed to hydrogen liberated by the reaction between aluminium in the alloy and water used as the coolant [42]. Addition of carbon leads to the formation of FeAlC phase, which may improve machinability by (i) reducing susceptibility to environmental embrittlement [42] and (ii) by allowing formation $Fe_{4-y}Al_yC_x$ of small even size chips during machining [43] in Fe-16Al (in wt %) alloys.

The addition of carbon resulted in a significant increase in yield strength [41]. This was attributed to the presence of a large volume fraction of hard. $Fe_{4-y}Al_yC_x$ precipitates and the formation of a Fe_3Al-$Fe_{4-y}Al_yC_x$ duplex structure. Similar results were obtained for Fe_3Al-based alloys with lower aluminium content [41]. The drop in strength observed above 600°C has also been reported for the low carbon alloys with similar Al contents [44]. The increase in ductility above 600°C may be related to the changes in failure mode from cleavage to the more ductile mixed mode failure and a likely change from DO_3 to B2 order in the material. Since the yield strength sharply fall for these intermetallics above 600°C irrespective of their carbon contents, it appears that the addition of carbon does not significantly affect the DO_3 to B2 structural transformation [40].

The addition of carbon to Fe-Al alloys resulted in significant strength improvements. At very low Al-contents (e.g. 8.5 wt % Al), the alloy was not susceptible to environmental embrittlement and the increase in strength is accompanied by a drop in ductility due to the presence of $Fe_{4-y}Al_yC_x$ precipitates. At higher Al contents (16-20 wt %), where the alloys are susceptible to environmental embrittlement, the benefits include improvement in machinability and strengthening without loss of ductility. However, the strength drops on increasing the Al-content from 16 to 20 wt %. Similar results have been reported for low carbon alloys where the loss in strength with increasing Al content has been attributed to weaker DO_3 order and increased dislocation mobility. On increasing the Al-content to still higher levels, the strength starts increasing after 23 to 24 wt % (38-

40 at %) Al when the alloys have a B2 structure. However, any carbon added to alloys containing more than 22 wt % (36.5 at %) Al, is likely to precipitate out as graphite, which is a very soft phase. It is, therefore, unlikely that the addition of carbon to B2 Fe-Al alloys will lead to significant strengthening. Cast Fe-Al alloys with low carbon contents exhibit poor ductility (1-3%) and optimum ductility is obtained only after extensive thermomechanical processing. In contrast high carbon electro slag remelted (ESR) alloys exhibit good (4-5%) ductility even in the cast condition. It is also observed that further increase in carbon content from 0.14 to 0.5wt% does not improve the creep and stress rupture properties [21,41].

The addition of Carbon enhances corrosion, due to the presence of cathodic carbides distributed in the matrix. A higher carbon content results in higher corrosion rate. These results are in conformity with the earlier studies [19,43].

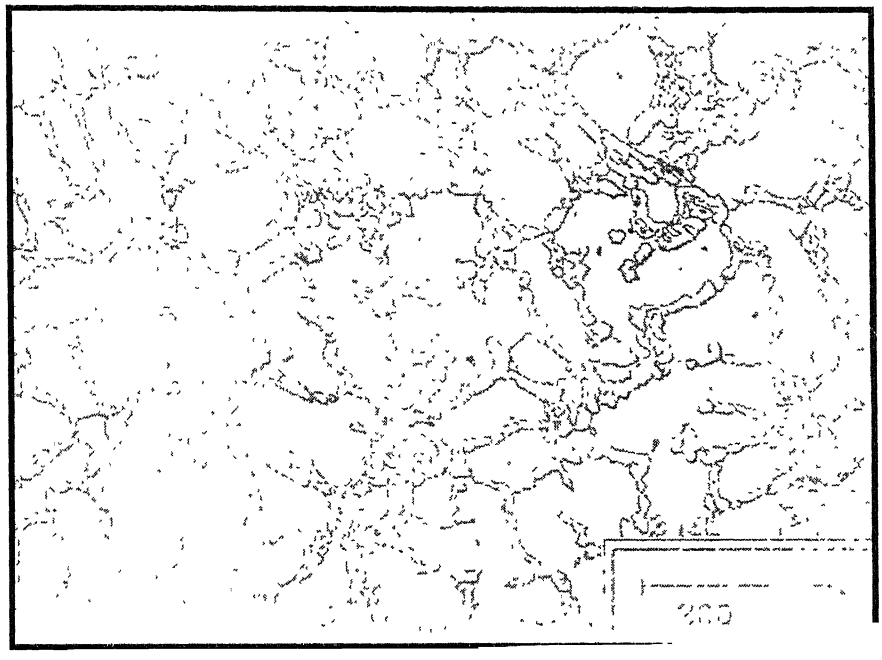

Figure 8 Optical micrograph of longitudinal sections of cast ESR ingots showing extensive precipitation of $Fe_3AlC_{0.5}$ [40]

2.6 Electrochemical corrosion

Corrosion can be defined as the degradation of a metal by an electrochemical reaction with its environment [46]. All metals are found in their low energy state ores, in the form of their oxides, sulfides, carbonates or more complex compounds. Large amount of energy is required in order to extract a pure metal from its ore. This pure metal is a high-energy state of the metal and hence they tend to come back to the low energy state by recombining with the environment. This process is called corrosion. Figure 9 shows the thermodynamic energy profile for metals and their compounds. The thermodynamic aspects of corrosion will be briefly discussed. All the interactions between elements and compounds are governed by the free energy changes (ΔG). Any reaction is said to be spontaneous when ΔG for the reaction is negative. At room temperature most of the chemical compounds of metals have lower free energy than the pure metals and hence most of the metals have an inherent tendency to corrode.

In all kinds of aqueous corrosion, there are two reactions occurring at the metal/liquid interface; an electron producing reaction (anodic or oxidation reaction) and an electron consuming reaction (cathodic or reduction reaction). The corrosion reaction for the creation of a wet electrochemical cell requires four basic requirements, the cathode on which the reduction reaction occurs, an anode on which oxidation occurs, an electrolyte to act as the conducting medium for ions and a electrical connection for electron to flow between the anode and cathode. The anodic reaction is invariably corrosion of the metal as shown in Eqn. 3. Several cathodic reactions can occur during corrosion [47]. The simplest of them is reduction of hydrogen ions as in Eqn.4. In the absence of any of these reactions water reduction will occur as in Eqn. 5. Another is reduction of an oxidized ion in solution (redox reaction) as in Eqn. 6. And yet another reaction is reduction of dissolved oxygen as in Equations 7 and 8.

$M \Rightarrow M^{n+} + ne^-$	(Anodic Reaction)	Eqn. 3
$2H^+ + 2e^- \Rightarrow H_2$	(Hydrogen Reduction Reaction) $pH \leq 7$	Eqn. 4
$2H_2O + 2e^- \Rightarrow H_2 + 2OH^-$	(Water Reduction Reaction) $pH > 7$	Eqn. 5
$Fe^{3+} + e^- \Rightarrow Fe^{2+}$	(Redox Reaction)	Eqn. 6
$O_2 + 4H^+ + 4e^- \Rightarrow 2H_2O$	(Oxygen Reduction Reaction) $pH \leq 7$	Eqn 7
$O_2 + 2H_2O + 4e^- \Rightarrow 4OH^-$	(Oxygen Reduction Reaction) $pH > 7$	Eqn. 8

A basic wet corrosion cell is shown in the Figure 10. The potential difference between the anode and the cathode could be measured by using a high impedence voltmeter in the circuit. This provides only the potential difference between the electrodes and in order to measure the absolute potential we need a third electrode. This third electrode is called as the standard electrode against which all the measurements can be made. Reference electrodes like standard hydrogen electrode (SHE), saturated calomel electrode (SCE), etc. are usually used as the standard electrodes. Table 6 lists some commonly used standard electrodes and their potentials.

2.7 Polarization

When a metal is not in equilibrium with the solution of ions, the electrode potential differs from the standard electrode potential by an amount known as the polarization [46]. It can also be said as over-potential or over-voltage. Polarization is a very important corrosion parameter as it is useful in calculating the rates of the corrosion process. The deviation of the equilibrium potential is a combination of an anodic polarization of metal and a cathodic polarization of the environment. If the electrons are made available the potentials at the surface becomes more negative, suggesting that excess electrons with their negative charges accumulate at the metal/solution interface waiting for the reaction. This negative potential charge is called as cathodic polarization. Similarly, if electrons are removed from the metal surface interface a positive potential change will occur called anodic polarization [47]. In an aqueous electrolyte solution, the

surface will reach a steady potential, E_{corr}, which depends on the ability and rate at which electrons can be exchanged by the anodic and cathodic reactions. When the surface potential increases above the E_{corr} value, to a value E, then the anodic polarization is given by the difference between E and E_{corr}. At equilibrium, the forward anodic reaction, i_a is equal to the reverse cathodic reaction, i_c. Hence the rate of the reaction can be given by,

$$i_a = i_c = i_o = A_o \exp[-\Delta G/RT] \qquad \text{Eqn. 9}$$

There are two methods available for measurement of corrosion rate using polarization methods, namely Tafel extrapolation and polarization resistance. The polarization methods to measure corrosion rates have their inherent advantages. The polarisation resistance *Rp* is derived from the slope of the linear polarisation curve and is used in calculating the corrosion rates of the alloys using equation

$$Rp = \beta a \beta c / 2.3\, i_{corr}(\beta a + \beta c) \qquad \text{Eqn 10}$$

where βa and βc are the tafel constants and $\imath corr$ is the corrosion current density.

The main advantage of these methods is that the time taken for conducting experiments is relatively short, whereas the conventional weight loss methods require several days. The polarization methods are highly sensitive, and accelerating factors such as elevated temperature, to increase rates, is generally not necessary. Moreover, these methods are non-destructive and several repetition experiments can be carried out using the same sample.

The mixed potential theory forms a basic for explaining the polarization techniques. The mixed potential theory consists of two simple hypotheses:

1. Any electrochemical reaction can be divided into two or more partial oxidation and reduction reactions.
2. There cannot be net accumulation of electrical charge during an chemical reaction i.e., corrosion reaction the sum of the anodic oxidation currents should be equal to the sum of the cathodic reduction currents. In other words the total rate of oxidation should be equal to total rate of reduction [48].

Consider the reactions for zinc getting corroded in an acid solution. Then the anodic and cathodic reactions are given by,

$$Zn \Rightarrow Zn^{2+} + 2e^{-} \quad \text{(Anodic reaction)} \qquad \text{Eqn. 11}$$

$$2H^{+} + 2e \Rightarrow H_2 \quad \text{(Cathodic reaction)} \qquad \text{Eqn. 12}$$

These reactions are called as the half-cell reactions and the potential corresponding to them are called cell potential. The potentials cannot coexist separately on an electrically conducting surface. The potentials will polarize to an intermediate value called as the corrosion potential or mixed potential (E_{corr}). When there is no external current flowing into the system, then the equilibrium potential attained is called free corrosion potential (E_{corr}).

As the reactions polarize on the same surface the change in potentials is given by,

$$\eta_a = \beta_a \log (i_a/i_o) \qquad \text{Eqn. 13}$$

$$\eta_c = \beta_c \log (i_c/i_o) \qquad \text{Eqn. 14}$$

where η_a and η_c are anodic and cathodic polarization, β_a and β_c are the Tafel constants, i_a and i_c are the anodic and cathodic currents respectively. At E_{corr}, the rates of anodic and cathodic reactions are equal and is equal to the current density, i_{corr}. The half-cell reactions for dissolution of Zn in acid are shown in the Figure 11. This figure is called as Evans diagram or polarization diagram and represents the corrosion of an active material.

The various polarization techniques that are commonly used are linear polarization, Tafel extrapolation, potentiodynamic polarization and cyclic polarization. These polarization techniques are summarized in the Figure 12.

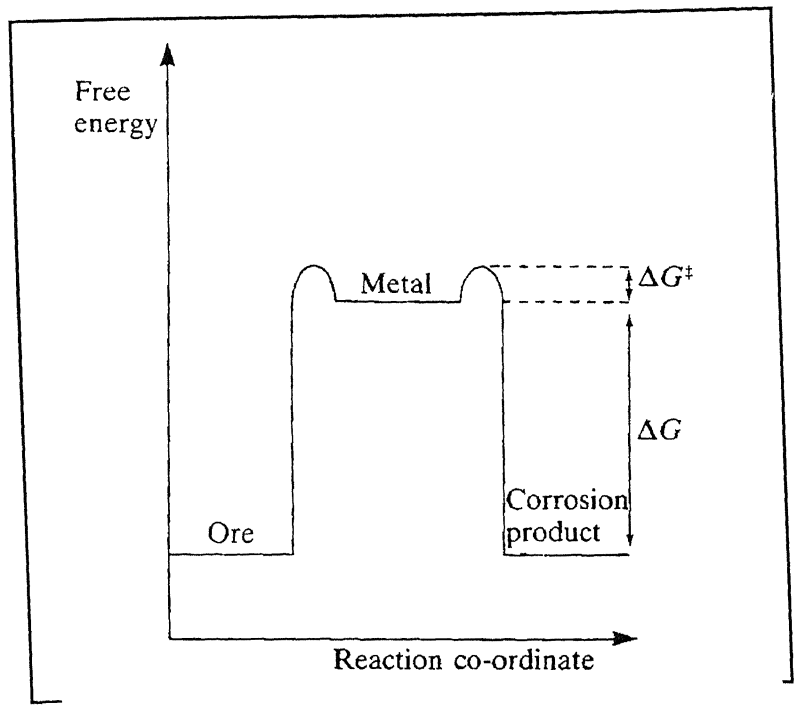

Figure 9 Thermodynamic energy profile for metals and their compounds [46]

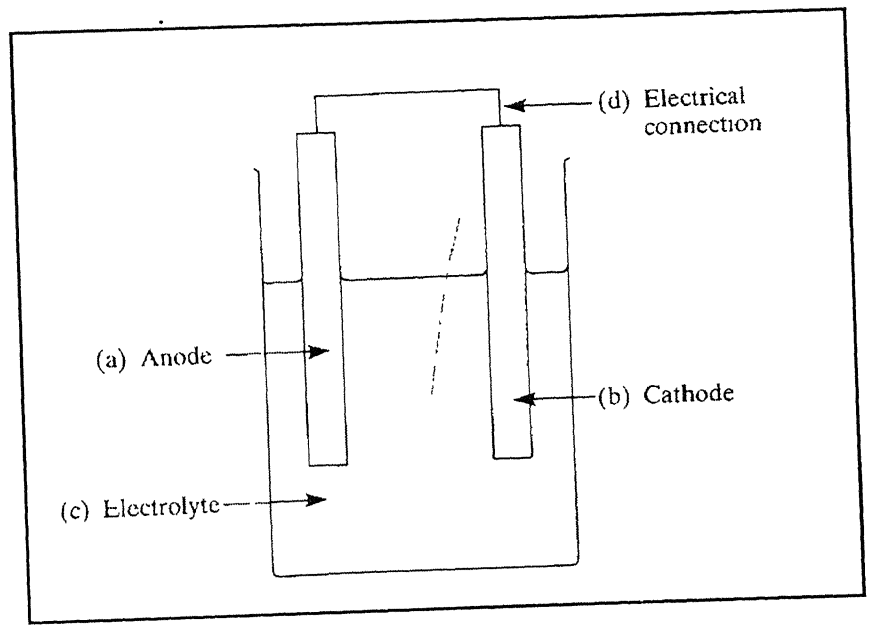

Figure 10 Basic wet corrosion cell [48].

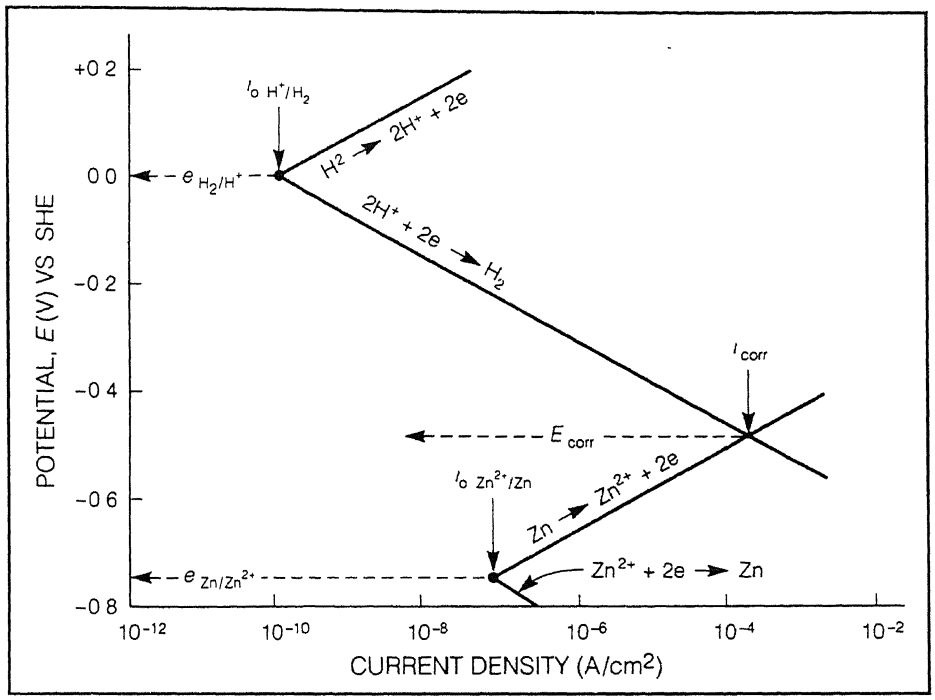

Figure 11 Evans diagram for an active metal (Zn) [48].

Table 6 Standard reference electrode potentials [48].

Electrode	Electrolyte	Potential (V)
Calomel (SCE)	Saturated KCl	+0.2420
Calomel (NCE)	1.0 M KCl	+0.2810
Calomel	0.1 M KCl	+0.3335
Silver/Silver Chloride (SSC)	1.0M KCl	+0.2224
SSC	Sea water	+0.25 (approx)
Copper/Copper sulfate (CSE)	Sea water	+0.30 (approx)
Zinc	Sea water	-0.79

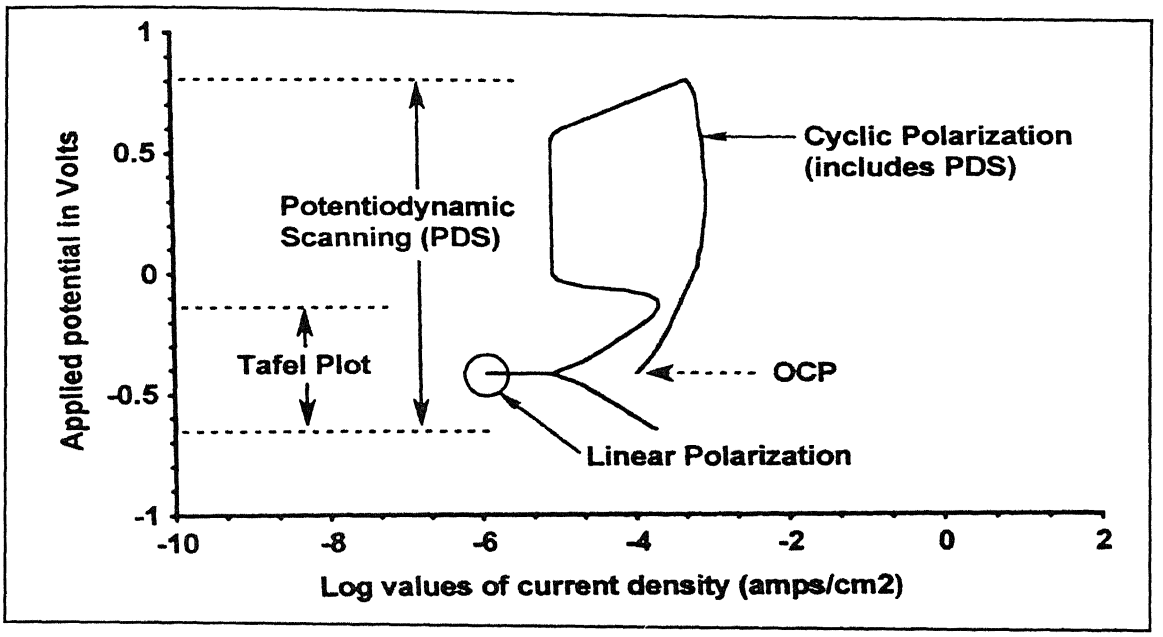

Figure 12. Various types of polarization methods [47].

2.7.1 Potentiodynamic Polarization

The potentiodynamic polarization is carried out in a wider range of potential spectrum and gives much more details about the samples response to the environment. The potentiodynamic polarization provides data about the metal behavior i.e., whether the metal is active or passive or active passive in the given environment. The plot elucidates the properties of the passive film and the effect of inhibitors on the corrosion behavior of the metal. Depending upon the nature of potentiodynamic polarization curve, alloys can be divided into active alloys and active-passive alloys. For an active metal the corrosion rate increases linearly with increase in the anodic polarization potential. This is due to the non-protective oxide layer, which forms on the metal surface. For an active passive metal the corrosion rate increases with polarization potential up to a critical current density, (i_{crit}) after which it falls down rapidly due to the formation of a protective passive film.

Figure 13 shows a typical potentiostatic/dynamic anodic polarization curve of a metal exhibiting passivity. The important points in this curve are described below.

A- Corresponds to the equilibrium potential of the metal under a given environment condition.

AB- Anodic polarization behavior of a normal corroding metal.

B- Corresponds to equilibrium potential for initiation of passive growth E_{ip}.

C- At potential of primary passivation E_{pp} acceleration of metal dissolution occurs. At potential E_{pp}, the rate of protective film growth already exceeds the rate of its chemical dissolution and the process of protective film formation begins.

D- At potential E_{cp} where formation of continuous protective film is completed and complete passivation is obtained.

DE- Metal dissolution occurs at a constant rate through the passivating oxide film.

E End of passivity range.

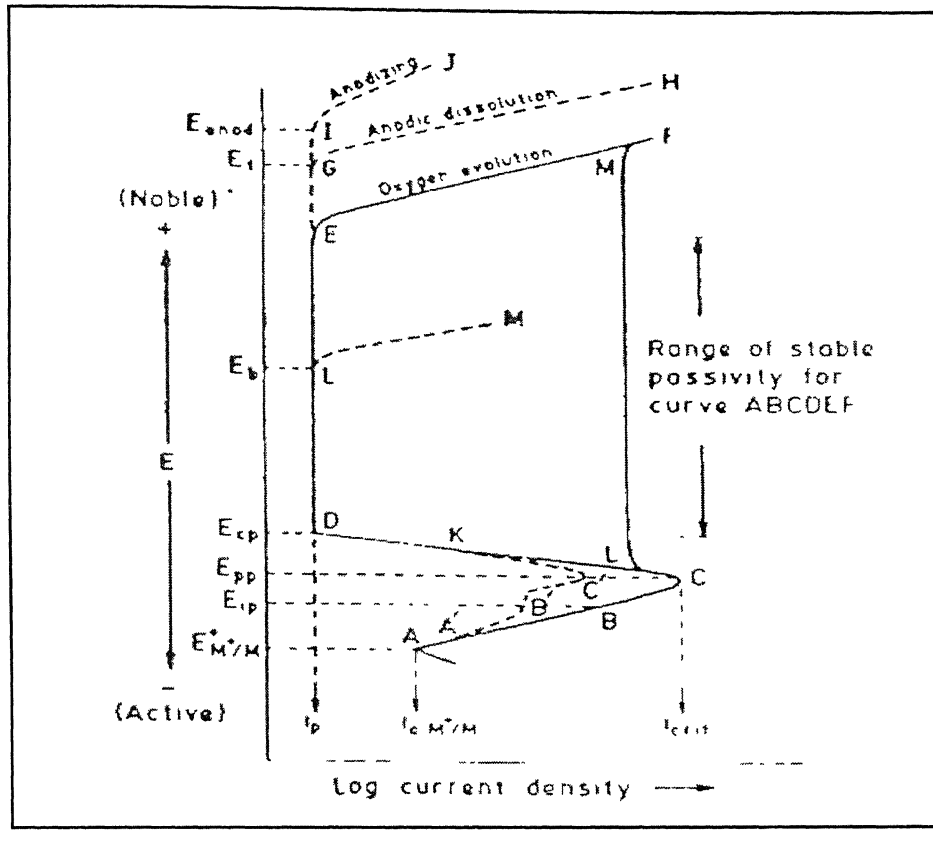

Figure 13 Anodic polarization curve for metal exhibiting passivity.

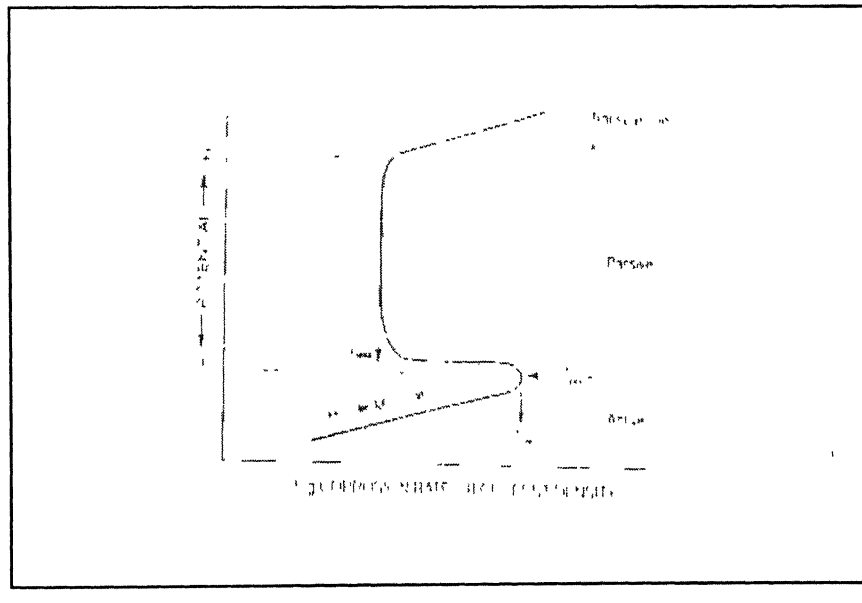

Figure 14 Schematic curve showing active passive polarisation behaviour [47]

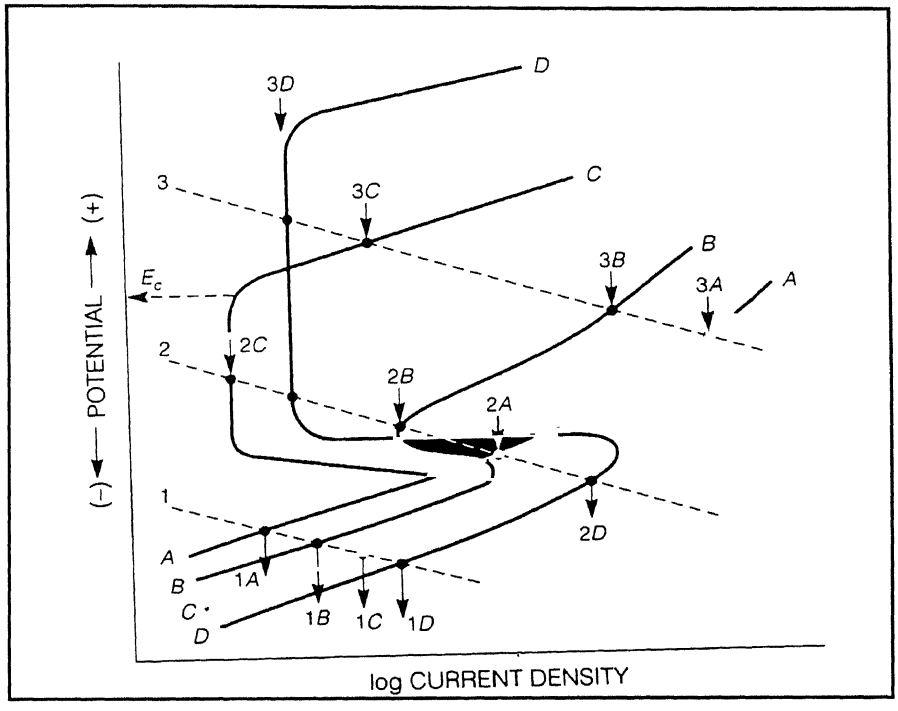

Figure 15 Schematic anodic polarization curves for hypothetical alloy A,B,C and D in 1) reducing 2) moderately oxidizing 3) highly oxidizing environments [47]

The anodic region in the Figure 14 can be subdivided into three main regions namely, the active region, the passive region and the trans-passive region. The active region and the cathodic curve can be extrapolated to extract the values of E_{corr} and i_{corr}. The active region ends at the primary passivation potential (E_{pp}) at which the passive film becomes stable and the corrosion rate falls rapidly. The current corresponding to this value is called as critical current density (i_{crit}). As the potential is increased beyond this value, the current density decreases until it reaches a steady current called as the passive current density (i_{pass}). The range over which the steady current is maintained is known as the passive range and it relates to the stability of the passive film. As the potential is increased further the passive layer breaks down and the anodic rate increases in the transpassive region. This breakdown in passivity can be attributed to the oxygen evolution or due to localized mechanisms such as pitting. In certain kind of alloys like stainless steel, there will be an additional region showing secondary passivity. This results due to the formation of some secondary oxide layer, which ultimately breaks leading to increase in the corrosion rate. The potential at which the passive film breaks is known as pitting potential (E_{pitt}) and the potential at which the surface oxide film is destabilised is often called the breakdown potential (E_b).

2.7.2 Criterion for selection of active passive metals

Potentiostatic/potentiodynamic anodic polarization is widely used method to compare the corrosion resistance of different metals and alloys in a specific environment [47]. A schematic representation of various comparing parameters is given in Figure 14 and a schematic comparison of the hypothetical alloys is given in Figure 15. For reducing conditions, as in number 1, either the non-passivating alloy A or the partially passivating alloy B is superior to the other two because A and B have lower corrosion rates (or current densities, ($i_{corr,\ 1A}$ and $i_{corr,1B}$) in the active condition without oxidizers. The alloying elements, for example chromium, needed to produce strong passivity passivity make C and D far more expensive and thus unjustified for service in condition 1.

For moderately oxidizing conditions, number 2, the recommend alloy would be C because the reduction curve exceeds the critical current density for passivation and it is

the only alloy in the stable passive condition. Although the reduction curve also exceeds the critical passivation current density for alloy B, the passivation current at 2B is not enough and the passive region is not broad enough to ensure good resistance in the passive state. Alloy D is in a state of borderline passivity with both active, 2D, and passive state possible. The active state is generally chosen as the most likely in cases of borderline passivity. The corrosion rate of the non-passive alloy, A, is predictably high at 2A in oxidizing conditions of any degree.

The recommended alloy in highly oxidizing condition (number 3) is D, since now the reduction curve exceeds the critical current density for passivation , and the corrosion rate is low at 3D. passivity breaks down for alloy C at E_C , and corrosion rate is increased at 3C, which is above the passive current density at 2C. alloys A and B are not resistance to highly oxidizing conditions.

The breakdown of the alloy C, at E_C, may occur due to initiation of localized corrosion in pits or crevices. With no breakdown either of the alloys C or D may be chosen because corrosion rates 2C and 3D in the passive state are both very low.

It can therefore be predicted about the choice of the alloy according to the parameters derived from paotentiostatic anodic polarization.

1. i_{corr} should be as low as possible.
2. I_{crit} should be as low as possible.
3. E_{cp} should be as low as possible.
4. E_{pp} should be as low as possible.
5. E_{pit} should be as high as possible.
6. Range of passivity should be as high as possible.

CHAPTER 3

EXPERIMENTAL PROCEDURE

The aim of the present work is to understand the effect of Ce addition on the electrochemical behaviour of carbon-alloyed iron aluminide. Non Ce-alloyed samples ESR74 and ESR127 were prepared to 600 grit in the rolling direction. For the Ce-alloyed sample ESR137, the sample was prepared to 600 grit in all the three directions viz, long transverse, short transverse and the rolling direction. These samples were subjected to potentiodynamic polarization studies. Long term and short term immersion testing experiments were also carried out and the results were then used for comparison. Stereological methods were applied to analyze the microstructural aspects. The hardness of the individual phases was characterized by microhardness testing.

3.1. Raw materials

The carbon-alloyed iron aluminides were obtained from Defence Metallurgical Research Laboratory (DMRL), Hyderabad, Their composition (in at %) were Fe-18.5Al-3.6C (ESR127) and Fe-20.0Al-2.0C (ESR74) and Fe-19.2Al-3.3C-0.07Ce (ESR137). In terms of wt %, the compositions were Fe-10.5Al-0.9C (ESR127) and Fe-11.0Al-0.5C (ESR74) and Fe-10.5Al-0.8C-0.2Ce (ESR137). Here, ESR stands for electro slag remelted specimens and these marked materials were obtained from DMRL, Hyderabad, in the form of rolled strips.

The alloys were originally processed via ingot metallurgy route. The processing technique utilized to obtain these strips is described as follows [50]. Commercial purity aluminium and mild steel scrap were used as raw materials for preparing the base iron aluminide ingots. Grinding was done to clean the surface of the iron charge. After melting the raw materials through the air induction melting process (AIM), the slag product was skimmed off. Aluminium pieces were then added to the molten iron bath. The melt was held at 1620°C for a very short time (2 minutes) to prevent aluminium losses and then normalized to room temperature and was then cast into cast iron moulds.

The ingots were then tested for their soundness by radiography. These AIM ingots (55 mm diameter, 360 mm long) were machined to 50 mm diameter. They were then refined by electro slag remelting (ESR) process in an ESR furnace of 350 kVA capacity. A commercial prefused flux based on CaF_2 was used. The flux was preheated and held at 850°C for 2 hours before use in order to remove moisture. The iron aluminide electrode was remelted under this flux cover and cast into 76 mm ingot in a water cooled steel mould. At the end of the process, the power supply was gradually reduced to impose a condition of hot topping. To check their soundness, the ESR ingots were also radiographed. The ingots were then forged to a reduction ratio of 70% and after forging they exhibited recrystallized grains [50].

Iron aluminide of composition Fe-19.2Al-3.3C-0.07Ce was prepared under an inert (argon) atmosphere using the base iron aluminide ingots with Ce (of purity 99.99%) as the alloying element.

This alloy button and the base Fe_3Al were homogenized at 1000°C for 4 hours before processing to further minimize segregation. The alloy buttons and the base iron aluminide thin strips were rolled in multi passes to 80% deformation at 1000°C (in disordered α phase field). Prior to rolling, the materials were soaked in a furnace for 1 hour. All the strips had a brown layer of oxide after rolling.

3.2. Material characterization

3.2.1. Optical microscopy

Standard metallographic techniques were used for preparation of the samples: sectioning, mounting, grinding and polishing. Rectangular specimens were cut from the as received alloy samples by using a abrasive cutter (Buehler, Germany).

The specimen size could not be maintained to a standard uniform size due to the limited amount of available specimen. The specimen length varied from 11.00 mm to 13.5 mm while their breadth varied from 9.00 mm to 11.00 mm and the thickness of the specimen varied from 6.50 mm to 7.0 mm. All the surface of the specimens, were mechanically polished in fine cloth using 0.5μ alumina powder and then degreased using

acetone before being used for each electrochemical experiment. In order to understand the microstructure the specimens were hot mounted. Care was taken while mounting to maintain the flatness of the sample and the mount. Grinding of the sample was performed in a series of emery papers staring from coarse grit to fine grit. The sample was ground carefully to avoid higher relief of the softer matrix than the hard carbides. Polishing was performed by using 0.5 μm alumina powder. For revealing the microstructures, an etchant of composition (volumetric) 33% acetic acid (CH_3COOH), 33% nitric acid (HNO_3), 33%water (H_2O) and 1% hydrofluoric acid (HF) was used. Optimum etching time was determined as 5 seconds after several trials.

The microstructures were recorded using an optical microscope (Axiolab A, Zeiss, Germany), attached with a digital camera (CE, Japan). They were later analyzed by the image-analysis program (Image-Pro Plus, version 4.1, Media Cybernetics, USA).

3.2.2. Scanning electron microscopy

Scanning electron micrographs were obtained for all the samples in a scanning electron microscope (SEM) (JEOL JSM 840A). The samples were finely polished up to 0.5-micrometer finish using Al_2O_3 powder and then were etched, prior to the SEM observations. The samples were over etched slightly in order to obtain better contrast for SEM observations.

3.2.3 Microhardness measurements

Microhardness measurements of both the phases, i.e. carbide and matrix, of all the samples were performed using a miniload microhardness tester (Lietz, Germany) attached with an optical microscope. A diamond pyramid indentor with a 50-gram load was employed. Observations were made at a magnification of 500X. Ten fields of view were chosen for each sample. All the values were noted as Vickers hardness number (VHN) which was obtained from the formula written below;

$$VHN = 1854.4 * P/d^2 \ (Kg\ mm^{-2}), \qquad \text{Eqn. 15}$$

where 'P' is the load in grams and 'd' is the average of the two diagonals of indentation mark in micrometer.

3.2.4 X ray diffraction

X ray diffraction (XRD) patterns of the Fe_3Al of Fe_3Al-Ce intermetallics were recorded with a Rich-Siefert 2002 X-ray diffractometer using CuKα radiation. The scan rate was fixed at 3°/min and the chart speed was fixed at 3cm/sec. The patterns were obtained between 30° to 100°. A magnification of 5K was used in all the recordings.

3.3 Stereological analysis

3.3.1 Measurement of the stereological parameters

Stereological analysis was done for the samples under study (ESR74, ESR127 and ESR137). The microstructures obtained in the rolling plane was taken up for observation and stereological studies because the available area for analysis was larger for the rolling plane. Moreover the electrochemical behaviour was evaluated in greater detail for this section. Each sample was observed at 30 different positions (fields of view) and the results were tabulated and analysed (refer Appendix A). The 95% confidence interval, which is a measure of the sampling error, is provided besides the individual measurements.

Volume fraction

Volume fraction represents the fraction of carbides as seen in the two dimensional microstructure [39]. In order to calculate the V_V of the carbides, a 10X10 grid was used and the sample was observed at 500X. The total number of intersection points between the crossed grid of the test lines and the carbides in each field of view was calculated manually and divided by the total number of points. The result provided the volume fraction. The results were tabulated in Appendix A

Grain size

The size of the grains are calculated by imposing 8 random test lines each of length 2300 microns on the image taken at a magnification of 50X. The total number of intersection points between the test lines and the grain boundaries is counted and the measured grain size is given by Gz =(n L / P) where Gz represents the grain size, n is the total number of grid lines, L is the length of a grid line and P is the number of intersection points between the test lines and the grain boundaries.

Surface area of exploded features per unit volume

Surface area of exploded carbides per unit volume provides an understanding of the space occupied by the carbides in the matrix [26]. For the purpose of calculating the surface area of the exploded carbides per unit volume and the contiguity parameters, 10 test lines, each of length 206 microns was drawn on the optical micrograph and the readings were taken. The final calculation is done using the equation

$$(S_V)_C = (2P / L) \qquad \text{Eqn. 16}$$

where $(S_V)_C$ is the surface area of the exploded carbides per unit volume, P is the number of intersection points between the test lines and the partition line of carbides, and L is the total length of the test lines. During the calculation of $(S_V)_G$, 2 is multiplied with P because when a test line intersects the boundary of two grains the number of intersection points were counted as one.

Contiguity of different phases

Contiguity is a measure of the fractional surface area of each feature occupied by other features of the same type [26]. Contiguity of carbides is calculated using the equation.

$$C_G = 4P_{L\alpha\alpha}/(4P_{L\alpha\alpha}+2P_{L\alpha\beta}) \qquad \text{Eqn. 17}$$

where C_G is the contiguity of carbides

$P_{L\alpha\alpha}$ is the number of intersection points between the test lines and the partition line of two adjoining carbides divided by the unit length of the test line and

$P_{L\alpha\beta}$ is the number of point intersections between the test lines and the partition line of grains and the carbides divided by the unit length of the test line.

3.4 Electrochemical studies

3.4.1 Apparatus for polarisation studies

The main apparatus used for the polarization experiments were a polarization cell and a potentiostat (Perkin Elmer potentiostat Model 263A) interfaced to a personal computer. The potentiostat used in the study was capable of performing a wide variety of potentio and galvano functions required for basic and applied studies in the field of corrosion. Electrochemical polarization studies were conducted using a Perkin Elmer potentiostat (Model 263A). Its ±20 V compliance and ±200 mA (±2 A with 94 Option) output capabilities allowed rapid and accurate potential or current control in the electrochemical cell. The schematic of a potentiostat connected with the polarization cell is shown in Figure 18. The potentiostat consists of an ammeter, an electrometer and a power supply. Three probes from the potentiostat were connected to the working electrode, reference electrode and counter electrode. The fourth probe was grounded. The polarization cell used for the polarization studies was a flat cell and a round bottom cell. The schematic representation of the flat cell are shown in Figure 17 .The flat cell was initially used in the present study. An Ag/AgCl electrode in saturated KCl was used as the reference electrode and the counter electrode was a platinum grid. The potential of the reference electrode was +197mV with respect to standard hydrogen electrode (SHE). The working electrode was placed in the flange and tightened so as to expose only $1 cm^2$ of the sample area to the electrolyte. The samples did not require any type of polymer mounting for this type of cell, as there was provision for attaching the sample without mounting. However, both the surfaces of the sample should be flat in order to prevent leakage of electrolyte.

The potentiodynamic experiments performed using a flat cell at a scan rate of 0.166mV/sec were not successful and the results non repetitive. Besides the polarisation curves were not smooth and was found having disturbances. The cause was identified and was found due to the evolution of hydrogen gases from the specimen, which sometimes

blocked the capillary tube emanating from the reference electrode, and which was closely placed to the working electrode. Hence the polarisation experiments for all the samples were conducted in a round-bottom cell at a scan rate of 1mV/sec.

Figures 19 and 20 provide a comparison of polarization curves obtained from the flat cell and the round bottom cell for the sample ESR137. The experimental results and the polarisation curves obtained from the polarisation experiments conducted in the flat cell have been tabulated in Appendix B.

The schematic representations of the round bottom cell are shown in Figure 16. A round bottom cell is a flask with a round bottom and has provisions in the form of various necks on the top to permit the introduction of electrodes, gas inlet and outlet tubes, and a thermometer. The samples used as working electrode in the round bottom cell were cold mounted. Cold mounting was done using a resin powder and an organic solvent. An electrical wire was soldered before the mounting to the sample in order to provide electrical contact with the anodic point of the cell in this case. The sample with the attached wire was cold mounted to expose only the concerned surface. The exposed area was measured by slide calipers before attaching with the cell. The Luggin probe connected with KCl salt bridge seperated the bulk solution from the saturated calomel reference electrode (SCE). The probe tip could be easily adjusted to bring in close proximity with the working electrode. The three electrodes used are the working electrode (mounted specimen connected with a wire), the counter electrode (high purity platinum stock flat wire) and the reference electrode. (a saturated calomel electrode with E^{O} = + 0.242 V vs. standard hydrogen electrode), as per the ASTM recommendations [49]. The potential of the calomel electrode was checked at periodic intervals to ensure the accuracy of the potential of the electrode.

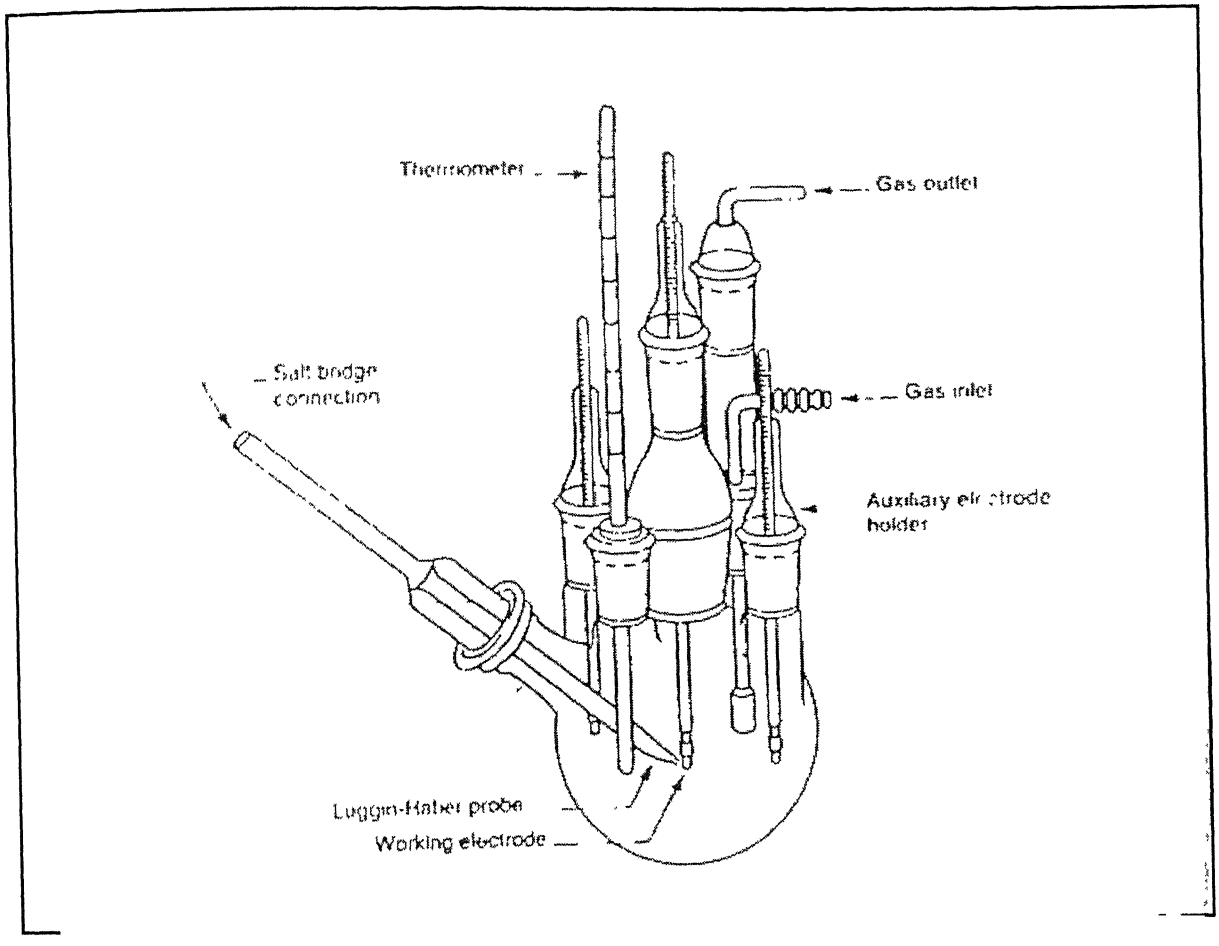

Figure 16. Electrochemical polarisation round bottom cell used for conducting polarisation studies

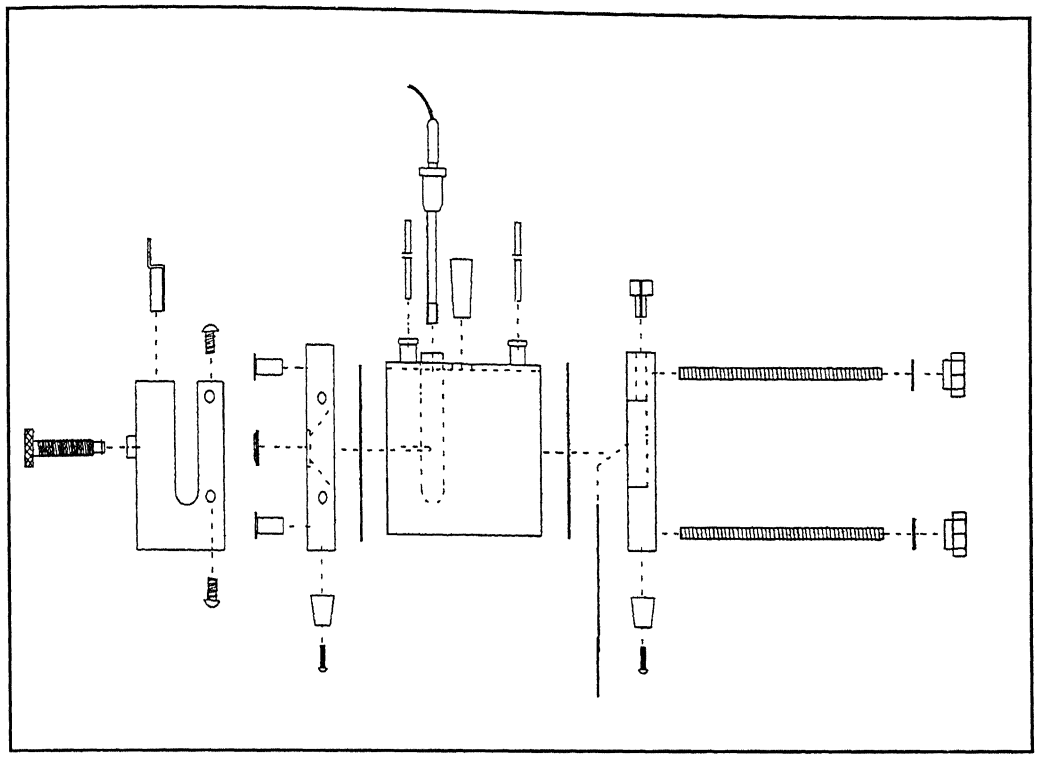

Figure 17 Schematic representation of Flat Cell

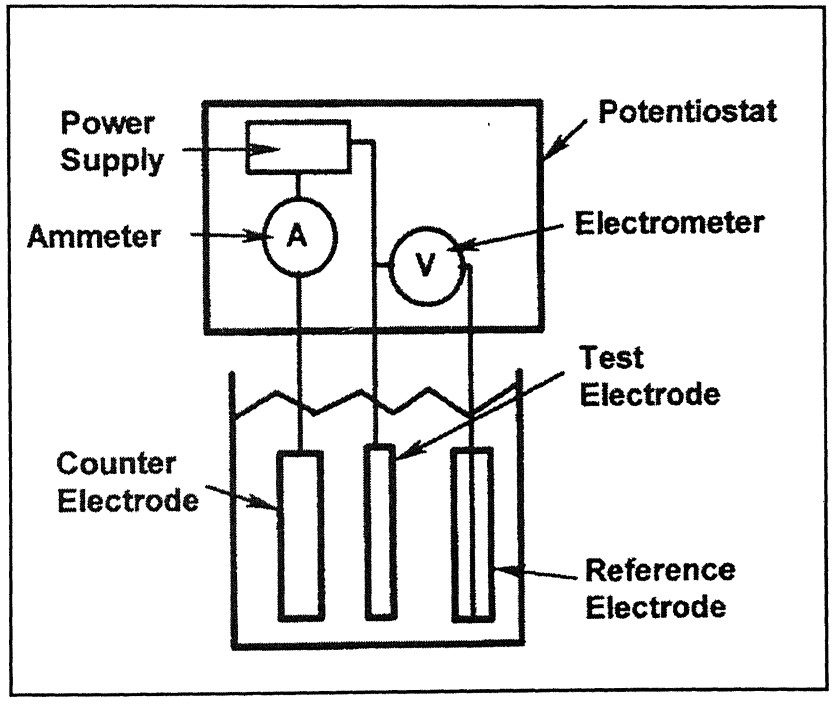

Figure 18 Schematic diagram showing the connections in the potentiostat.

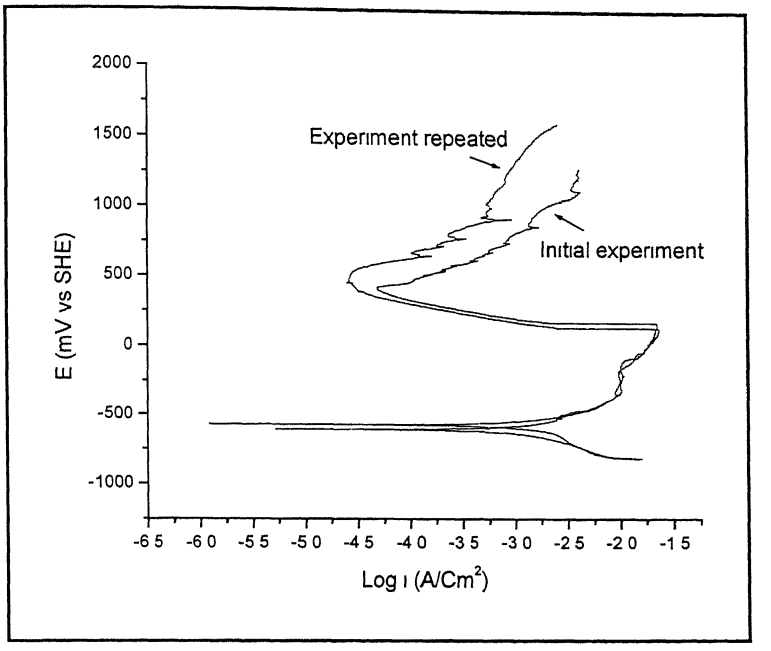

Figure 19 Polarisation behaviour of the rolling plane of the ESR137 alloy in 0.5N H_2SO_4 obtained using a flat cell at a scan rate of 0.166 mV / sec .

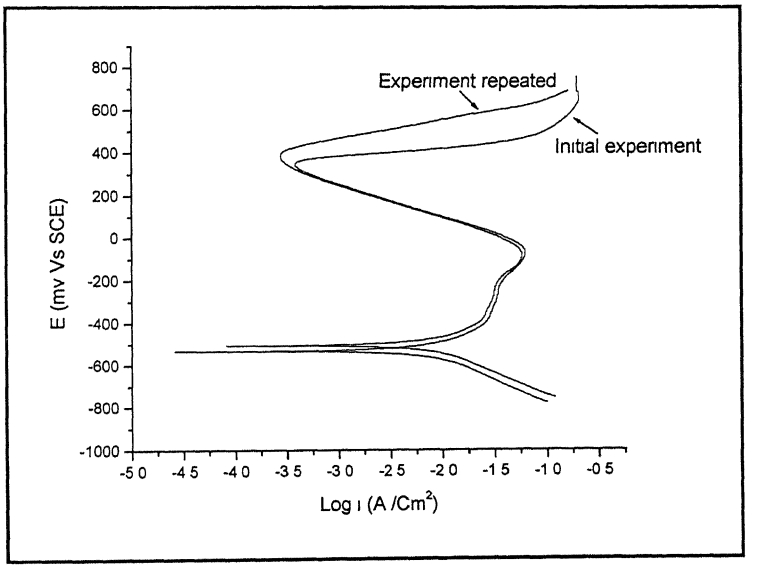

Figure 20 Polarisation behaviour of the rolling plane of the ESR137 alloy in 0.5N H_2SO_4 obtained using a round bottom cell at a scan rate of 1mV / sec.

3.4.2 Electrolytes

The following electrolytes were used in the present study to evaluate the corrosion behavior of Fe_3Al and Fe_3AlCe intermetallics.

(a) 0.5 N H_2SO_4 of pH 0.74

(b) Borate buffered solution (1.5N H_3BO_3 + 0.1N $Na_2B_4O_7$-$10H_2O$ + 0.01N KNO_3) of pH 7.6

A fixed volume of 1000 ml of test solution was used for all the tests. Although ASTM recommends 40 ml of test solution to every 1 cm^2 area of the test surface [49], it is also recommended to keep the ratio of the solution volume to specimen surface area high in order to avoid any appreciable change in the corrosivity of the solution during the test, especially since the solution would not be recirculated [49]. Only test solutions that were less than 24 hours old were used in order to minimize contamination of the electrolyte. Additional care was taken to stir the solution thoroughly before starting each test.

The temperature of the electrolytes could not be controlled using a water bath due to the shape of the polarization cell. The experiments were conducted between August 2003 (temperature 33^0C) and October 2003 (temperature 26^0C). The major difference in the solution condition between the two extremes in temperature is that the concentration of dissolved oxygen would have been slightly lower when the solution was at a higher temperature compared to that when it was a lower temperature. However since there is no major difference in the temperature of the environment this factor can be ignored. The solution were freely (naturally) aerated.

3.4.3 Test procedure for polarisation studies.

The electrolyte solution (1000 ml) was transferred to the corrosion cell. The electrodes were immersed in the electrolyte and secured in a place using a retort stand. Precaution was taken that the specimens were dipped to the same depth and the Luggin probe was adjusted so that its tip was consistently as close to the working electrode as

possible. It is well known in polarization measurements that the portion of the electrolyte between the working electrode and the capillary tip of the reference electrode also contributes towards the electrical resistance. Since resistance is a function of the distance between the electrodes, better accountability for the measured values was achieved by keeping the gap as small as possible to minimize the extra resistance

3.4.4 Potential stabilization

The free corrosion potential (E_{corr}) was monitored after immersion of the samples in the electrolyte until a steady potential was obtained. These experiments used to define the range of experimental potentials in the electrochemical experiments. Proper care was ensured so that the specimens were immersed in electrolytic solution for a minimum specified duration. Precautions were also taken to avoid any delay in starting the experiment immediately after immersing the specimen and providing the connections. The corrosion potential of the working electrode was continuously recorded starting immediately after immersion until a constant potential was obtained.

The period for stabilization depended upon the specimen, its surface finish, and the electrolyte. Generally, a constant potential was obtained within 30 minutes of immersion. Potentiodynamic polarization studies were sometimes conducted immediately after stabilised corrosion values were obtained. All the experiments were performed twice for reproducibility purposes.

3.4.5 Potentiodynamic polarization

The potentiodynamic polarization was carried out in the potential range of –1000 mV to +1600 mV for all the samples. Some experiments were started immediately after immersion of the alloy in the electrolyte. This prevented the formation of a surface film before the experiment was started. This also allowed comparison of $i_{critical}$. All potentiodynamic polarization experiments were carried out at a scan rate of 1 mV/sec. As indicated earlier the experiments were also conducted at a scan rate of 0.1666 mV/sec and the results were found unsatisfactory. The results obtained using a scan rate of

1 mV/sec (as per the recommendation of ASTM standards) was found suitable for the reliable measurement of equilibrium electrochemical characteristics for these alloys. Generally the total duration of the test was around 1.5 hours. The data was processed by the computer and stored digitally. The specimen area was taken into account during the processing of data.

3.5 Corrosion rates by immersion testing

The electrochemical methods of determining corrosion rates (ie Tafel extrapolation methods) were complemented with both short term and long term mass-loss immersion tests. This provides information about the time dependence of the process involved. Specimens of known surface area were polished to 600 grit, degreased with acetone, weighted and were immersed in 0.5N H_2SO_4 solution. The specimens were removed from the solution and the corrosion products were washed off using distilled water. Then the specimens were weighed after specific intervals of time. The specimens were again immersed in the solution after the reading was obtained. The samples were immersed for a total of 11 hours span of time and weighed after every 45 minutes in the first set of experiments. In the second set of experiment, to study the long term corrosion effect, the samples were immersed for a total of 85 hours and weighed after every 12 hours. In all the cases, the corrosion rate is given by the formula

$$\text{C.R. (in mmpy)} = (kW)/Apt \qquad \text{Eqn 18}$$

where W is the weight loss in grams (precision of 0.0001 grams), A is the surface area of the specimen in sq.cm, t is the time of exposure in hours, p is the density in gm/cc, k is a constant and its value is 87×10^3 for obtaining corrosion rate in mm per year (mmpy) [48]. The temperature was not controlled during the experiments and the experiments were conducted at slightly different climatic conditions. Therefore the temperature varied between 26°C and 33°C. The data collected from the immersion study is provided in Appendix C.

CHAPTER 4

RESULTS AND DISCUSSION

The results of microstructural and electrochemical studies on carbon-alloyed iron alumides, with and without Ce addition, will be presented and discussed in this chapter. The aim of the study is to understand the effect of Ce on the microstructure and electrochemical behaviour of the carbon-alloyed iron alumides.

4.1 Characterization of as-received material

The as received alloys, Fe-18.5Al-3.6C (ESR127), Fe-20.0Al-2.0C (ESR74) and Fe-19.2Al-3.3C-0.07Ce (ESR137) were characterized for understanding the microstructure. The microstructural characterization was performed by optical and scanning electron microscopy. The microstructures were analysed by stereological methods. The crystal structure were understood by X-ray diffraction analysis.

4.1.1 Microstructural characterization

The microstructures of the as-received iron aluminide alloys were analyzed in all the three directions.The optical micrographs and SEM microstructures of ESR74, ESR127 and ESR137 taken from the rolling plane, longitudinal and short transverse sections of the as received plate are given in Figures 21 through 29.

All the alloys possessed recrystallized grains. This was expected because the thermomechanical processing of the alloys was performed at a high temperature (550^0C to 600^0C) where dynamic recrystallization had taken place [13,14]. The alloy Fe-18.5Al-3.6C (ESR127) exhibited a typical two-phase structure (Figures 21 through 23) consisting of carbides dispersed in the iron aluminide matrix. According to Baligidad *et. al.* [18], the matrix phase is based on Fe_3Al and the precipitates are $Fe_{4-y}Al_yC_x$ carbides possessing perovskite structure. The carbides were distributed uniformly throughout the matrix of iron aluminide. The compositional analysis of the matrix for a similar alloy of similar composition indicated that for these category of alloys, the atomic ratio of iron and

aluminium in the matrix is in the order or 3:1, thereby suggesting that the stoichiometric formula of the matrix phase as Fe_3Al [52]. A similar situation is also anticipated in the alloy under investigation.

Two different types of morphology of the second phase carbide particles were observed: larger spherical and smaller nodular shaped precipitates. The size and distribution of these carbides is expected to have an effect on the corrosion behaviour of these alloys. Therefore the following discussion will focus attention on the differences in the morphology of carbides, as it has been observed in the micrographs obtained from the rolling plane, long transverse and short transverse planes of these alloys.

The carbides seen in the alloy Fe-18.5Al-3.6C (ESR127) on the rolling and longitudinal planes were of two distinct sizes. Larger bulky carbides were equally distributed throughout the matrix with many smaller precipitates interspersed in between.(Figure 21). The situation was similar in all the observed planes. (Figures 21 through 23). However, the distribution of carbides in short transverse section (Fig 23) was slightly different in that the bulky carbides were smaller in size compared to that seen in other planes and were more closely spaced. Smaller precipitates were dispersed around the bulky carbides in a similar fashion to that seen in the other planes.This probably resulted due to thermo mechanical processing.

In the case of Fe-20.0Al-2.0C (ESR74) alloy,similar bulky carbides were observed in the rolling, long transverse and short transverse planes.(Figures 24 through 26). Similarly, the smaller nodular precipitates were distributed around the bulky carbides. The distribution of carbides were uniform throughout the matrix. (Figures 24 through 26). The carbon content in Fe-20.0Al-2.0C (ESR74) was lower than in Fe-18.5Al-3.6C (ESR127). This resulted in higher volume fraction of carbide and lower spacing between the bulky carbides in the later alloy. In all the cross sections of Fe-20.0Al-2.0C, the inter carbide spacing was higher when compared to the Fe-18.5Al-3.6C alloy. Examination of these microstructure using stereological methods confirmed that the volume fraction and the exploded surface area per unit volume of the carbides in the

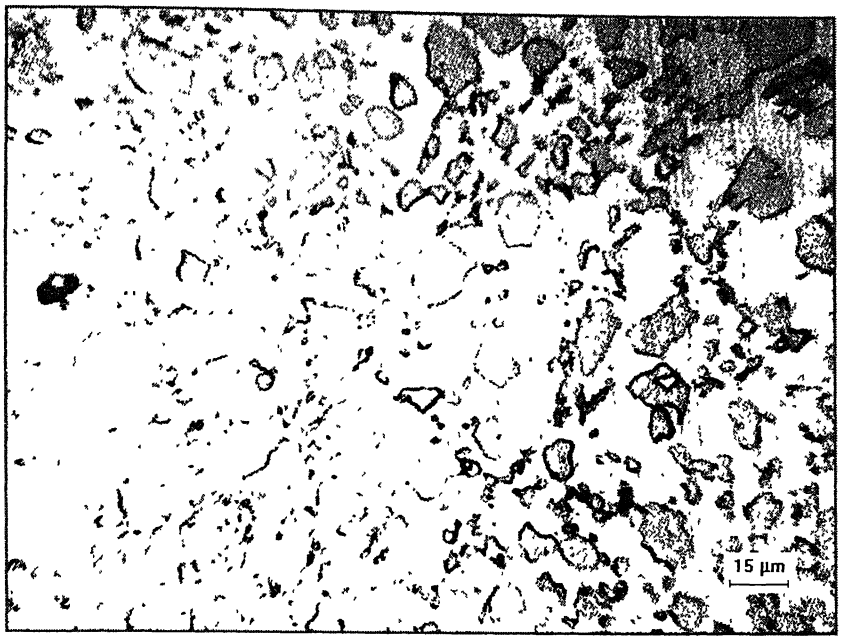

(a)

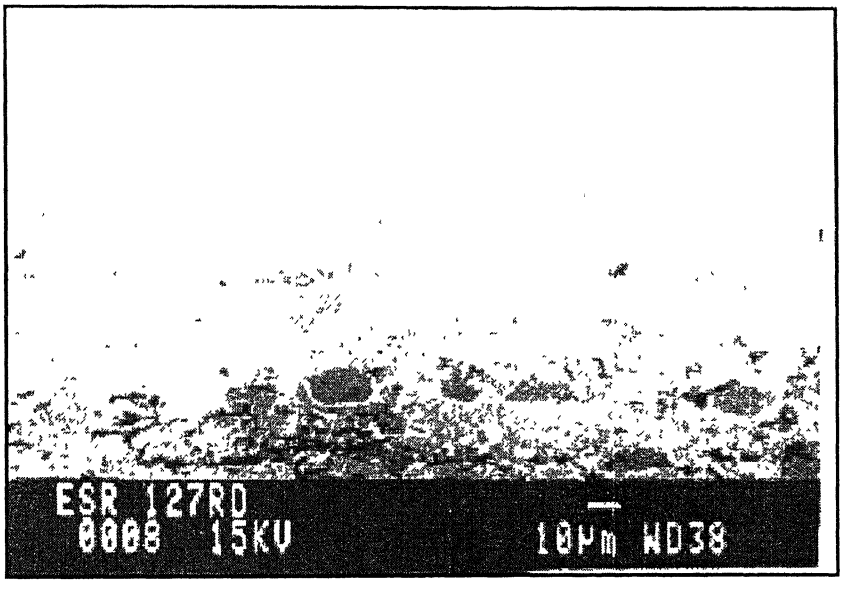

(b)

Figure 21. Microstructure of ESR127 (Fe -18.5Al-3.6C) alloy in the rolling plane as observed in a) Optical Microscope b) SEM

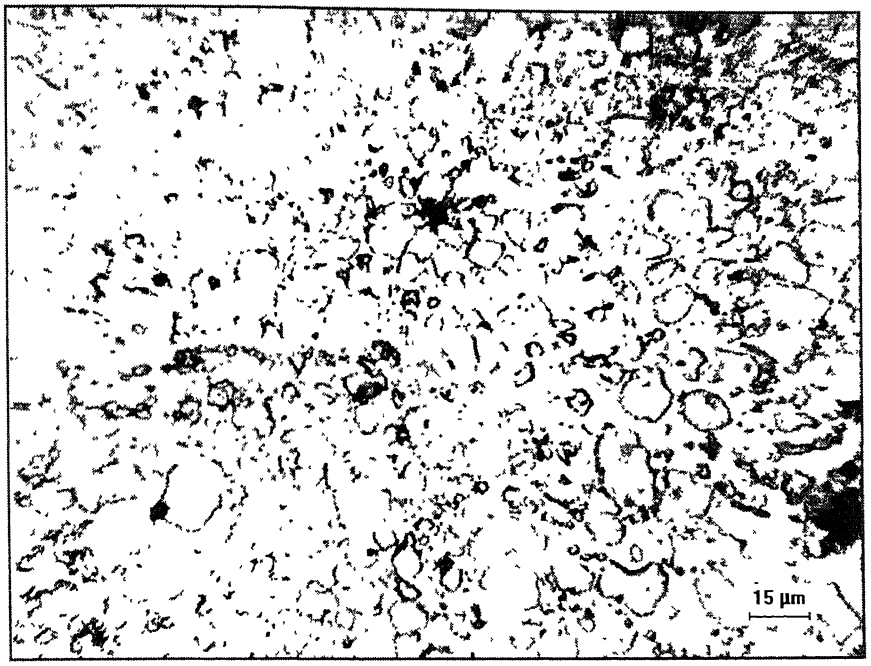

(a)

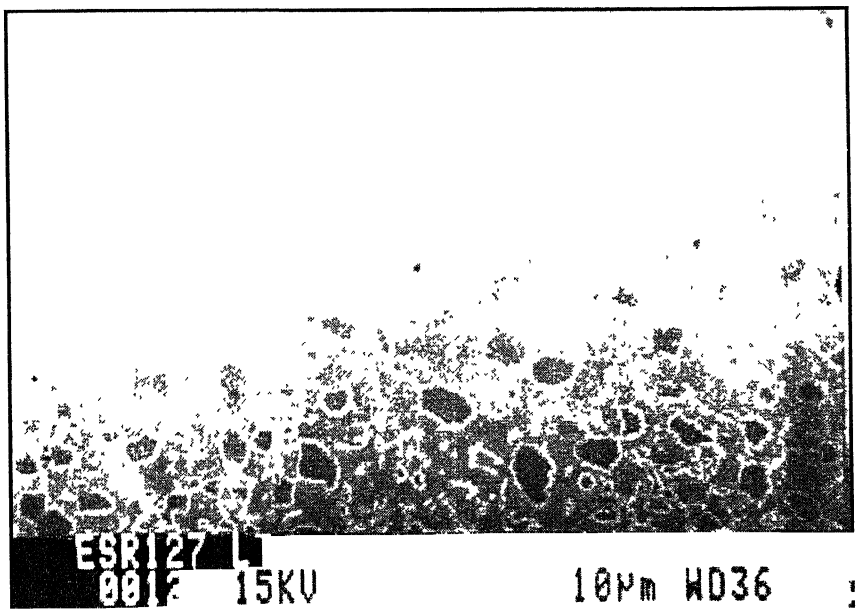

(b)

Figure 22 Microstructure of ESR127 (Fe-18.5Al-3.6C) alloy in the long transverse plane as observed in a) Optical Microscope b) SEM

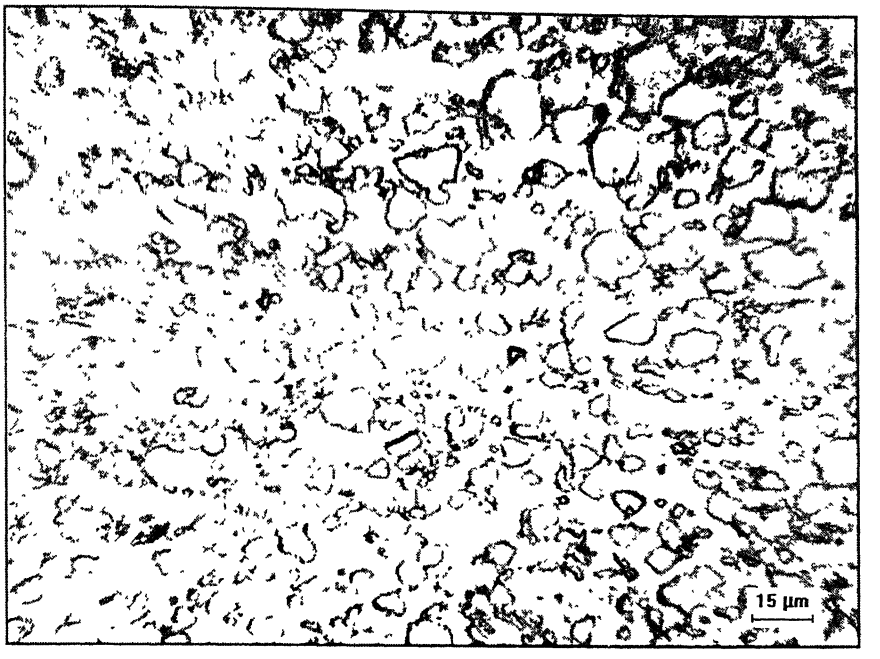

(a)

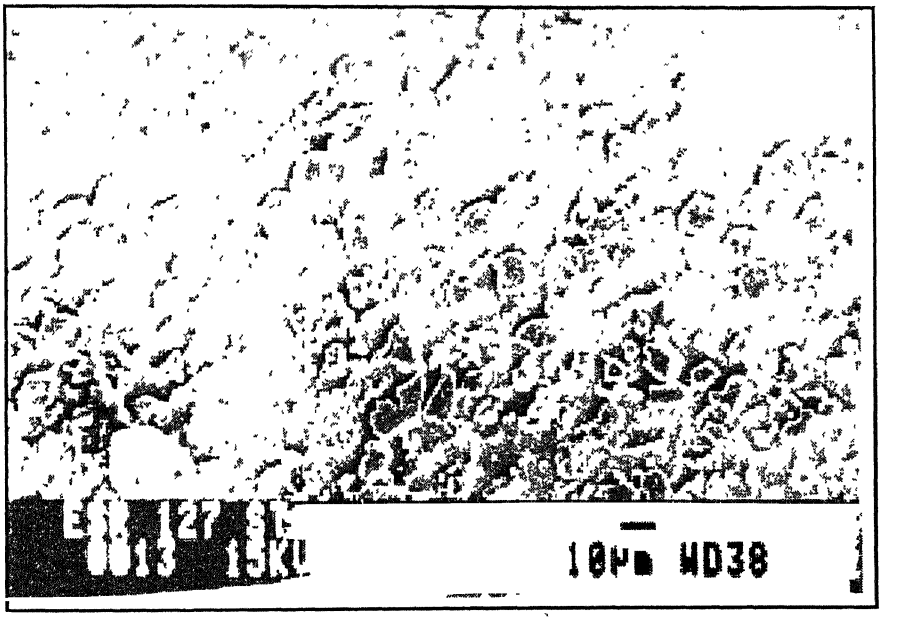

(b)

Figure 23 Microstructure of ESR127 (Fe-18.5Al-3.6C) alloy in the short transverse plane as observed in a) Optical Microscope b) SEM

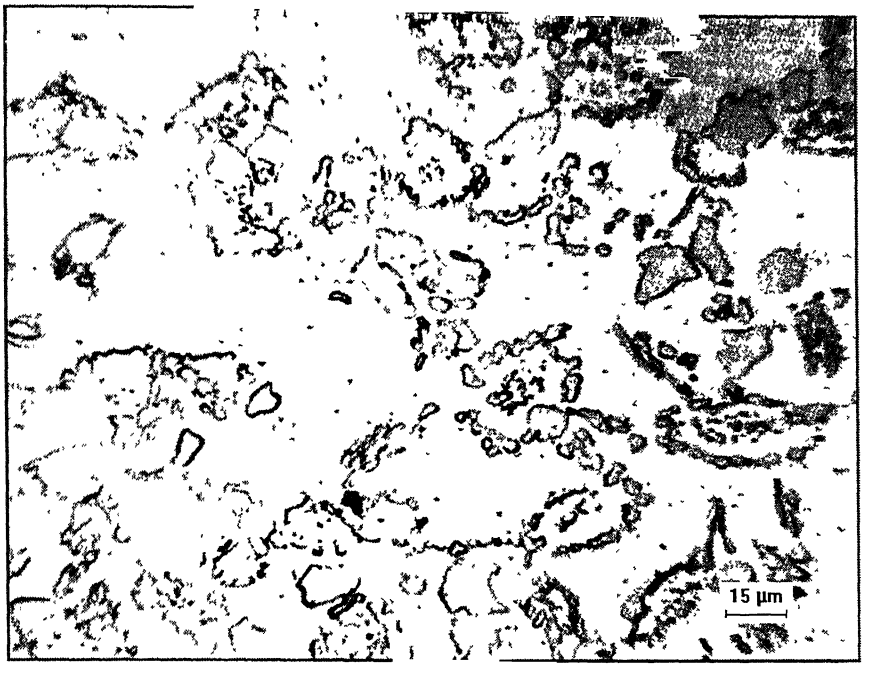

(a)

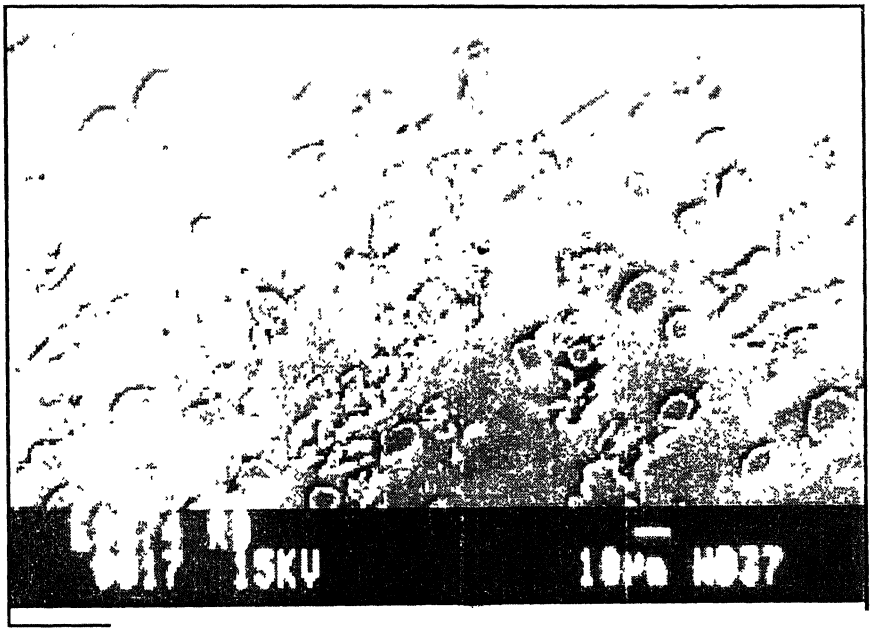

(b)

Figure 24 Microstructure of ESR74 (Fe -20.0Al-2.0C) alloy in the rolling plane as observed in a) Optical Microscope b) SEM

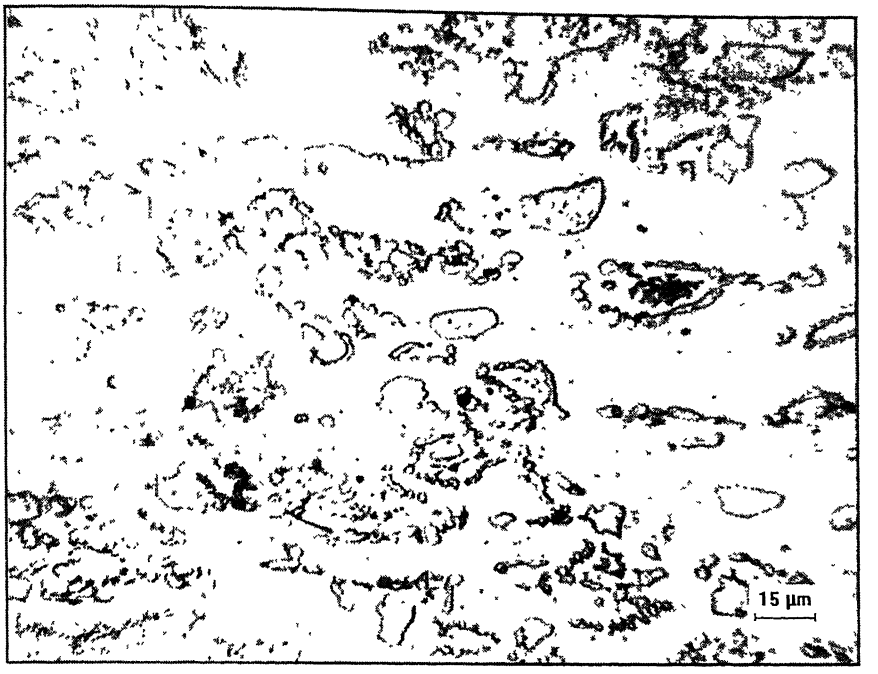

(a)

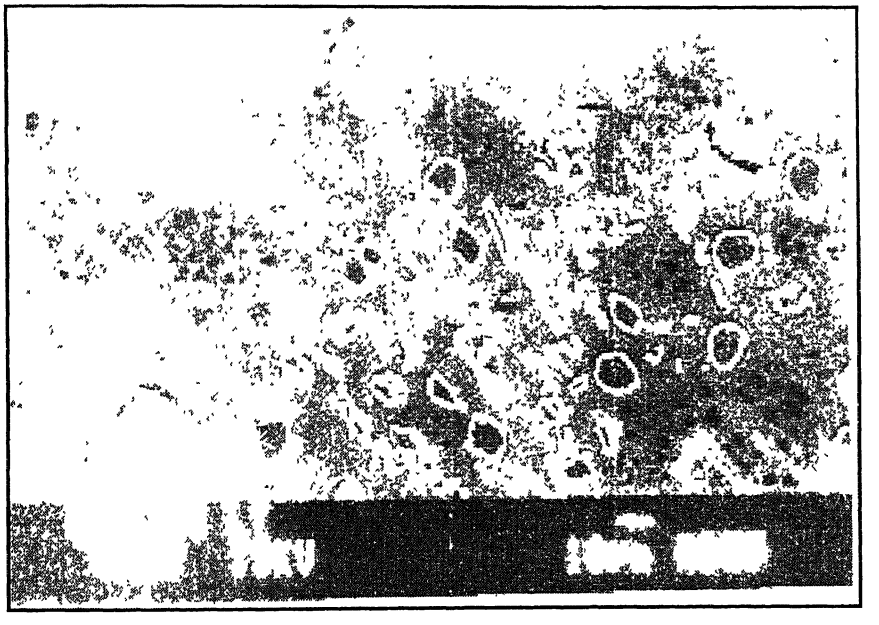

(b)

Figure 25 Microstructure of ESR74 (Fe-20.0Al-2.0C) alloy in the long transverse plane as observed in a) Optical Microscope b) SEM

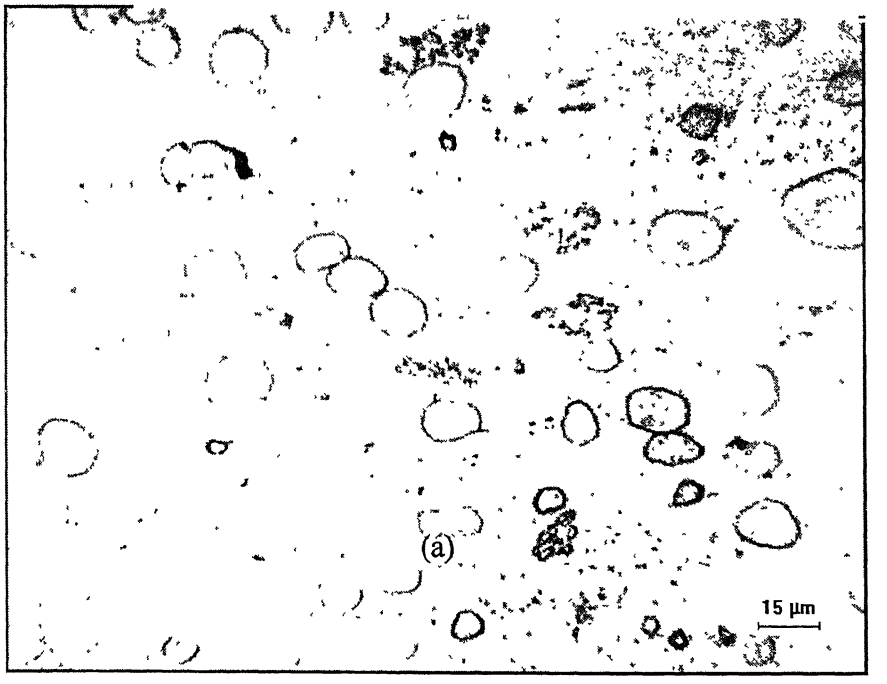

(a)

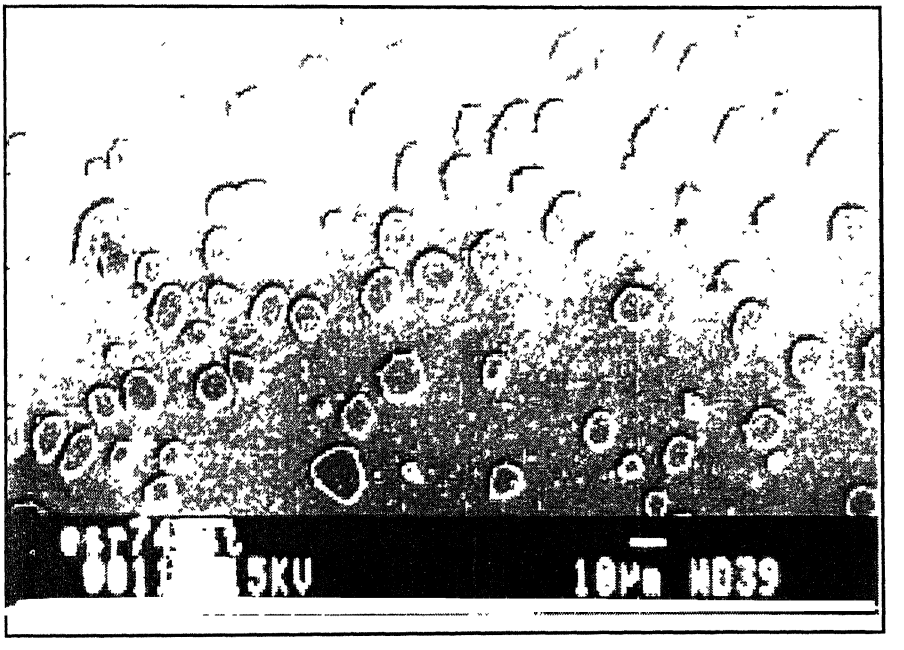

(b)

Figure 26. Microstructure of ESR74 (Fe-20.0Al-2.0C) alloy in the short transverse plane as observed in a) Optical Microscope b) SEM

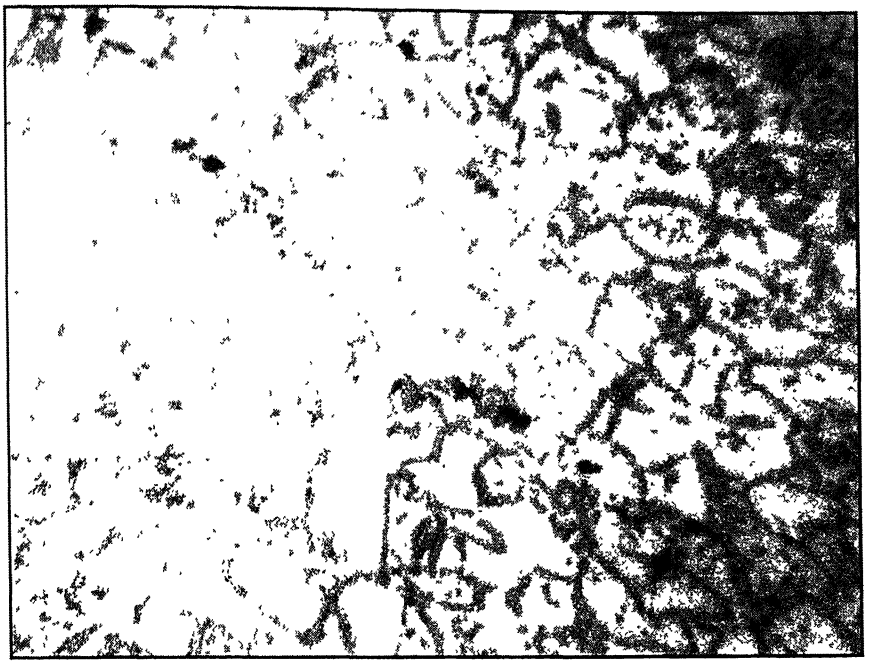

(a)

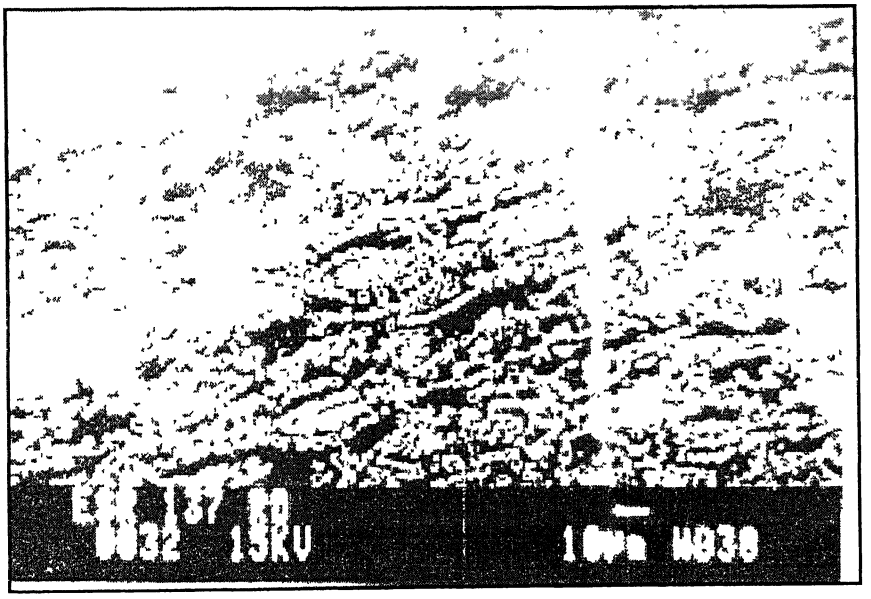

(b)

Figure 27 Microstructure of ESR137 (Fe-19.2.0Al-3.3C-0.07Ce) alloy in the rolling direction as observed in a) Optical Microscope b) SEM

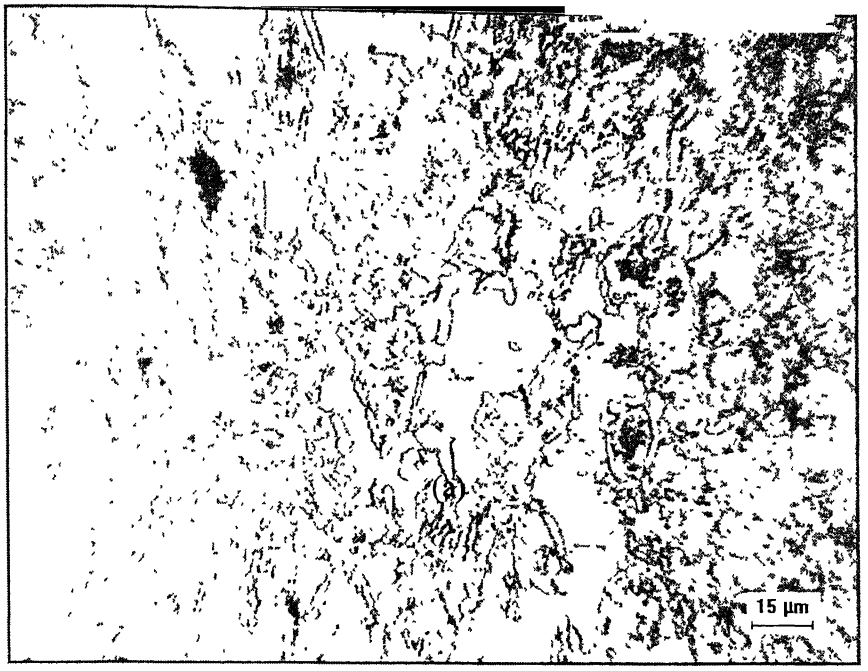

(a)

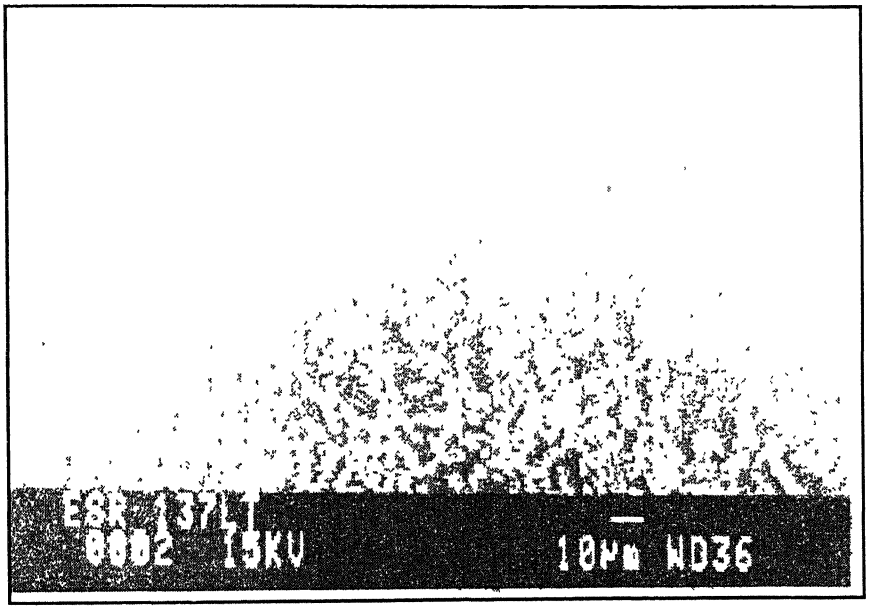

(b)

Figure 28 Microstructure of ESR137 (Fe-19.2Al-3.3C-0.07Ce) alloy in the long transverse direction as observed in a) Optical Microscope b) SEM

(a)

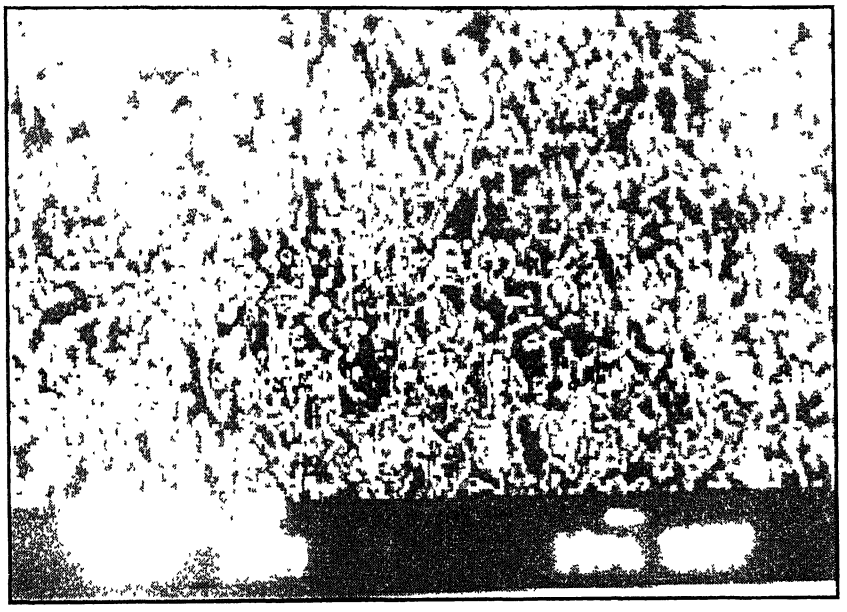

(b)

Figure 29 Microstructure of ESR137 (Fe-19.2Al-3.3C-0.07Ce) alloy in the short transverse direction as observed in a) Optical Microscope b) SEM

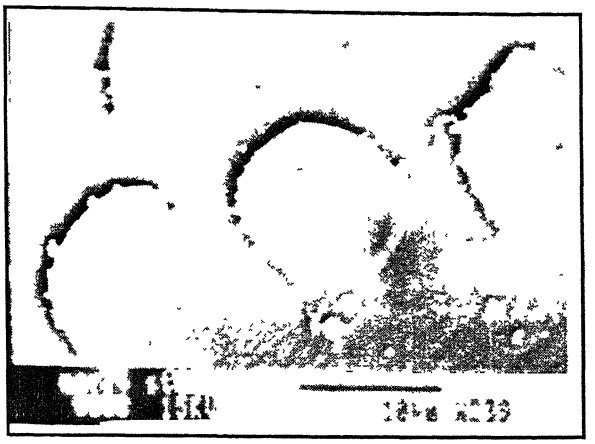

(a)

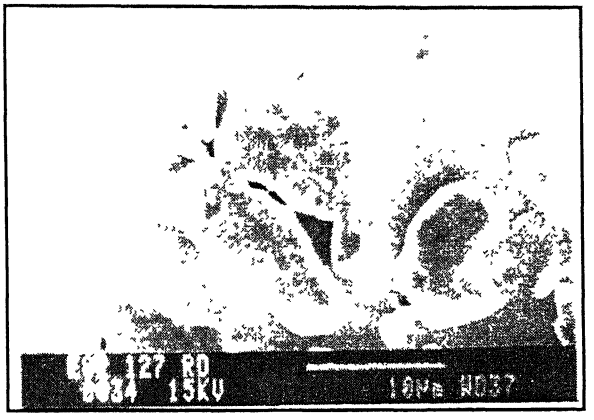

(b)

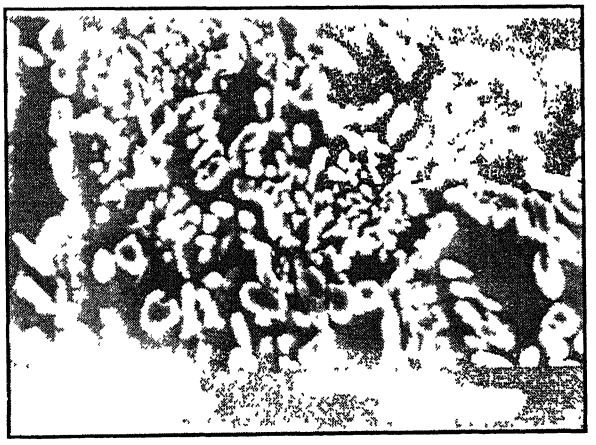

(c)

Figure 30 Microstructure of a) Fe-20.0Al-2.0C (ESR74), b) Fe-18.5Al-3.6C (ESR127) and c) Fe-19.2Al-3.3C-0.07Ce (ESR137) alloys as observed in SEM at a higher magnification.

alloy Fe-18.5Al-3.6C (ESR127) was higher than the alloy Fe-20.0Al-2.0C (ESR74). (to be discussed below) .

The addition of Ce in the alloy Fe-19.2Al-3.3C-0.07Ce modified the morphology of the carbides. (Figures 27 through 29). The microstructure of the alloy Fe-19.2Al-3.3C-0.07Ce (ESR137) was different when compared to that of ESR127 and ESR74 alloys. (Figures 21 through 26). The carbide grain sizes were finer and moreover were uniformly distributed throughout the matrix. Therefore, the addition of Ce to iron aluminides affected the morphology and size of the carbides.

It is well known that Ce is generally added in cast iron to act both as an inoculant and as a nodulariser [53]. Ce ties up the trace elements such as Pb, As, Bi, Sb, Sn, Al, Cd and Ti, which have a negative influence on the structure of the graphite. Additionally, Ce reacts with both dissolved oxygen and sulphur in the cast iron melt and forms sulphide or oxide inclusions which are of the type X_2Y_3 and XY_2, where X is Ce and Y is either sulphur or oxygen. These inclusions act as nuclei for the nucleation of graphite and hence reduces the undercooling necessary to initiate eutectic solidification. This increase in the nucleation rate of the graphite nodules in the ductile cast iron results in the formation of graphite nodules. This eventually produces the so called ductile cast iron. As S and O are effectively tied up, the morphology of graphite is changed from flakes to nodules in case of Ce-alloyed cast iron.[53]. Based on this well known effect, it is reasonable to conclude that a similar effect is influenced by Ce in the case of carbon-alloyed iron aluminides.

The microstructures of all the three planes of these alloys were also observed in the SEM. Typical SEM microstructures in the rolling plane, short transverse and long transverse plane of ESR74, ESR127 and ESR137 are presented in Figures 21 through 29. The differences in the morphology of the carbides was revealed better at higher magnifications and Figure 30 compares the structures at higher magnification.

4.1.2 Stereological analysis

The microstructures were analysed for obtaining information on the carbide particle distribution (the carbide particle size and its surface area per unit volume). The rolling plane was specifically analysed by the stereological analysis because the available area for analysis was larger for the rolling plane. Moreover, the electrochemical behaviour of the alloys was evaluated in greater detail for this section by potentiodynamic polarisation studies.

The grain size and the mean volume fraction ($\overline{V}_V$) of the bulky carbides were reported in Table 7. It was found difficult to reveal the grain boundaries in the microstructure of Fe-19.2Al-3.3C-0.07Ce (ESR137) by etching.

The surface area of exploded features per unit volume (S_V) and the contiguity for the bulky carbides were determined and these are reported in Table 8. The 95% confidence interval, which is a measure of the sampling error, is provided besides the individual measurements. As the ESR127 and ESR137 alloys possess a higher carbon content than ESR74, these alloys exhibited a higher exploded surface area per unit volume of the carbide particles. The finer carbides of all the samples were smaller in size and seen uniformly distributed and noticeable differences were seen only in the shape and size of the bulky carbides. Therefore, in estimating the above parameters, the finer particles of the carbides were neglected and the analysis was made on the bulky carbides. This provides a qualitative picture of the distribution of the larger carbide particles.

The contiguity of the bulky carbide phases were determined and reported in Table 8. The results shows that the second phase carbide phases in the samples ESR127 and ESR137 are more contiguous and proximate than the carbides in ESR74. This may be due to the higher amount of carbon in ESR 127 and ESR137. Moreover in case of the Ce added sample, ESR137, the role played by Ce in finer and uniform distribution of carbides can also be the reason for the observed higher contiguity in the Fe-19.2Al-3.3C-0.07Ce (ESR137) sample.

Table 7 Grain size and mean volume fraction ($\overline{V}_V$) of the bulky carbides distributed in the rolling plane of samples Fe-20.0Al-2.0C (ESR74) and Fe-18.5Al-3.6C (ESR127) and Fe-19.2Al-3.3C-0.07Ce (ESR137) samples

Alloy	Composition	Grain Size		Volume fraction of bulky carbides	
		Mean μm	95% confidence interval	Mean	95% confidence interval
ESR74	Fe-20.0Al-2.0C	480.48	54.10	0.20	0.0353
ESR127	Fe-18.5Al-3.6C	574.91	85.90	0.33	0.0406
ESR 137	Fe-19.2Al-3.3C-0.07Ce	-	-	0.35	0.0457

Table 8 Exploded surface area per unit volume, and contiguity of the carbides distributed in the rolling plane of Fe-20.0Al-2.0C (ESR74), Fe-18.5Al-3.6C (ESR127) and Fe-19.2Al-3.3C-0.07Ce (ESR137) samples

Alloy	Composition	Exploded surface area per unit volume (μm^{-1})		Contiguity	
		Mean (μm^{-1})	95% confidence interval	Mean	95% confidence interval
ESR74	Fe-20.0Al-2.0C	0.230	0.0364	0.065	0.0201
ESR127	Fe-18.5Al-3.6C	0.247	0.0146	0.160	0.0317
ESR 137	Fe-19.2Al-3.3C-0.07Ce	0.237	0.0146	0.114	0.0344

4.1.3 Structural analysis

The structure of the matrix and carbides was understood by X-ray diffraction. The diffraction patterns of the as-received alloys ESR74, ESR127 and ESR137 using CuK_α (λ = 0.15045) radiation is shown in Figures 31 through 33 respectively. The patterns were analysed and the results were tabulated in the Tables 9 through 11.

The major peaks belonged to Fe_3Al. After indexing the peaks of Fe_3Al, the smaller peaks were indexed to the carbide Fe_3AlC. It was assumed that the 100% carbide peak was the strongest carbide peak and the relative intensities for the carbide peaks were then obtained with reference to this peak. X ray diffraction patterns confirmed that the presence of carbon leads to the formation of Fe_3AlC precipitates in the matrix.

The Fe_3AlC phase possesses a FCC crystal structure with Al atoms occupying the corners of the cube, Fe atoms at the face centers and the carbon atom at the body center position (i.e. the octahedral void at ½, ½, ½) (Figure 3) .The lattice parameters of the carbide and non carbide phases is presented in Table 12.The published lattice parameter (a) of the carbides is 0.377 nm [54] while indexing of carbide peaks in the pattern provided a lattice parameter of 0.374 nm for the non cerium alloys and 0.369 for the cerium alloyed samples. The slight mismatch of the calculated lattice parameter with the published lattice parameter was explained to result due to the relative small number of d_{hkl} values utilized to calculate the lattice parameter [54].

The Ce-alloyed intermetallics did not exhibit any additional diffraction peaks (Figure 33) apart from the peaks that were obtained in the Figures 31 and 32 as in the case of the base intermetallics. Therefore, it can be concluded that Ce additions essentially enter into solid solution in the Fe_3Al matrix or in the interfacial region between carbide and the matrix.

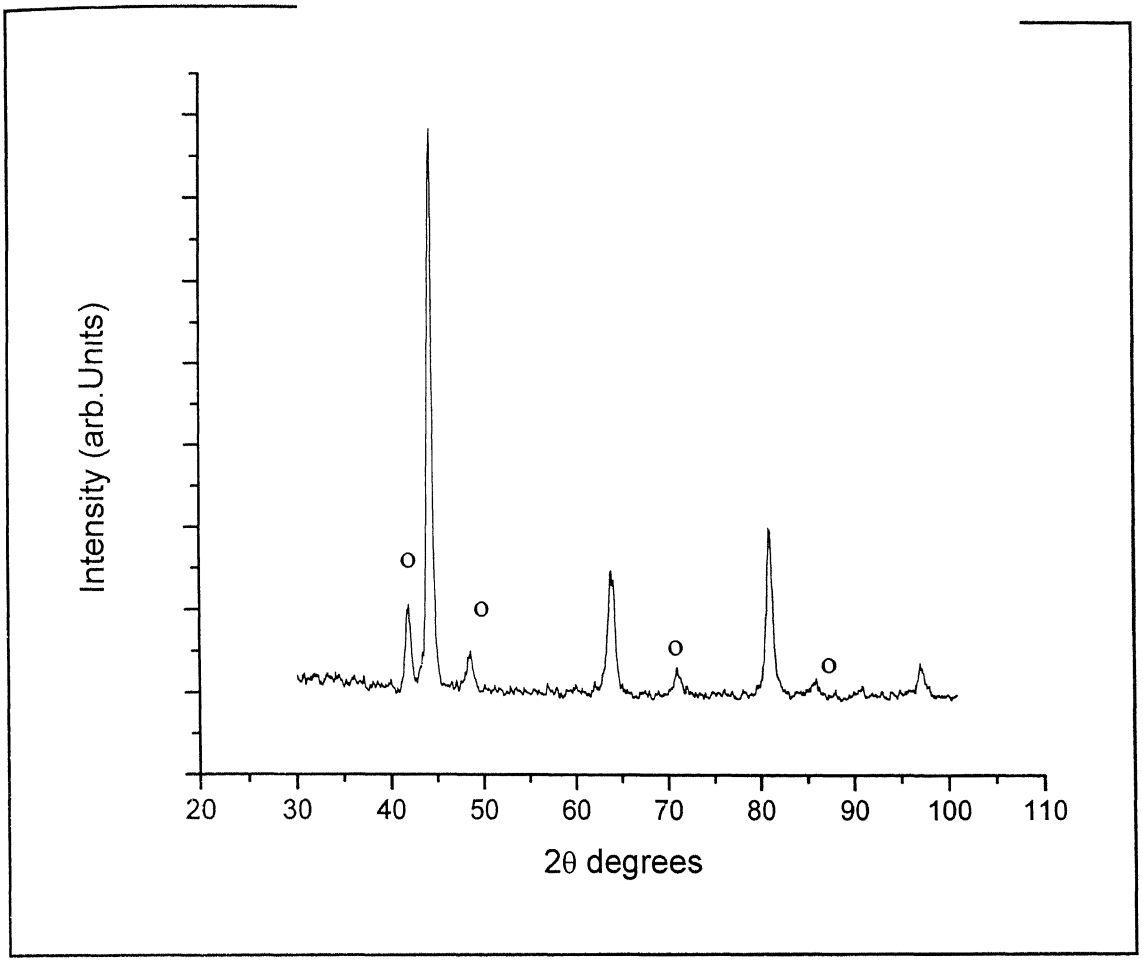

Figure 31 XRD pattern of as received Fe-20.0Al-2.0C (ESR74) alloy using Cu Kα (λ = 0.015405 nm) radiation. The peaks due to the carbide phase (Fe_3AlC) have been marked **o**

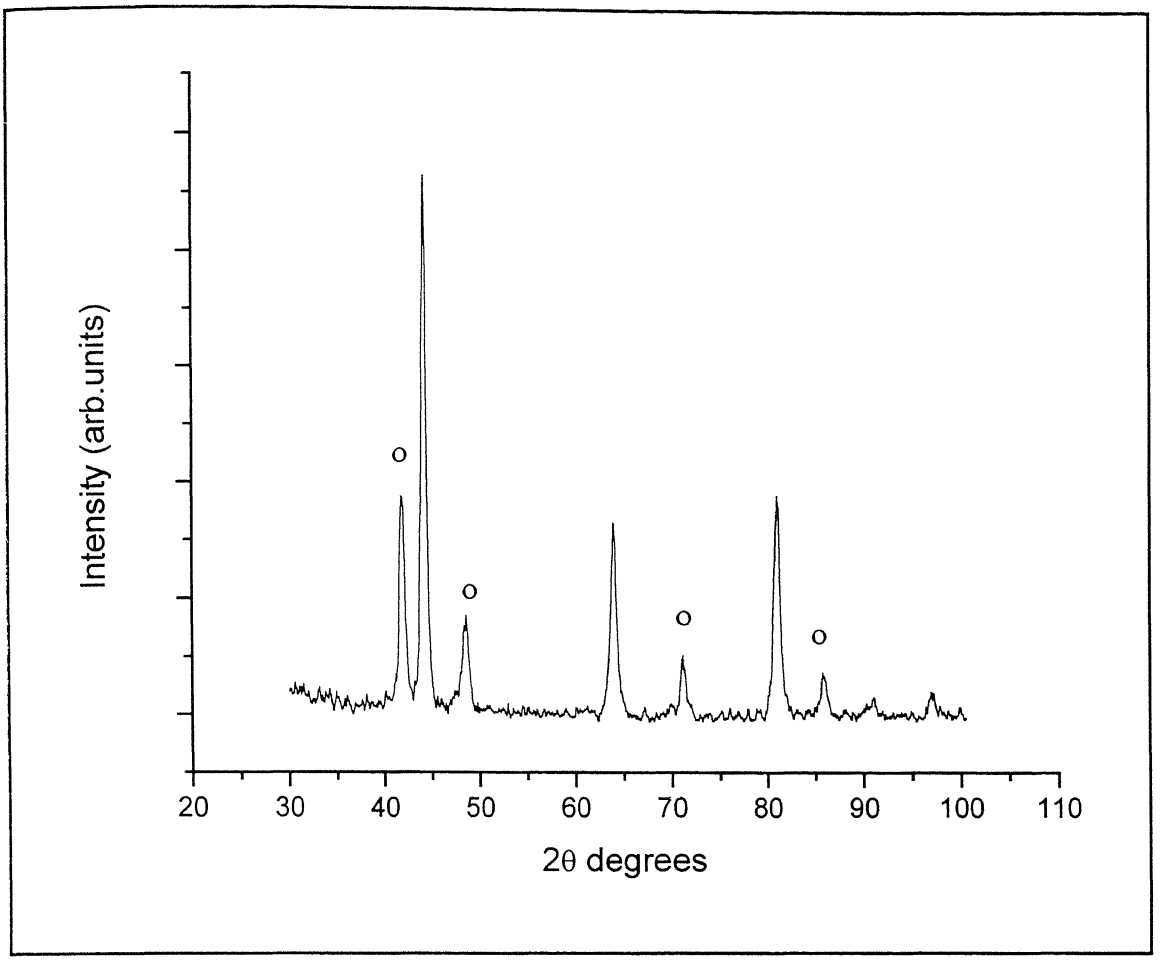

Figure 32 XRD pattern of as received Fe-18.5Al-3.6C (ESR127) alloy using Cu Kα (λ = 0.015405 nm) radiation. The peaks due to the carbide phase (Fe_3AlC) have been marked **o**

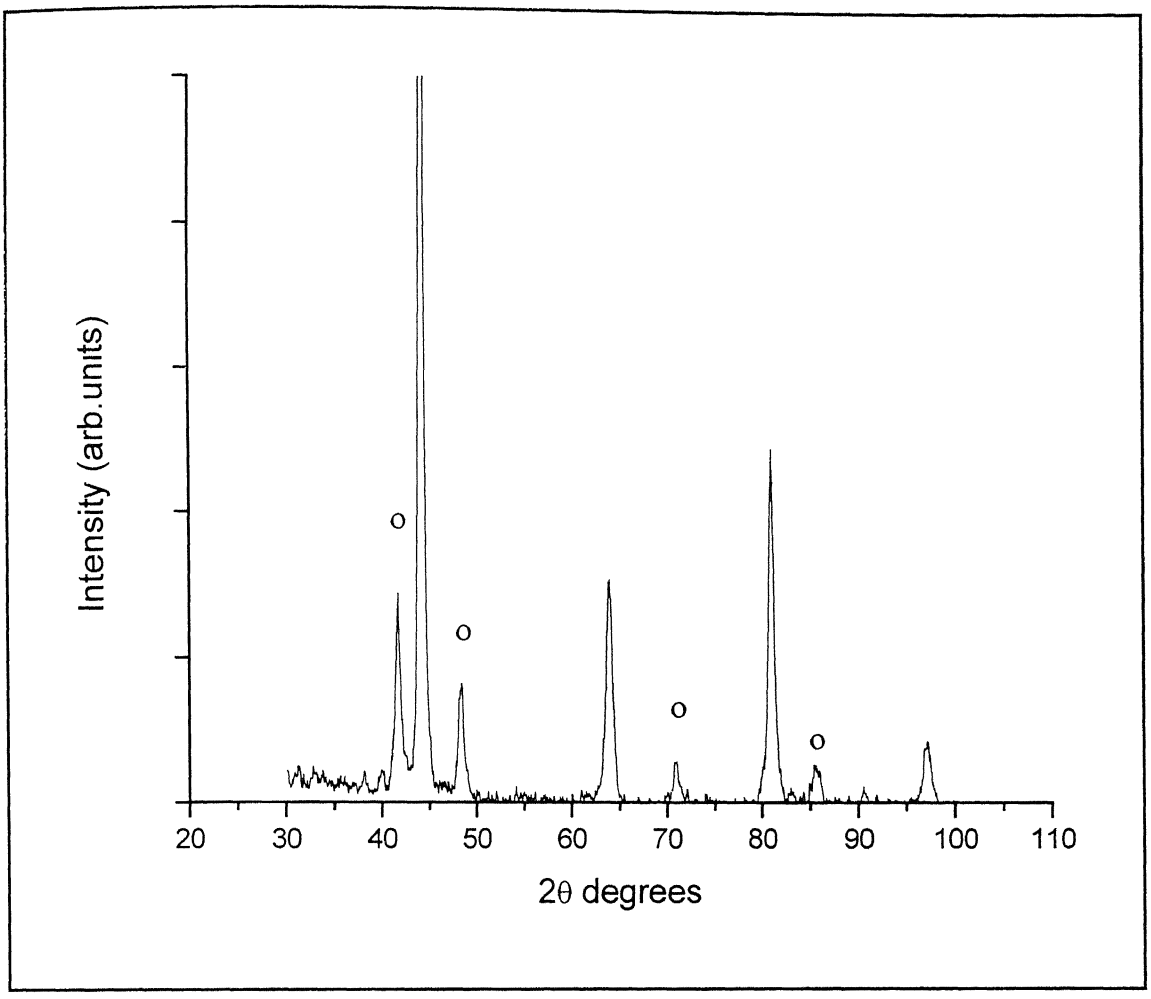

Figure 33 XRD pattern of as received Fe-19.2Al-3.3C-0.07Ce (ESR137) alloy using Cu Kα (λ = 0.015405 nm) radiation. The peaks due to the carbide phase (Fe_3AlC) have been marked **o**

Table 9 Analysis of the X ray diffractogram of Fe-19.2Al-3.3C-0.07Ce (ESR137) alloy using CuKα (λ = 0.15405 nm). Obs = Observed , Theo = Theoretical

Line#	$2\theta_{obs}$	$2\theta_{theo}$	hkl_{obs}	hkl_{theo}	d_{hkl} (A°) obs	d_{hkl} (A°) theo	$(I/Io)\%_{obs}$	$(I/Io)\%_{theo}$	Phase
1	41.62	41.43	111	111	2.169	2.17	18.11	100	$Fe_3AlC_{0.5}$
2	44.09	44.37	220	220	2.053	2.03	100	100	Fe_3Al
3	48.32	48.24	200	200	1.883	1.88	9.90	47	$Fe_3AlC_{0.5}$
4	64.07	81.50	400	400	1.453	1.18	20.8	90	Fe_3Al
5	71.06	70.60	311	311	1.326	1.33	3.47	18	$Fe_3AlC_{0.5}$
6	81.17	64.18	422	422	1.840	1.44	28.8	80	Fe_3Al

Table 10 Analysis of the X ray diffractogram of Fe-20.0Al-2.0C (ESR74) alloy using CuKα (λ = 0.15405 nm). Obs = Observed , Theo = Theoretical

Line#	$2\theta_{obs}$	$2\theta_{theo}$	hkl_{obs}	hkl_{theo}	d_{hkl} (A°) obs	d_{hkl} (A°) theo	$(I/Io)\%_{obs}$	$(I/Io)\%_{theo}$	Phase
1	41.76	41.43	111	111	2.16	2.17	14.79	100	$Fe_3AlC_{0.5}$
2	44.12	44.37	220	220	2.05	2.03	100	100	Fe_3Al
3	48.49	48.24	200	200	1.88	1.88	6.69	47	$Fe_3AlC_{0.5}$
4	63.87	81.50	400	400	1.45	1.18	20.8	90	Fe_3Al
5	71.05	70.60	311	311	1.33	1.33	4.72	18	$Fe_3AlC_{0.5}$
6	81.10	64.18	422	422	1.18	1.44	28.8	80	Fe_3Al

Table 11 Analysis of the X ray diffractogram of Fe-18.5Al-3.6C (ESR127) alloy using CuKα (λ = 0.15405 nm). Obs = Observed , Theo = Theoretical

Line#	$2\theta_{obs}$	$2\theta_{theo}$	hkl_{obs}	hkl_{theo}	d_{hkl} (A°) obs	d_{hkl} (A°) theo	$(I/Io)\%_{obs}$	$(I/Io)\%_{theo}$	Phase
1	41.84	41.43	111	111	2.16	2.15	40.06	100	$Fe_3AlC_{0.69}$
2	44.15	44.37	220	220	2.05	2.05	100	100	FeAl
3	48.52	48.24	200	200	1.88	1.87	16.76	47	$Fe_3AlC_{0.69}$
4	64.02	81.50	400	400	1.45	1.45	35.11	90	FeAl
5	71.20	70.60	311	311	1.33	1.32	11.06	18	$Fe_3AlC_{0.69}$
6	81.18	64.18	422	422	1.18	1.18	39.85	80	FeAl

Table 12. Lattice parameters of the carbide and non carbide phases of ESR74, ESR127 and ESR137 alloys.

Line#	$2\theta_{obs}$	hkl_{obs}	d_{hkl} (A°) obs	Lattice Parameter (A ∘)	Phase
Fe-20.0Al-2.0C (ESR 74)					
1	41.84	111	2.16	3.74	$Fe_3AlC_{0\,69}$
2	44.15	220	2.05	5.80	FeAl
3	48.52	200	1.88	3.76	$Fe_3AlC_{0\,69}$
4	64.02	400	1.45	5.80	FeAl
5	71.20	311	1.33	4.41	$Fe_3AlC_{0\,69}$
6	81.18	422	1.18	5.78	FeAl
Fe-18.5Al-3.6C (ESR 127)					
1	41.84	111	2.16	3.74	$Fe_3AlC_{0\,69}$
2	44.15	220	2.05	5.80	FeAl
3	48.52	200	1.88	3.74	$Fe_3AlC_{0\,69}$
4	64.02	400	1.45	5.80	FeAl
5	71.20	311	1.33	4.38	$Fe_3AlC_{0\,69}$
6	81.18	422	1.18	5.78	FeAl
Fe-19.2Al-3.3C-0.07Ce (ESR 137)					
1	41.84	111	2.16	3.769	$Fe_3AlC_{0\,69}$
2	44.15	220	2.05	5.81	FeAl
3	48.52	200	1.88	3.77	$Fe_3AlC_{0\,69}$
4	64.02	400	1.45	5.81	FeAl
5	71.20	311	1.33	4.40	$Fe_3AlC_{0\,69}$
6	81.18	422	1.18	9.01	FeAl

4.1.4 Microhardness characterization

The microhardness of the bulky carbides and the matrix were measured for the alloys Fe-20.0Al-2.0C and Fe-18.5Al-3.6C. A 50 gram load was applied during the measurement of hardness and this provided optimum size of indentation. Hardness measurements of the finer carbides in the Ce added alloy Fe-19.2Al-3.3C-0.07Ce were not possible because proper indentations could not be made due to the small size of these carbides. Therefore the data reported in Table 13 has been placed within the brackets due to the uncertainties. A 10 gram load was tried during the measurement of hardness in this alloy and the size of the indentation was observed to be too small and the measurement error of the diagonal was high. On the other hand if a higher load was applied in order to make the indentation, the indentation mark could overlap some nearby phase. Table 13 reports hardness for the bulky carbides and Table 14 reports that for the matrix. It is observed from Tables 13 and 14 that the carbides and matrix of the sample Fe-20.0Al-2.0C exhibited higher hardness though it contained lower carbon. The increase in hardness of the carbides could be probably due to the higher aluminium content of the alloy which forms a hard $Fe_{4-y}Al_yC_x$ phase. The hardness of the matrix in all the alloys were comparable (Table 14).

Table 13 Microhardness of bulky carbides for ESR74, ESR127 alloys using a 50 gram load and ESR137 alloy using a 10 gram load.

Alloy	Composition	Diagonal (mm)	SD	FOV	%Error, +-	Hardness kg/mm^2
ESR 74	Fe-20.0Al-2.0C	13.67	0.44	10	2.06	501.2
ESR127	Fe-18.5Al-3.6C	15.14	0.79	10	3.32	408.3
ESR137	Fe-19.2Al-3.3C-0.07Ce	(5.76)	(0.61)	(10)	(6.67)	(581.6)

Table 14 Microhardness of matrix for ESR74, ESR127 and ESR137 alloys using a 50 gram load and ESR137 alloy using a 10 gram load.

Alloy	Composition	Diagonal (mm)	SD	FOV	%Error, +-	Hardness kg/mm^2
ESR 74	Fe-20.0Al-2.0C	16.20	0.72	10	2.80	359.6
ESR127	Fe-18.5Al-3.6C	16.34	0.37	10	1.45	347.7
ESR137	Fe-19.2Al-3.3C-0.07Ce	7.27	0.63	10	3.16	361.3

4.2 Electrochemical behavior

4.2.1 Stabilisation of free corrosion potential

The nature of stabilization of the free corrosion potential (FCP) in 0.5N H_2SO_4 acid solution provides information about the nature of the film that forms on the surface of materials under free corrosion conditions [55]. If the FCP moves from an active to noble potential during stabilization, it suggests dissolution of the film that forms under free corrosion conditions and an equilibrium FCP is attained when the dissolution rate equals the growth rate of the film. In case the FCP moves from noble to active potential during stabilization, the equilibrium potential is attained when the dissolution rate equals the film growth rate. This possibly indicates that the film that forms in this case is more protective. Incase the FCP stabilizes immediately upon immersion, it implies that the equilibrium conditions are attained relatively fast.

The stabilization of the free corrosion potentials in the acidic solution of 0.5N H_2SO_4 for the carbon-alloyed intermetallics ESR74 and ESR127 used in the present study are presented in the Figure 34. The FCP of the intemetallics stabilize in the range of –0.50 V to -0.54 V vs SCE in almost all the cases. The nature of the stabilization curves are similar for all the cases. The potentials move from active to noble potentials on stabilization. The nature of the stabilization curve for the Ce-alloyed intermetallic ESR137 was slightly different. The FCP stabilized immediately on immersion (Figure 34). An interesting trend was noticed in the case of Ce-alloyed intermetallic when compared to the non Ce-alloyed intermetallics. Although the FCP stabilsation curve appears flat in Figure 34, on magnifying the scale of the potential axis, a consistent trend in the FCP variation was observed for the Ce-alloyed iron aluminide. This is shown in Figure 35. The general trend seen was that the potential initially moved from noble to active potential, then eventually shifted to a noble potential, and finally stabilized around -0.535 mV vs SCE. The time for stabilization was around 2000 seconds. Interestingly this behaviour was noticed in all the sections i.e RD, LT and ST (Figure 35).

The stabilized free corrosion potentials for the intermetallics in acidic medium are tabulated in Table 15. The zero current potential obtained from the polarization curves (to be discussed below) has also been presented in the Table 15.

In the potentiodynamic polarization experiments conducted in the borate buffered solution of pH 7.6, the free corrosion potential of the alloys were not stabilized and the experiments were conducted immediately after immersion of the samples in the electrolyte. Therefore, the stabilization of free corrosion potential has not been provided in the borate buffered solution.

Table 15 Free corrosion potential (Ecorr) and zero current potential (ZCP) of the intermetallics in 0.5N H_2SO_4. All the potentials are in volts vs SCE

Nomenclature	Intermetallics	Section	Ecorr V vs SCE	ZCP V vs SCE
ESR74	Fe-20.0Al-2.0C	Rolling	-0.514	-0.515
ESR127	Fe-18.5Al-3.6C	Rolling	-0.502	-0.501
ESR137	Fe-19.2Al-3.3C-0.07Ce	Rolling	-0.530	-0.511
ESR137	Fe-19.2Al-3.3C-0.07Ce	Long transverse	-0.504	-0.548
ESR137	Fe-19.2Al-3.3C-0.07Ce	Short transverse	-0.515	-0.524

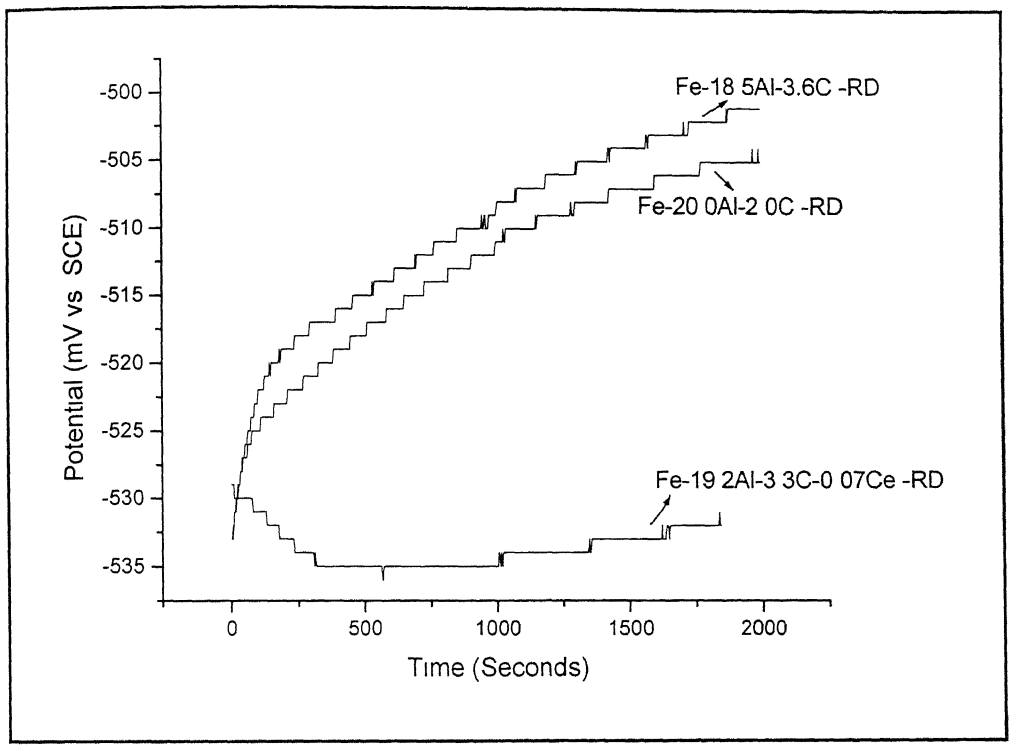

Figure 34 Variation in free corrosion potential as a function of time for Fe-20.0Al-2.0C (ESR 74), Fe-18.5Al-3.6C (ESR 127) and Fe-19.2Al-3.3C-0.07Ce (ESR 127) alloys in freely-aerated 0.5N H_2S0_4

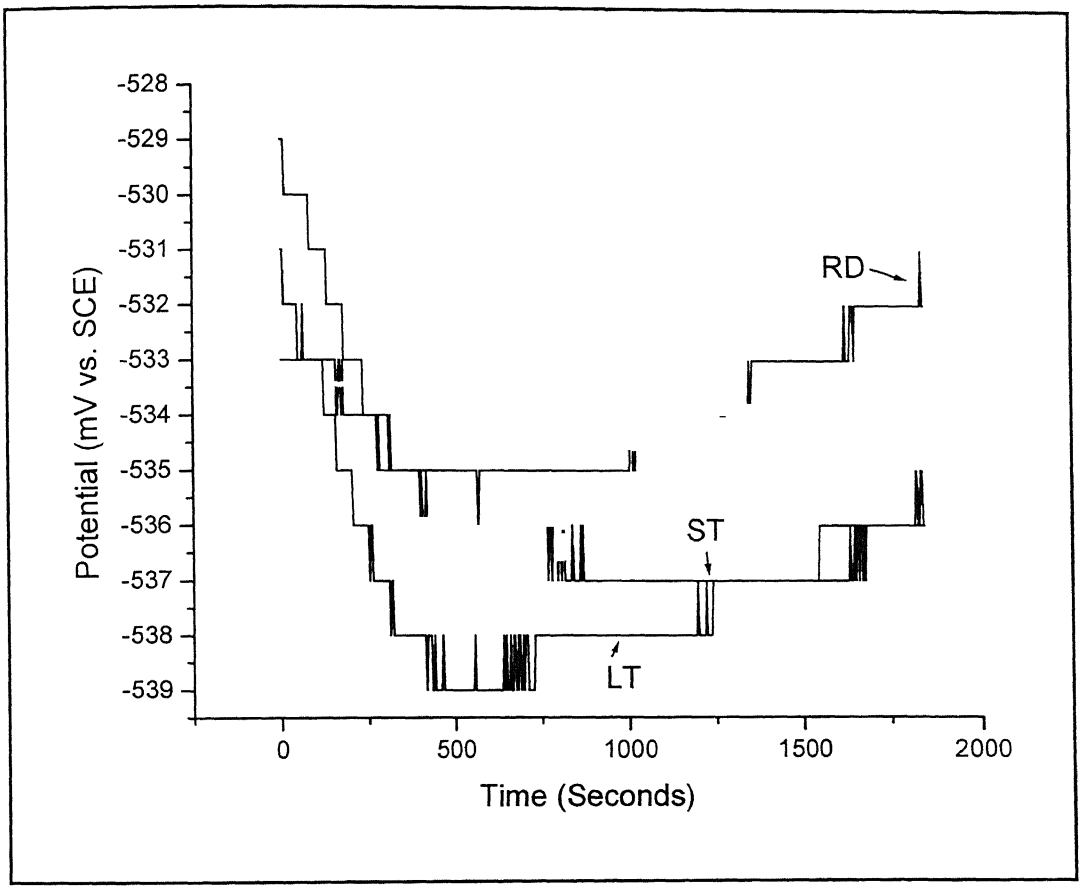

Figure 35 Variation in free corrosion potential as a function of time for Fe-19.2Al-3.3C-0.07Ce for the rolling plane (RD), long transverse plane (LT), and short transverse planes (ST), in freely aerated 0.5N H_2SO_4

4.2.2 Polarisation behaviour in acidic solution

The potentiodynamic polarisation behavior for the alloys ESR74, ESR127 and ESR137 alloy were studied in freely aerated 0.5N H_2SO_4 (pH of 0.74). In all the studies the rolling plane was specifically addressed. All the experiments were duplicated two times for accuracy and the results were found highly reproducible. The duplicate data for all the tests are provided in Appendix D.

The potentiodynamic polarization curves for Fe-18.5Al-3.6C and Fe-20.0Al-2.0C in the acidic 0.5N H_2SO_4 solution are presented in Figure 36. Both the alloys exhibited active passive behaviour which means that there is a region where the current density is lowered on polarizing past the zero current potential. The zero current potential (E_{zcp}), corrosion current density (i_{corr}), passive current density (i_{pass}), critical current density (i_{crit}), passive potential (E_{pp}), and completion of passivation potential (Ecp) obtained from the polarisation curves have been tabulated in Table 16. On comparison of the i_{pass} and i_{crit} values of the above two alloys, we see that the i_{crit} increases with the increase in carbon addition. The alloy Fe-20.0Al-2.0C, which has a lower carbon content, exhibited a comparatively lower critical current density. The passivation parameters are generally comparable between the two alloys ESR74 and ESR127. This is reasonable because the carbon contents are not significantly different and moreover the carbide distribution in these alloys was similar.

The potentiodynamic polarization curve for all the sections of Fe-19.2Al-3.3C-0.07Ce in the freely aerated 0.5N H_2SO_4 solution is presented in Figure 37. The Ce-alloyed sample also exhibited active passive behaviour. The effect of the addition of Ce to the intermetallics become more clear when the polarization curves of alloys Fe-18.5Al-3.6C and Fe-19.2Al-3.3C-0.07Ce are compared, as these two alloys have almost equal aluminum and carbon contents. (refer Table 16). The most important difference from the other carbon-alloyed iron aluminide is the low passive range of the Ce-alloyed iron aluminide. Moreover i_{crit} for the RD plane of Ce-alloyed aluminide was lower compared to the other alloys. (Table 16). The passive current densities of the alloys were comparable and so were the other passivation properties. An interesting result is the

relatively better passivation properties (ie higher E_b and the passivation range) obtained in the LT section for the Ce-alloyed aluminide (Figure 37 and Table 16). The lower values of i_{pass} for the rolling plane and the long transverse plane indicates that the addition of Ce influences the nature of the passive film beneficially. However these values are higher for the short transverse plane of Fe-19.2Al-3.3C-0.07Ce. It seems therefore that the passive film formed is quite weak and hence there is a preferential dissolution of carbides which causes a higher passive current density in this plane, when compared to the rolling and the longitudinal planes where the passive film is more stable. This surface pits heavily once the breakdown potential is attained and a large current density is drawn because of this reason. As already noted the addition of Ce resulted in a finer distribution of the carbides (ie smaller sizes) through the alteration of the microstructure. As carbides are potential cathodic sites, the number of cathodic sites must increase with Ce addition For this kind of a morphology, a higher corrosion rate is anticipated, but since the corrosion for Ce-alloyed material was lower, it appears that Ce addition would have modified the surface film which results in passivation.[51]

The corrosion rates for all the samples were determined from the Tafel curves by the Tafel extrapolation method . The results of the Tafel experiments is given in Figure 38. Values of β_a, β_c and i_{corr} obtained from the Tafel curves of carbon-alloyed iron alumindes in are presented in Table 17. The corrosion rates and Tafel slopes were comparable for the carbon-alloyed aluminides. However, the corrosion rates for the Ce-alloyed aluminide was lower in all the planes compared to the other two aluminides. This trend was also seen in the results obtained from the weight loss method.

The corrosion rates were also determined by the polarisation resistance method by measuring the slope of the linear polarisation curves. (Figure 39). The corrosion rate thus obtained is presented in Table 18. It was observed that the corrosion rates for all the alloys obtained by linear polarisation method is comparatively higher than those obtained using the Tafel extrapolation method. This can be attributed to the ohmic resistance interferences in the potential measurements [47]. The results obtained from duplicated experiments of linear polarisation resistance method is given in Appendix E.

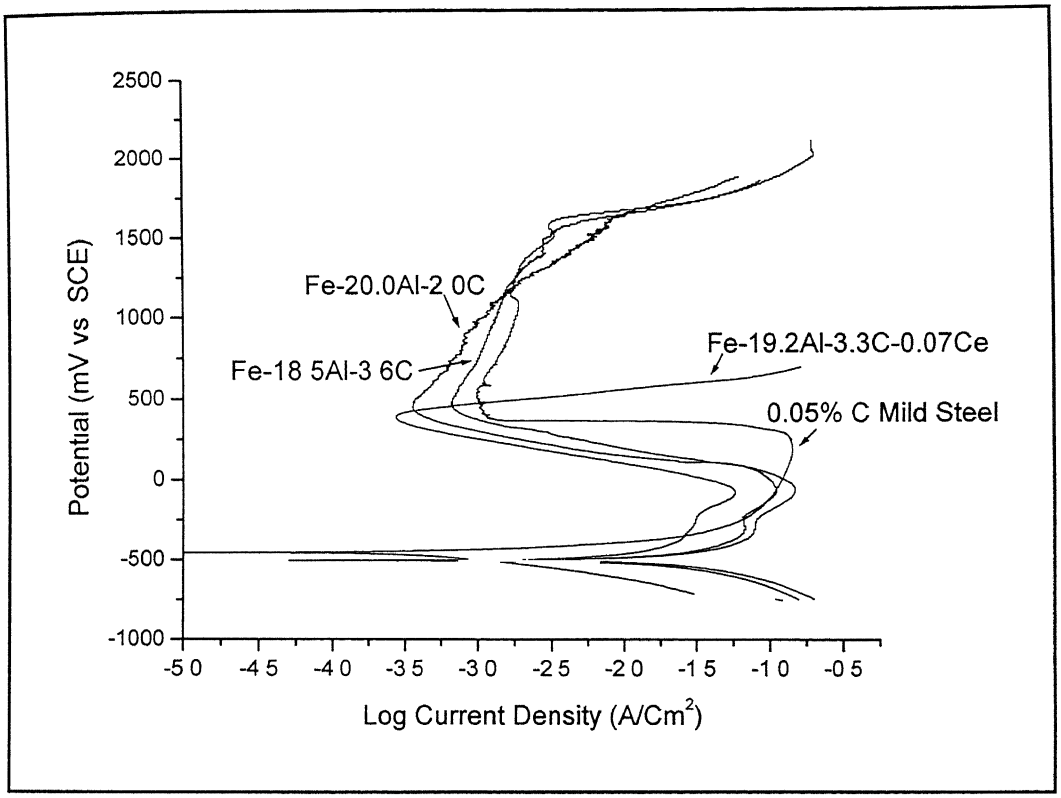

Figure 36 Potentiodynamic polarization behaviour of Fe-20.0Al-2.0C, Fe-18.5Al-3.6C, Fe-19.2Al-3.3C-0.07Ce and mild steel in freely aerated 0.5N H_2SO_4 using a scan rate of 1 mV/sec

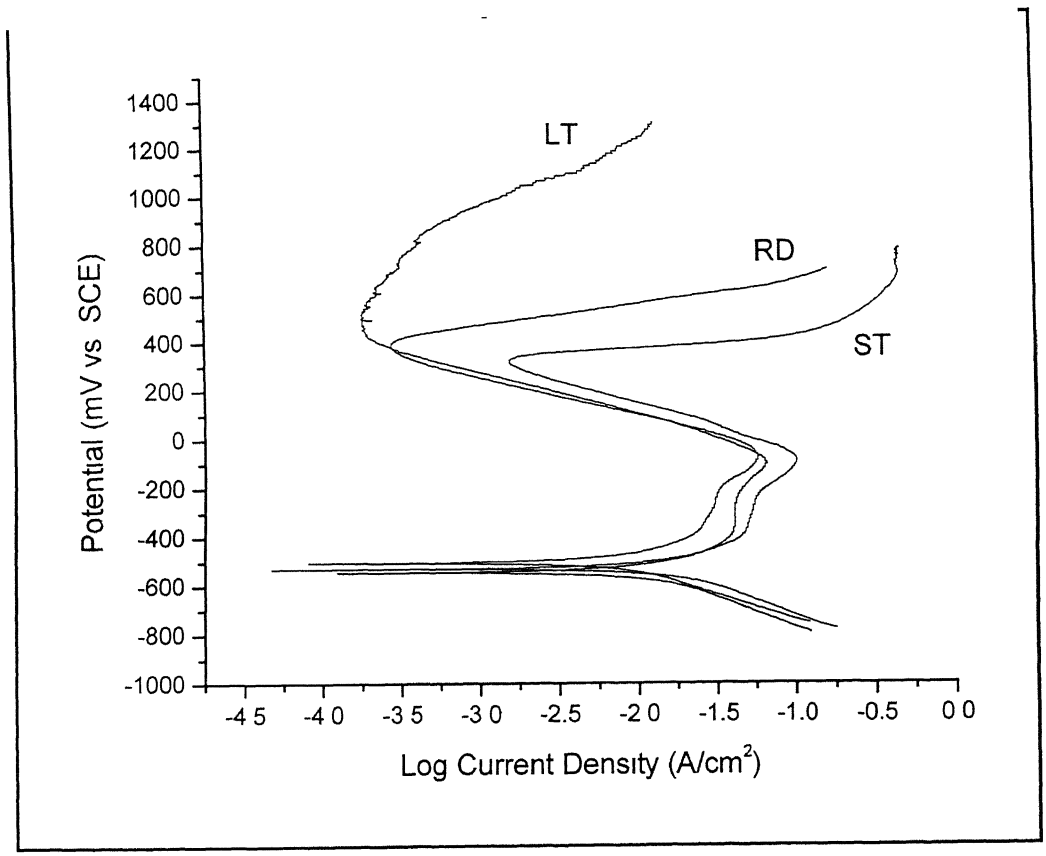

Figure 37. Potentiodynamic polarization curves obtained from the rolling (RD), long transverse (LT) and short transverse (ST) planes of Fe-19.2Al-3.3C-0.07Ce alloy in freely aerated 0.5N H_2SO_4

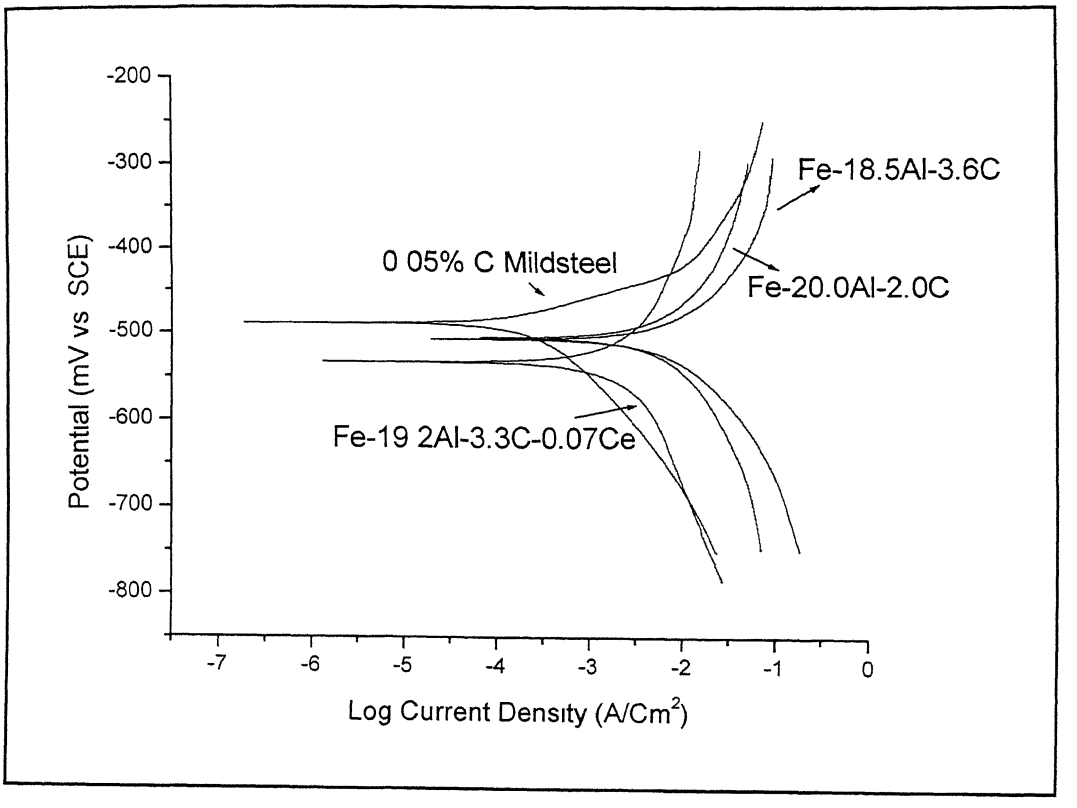

Figure 38 Tafel plots of Fe-20.0Al-2.0C, Fe-18.5Al-3.6C, Fe-19.2Al-3.3C-0.07Ce and mild steel in freely aerated 0.5N H_2SO_4, using a scan rate of 0.166 mV /sec

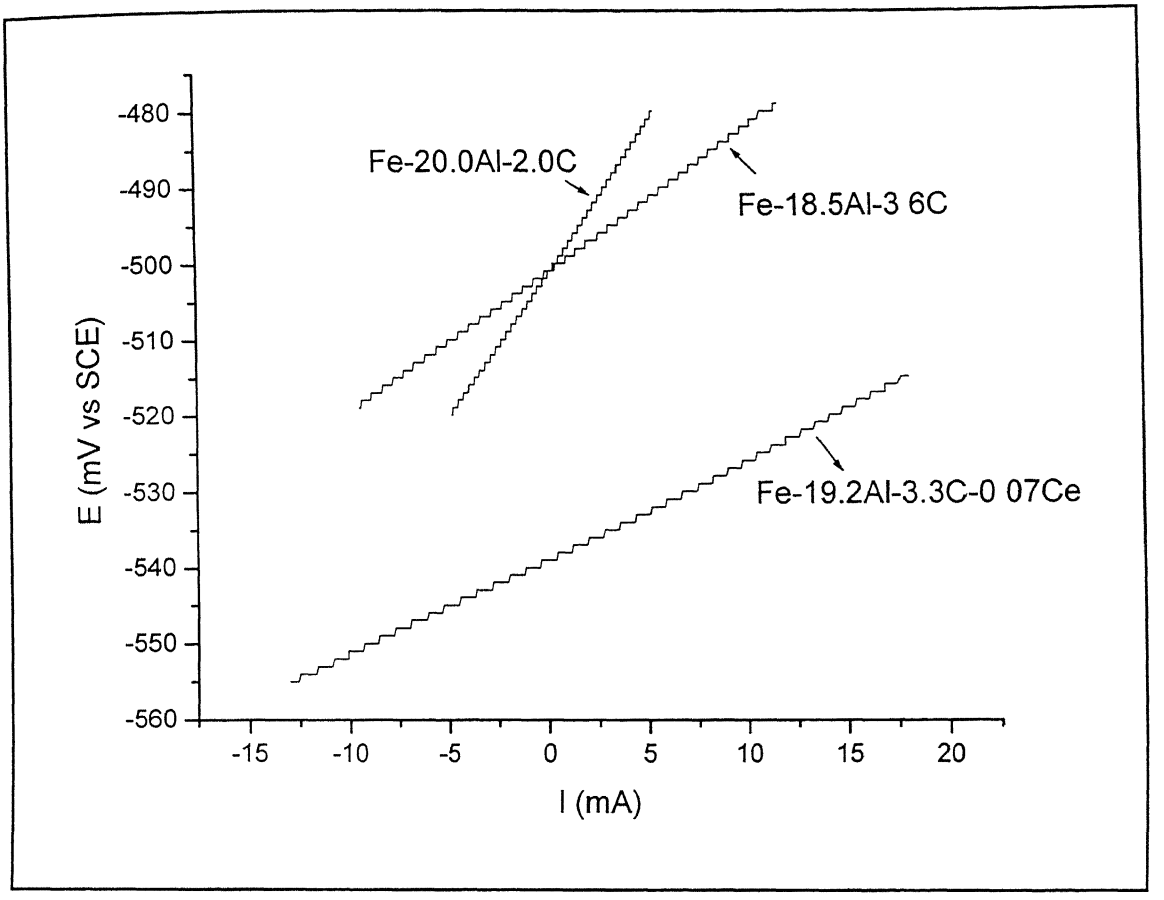

Figure 39 Linear curves obtained from the rolling plane of the as received alloys Fe-19.2Al-3.3C-0.07Ce (ESR137), Fe-20.0Al-2.0C (ESR74) & Fe-18.5Al-3.6C (ESR127) in freely aerated 0.5 N H_2SO_4 solution

Table 16 Passivation parameters obtained from the potentiodynamic polarisation of the ESR127,ESR74 and ESR 137 alloys in freely aerated 0.5N Sulfuric acid

Alloy	Order of experiment	Plane	Composition	ZCP (V)	Epp (V)	Ecp (V)	Eb (V)	Eb-Ecp (V)	icrit A / Cm^2	ipass A / Cm^2
ESR 74	First	RD	Fe-20.0Al-2.0C	-0 515	-0.045	0 418	1 530	1 112	105×10^{-3}	35×10^{-5}
	Duplicated			-0 503	-0 042	0.350	1 560	1 230	74×10^{-3}	36×10^{-5}
ESR 127	First	RD	Fe-18.5Al-3 6C	-0.501	-0.065	0.432	1 570	1.138	149×10^{-3}	67×10^{-5}
	Duplicated			-0 508	-0.054	0.447	1 580	1 133	121×10^{-3}	85×10^{-5}
ESR 137	First	RD	Fe-19.2Al-3.3C-0.07Ce	-0.511	-0.061	0 364	0 394	0 030	53×10^{-3}	27×10^{-5}
	Duplicated			-0 535	-0 055	0.339	0 355	0.016	60×10^{-3}	38×10^{-5}
ESR 137	First	LT	Fe-19 2Al-3 3C-0 07Ce	-0.548	-0.085	0 419	0 526	0 107	66×10^{-3}	17×10^{-5}
	Duplicated			-0.544	-0.063	0.439	0 533	0.094	101×10^{-3}	43×10^{-5}
ESR 137	First	ST	Fe-19.2Al-3 3C-0 07Ce	-0 524	-0 096	0.306	0.331	0.025	102×10^{-3}	162×10^{-5}
	Duplicated			-0.535	-0.017	0.294	0.311	0.029	111×10^{-4}	165×10^{-5}

Table 17 Values of β_a, β_c and i_{corr} obtained from the Tafel Curves of ESR74,ESR137 and ESR127 samples in freely aerated 0.5N sulfuric acid

Alloy	Order of experiment	Plane	Composition	β_a, V / decade	β_c V / decade	icorr A / Cm^2	Corrosion rate (mmpy)
ESR 74	First	RD	Fe-20 0Al-2.0C	-0.194	0.194	$7\ 76 \times 10^{-3}$	179
	Duplicated			-0.296	0.256	8.13×10^{-3}	188
ESR 127	First	RD	Fe-18.5Al-3.6C	-0.129	0.173	9.77×10^{-3}	222
	Duplicated			-0.132	0 136	8.91×10^{-3}	202
ESR 137	First	RD	Fe-19.2Al-3 3C-0 07Ce	-0 206	0.233	2.29×10^{-3}	52
	Duplicated			-0.239	0.258	2.82×10^{-3}	64
ESR 137	First	LT	Fe-19.2Al-3 3C-0 07Ce	-0.055	0.125	1.35×10^{-3}	31
ESR 137	First	ST	Fe-19.2Al-3.3C-0.07Ce	-0.0529	0.050	2.19×10^{-3}	50
Mildsteel	First		Fe-0.05C	-0.16	0.050	0.56×10^{-3}	7

Table 18 Parameters obtained from the linear polarisation curve for the alloys ESR74,ESR127 and ESR137 in freely aerated 0.5N sulfuric acid

Alloy	Order of experiment	Plane	Composition	β_a, V / decade	β_c V / decade	Polarisation resistance Rp	icorr A / Cm^2	Corrosion rate (mmpy)
ESR 74	First	RD	Fe-20.0Al-2.0C	-0.194	0 194	3 868	10.89×10^{-3}	251
	Duplicated			-0 296	0.256	5.004	11.91×10^{-3}	275
ESR 127	First	RD	Fe-18.5Al-3 6C	-0.129	0.173	1 890	16.98×10^{-3}	386
	Duplicated			-0.132	0 136	1 873	15.53×10^{-3}	353
ESR 137	First	RD	Fe-19.2Al-3 3C-0.07Ce	-0.206	0.233	12 730	3.73×10^{-3}	85
ESR 137	First	LT	Fe-19.2Al-3.3C-0 07Ce	-0.055	0.125	2 160	7.47×10^{-3}	170
ESR 137	First	ST	Fe-19.2Al-3.3C-0.07Ce	-0.0529	0.050	2.380	7.00×10^{-3}	160

The effect of Ce addition to Fe_3Al on the surface film nature has been earlier studied by Yangshan *et al.*[15]. They reported that small additions of Ce enhanced the ductility and strength of these alloys at ambient temperature, They also observed, through a X-ray photoelectron spectroscopy (XPS) analysis, that Ce addition increased the proportion of aluminium and chromium oxide but decreased the proportion of iron oxide on the specimen surface. The results of the XPS analysis done by Yangshan *et al* has been reproduced in the Table 19.

Table 19. Results of the XPS analysis conducted by Yangshan *et al* [15] on Cr alloyed iron aluminides with and without Ce addition.

	Proportion of Oxides (%)		
Alloy (wt%)	Al_2O_3	Cr_2O_3	Fe_2O_3
Fe-15.9Al-2.2 Cr	50.22	6.49	43.29
Fe-15.9Al-2.2Cr-0.15Ce	60.35	12.38	24.27

4.2.3. Polarisation behaviour in borate buffered solution

The electrochemical behavior of the as-received ESR74, ESR127 and ESR137 alloy was also studied in the borate buffered solution, of pH=7.6. Borate buffered solutions are normally employed to understand the passivation phenomena in iron based alloys and hence this solution was chosen. Moreover the experiments were conducted immediately after immersion, without the stabilization of free corrosion potential (E_{corr}). The potentiodynamic polarisation potential curves for the alloys have been presented in Figure 40 and the passivation parameters obtained from these curves are tabulated in Table 20. The data for mild steel has been also presented for comparison purposes. All the materials exhibited stable passive behaviour. In the buffered solution, the polarization curves indicated that all the three alloys were passivated readily on immersion. The passive current densities of the alloys were similar but lower in the buffer solution when compared to the acidic solution as expected. The break down potential for all the alloys were around 1000 mV. All the aluminides exhibited a similar behaviour and the effect of Ce could not be revealed using this solution.

Table 20. Passivation parameters obtained from the potentiodynamic polarization of the ESR127, ESR74 and ESR137 alloys in borate buffered solution

Alloy		ZCP	E_{pp}	E_{cp}	E_b	E_b-E_{zcp}	i_{crit}	i_{pass}
		V	V	V			A/cm^2	A/cm^2
ESR74	RD	-0.417	-	-	0.99	1.407	-	0.77×10^{-6}
ESR127	RD	-0.412	-	-	1.020	1.432	-	1×10^{-6}
ESR137	RD	-0.262	-	-	0.995	1.257	-	2.39×10^{-6}
Mild steel	RD	-0.242	-	-	1.010	1.252	-	5.24×10^{-6}

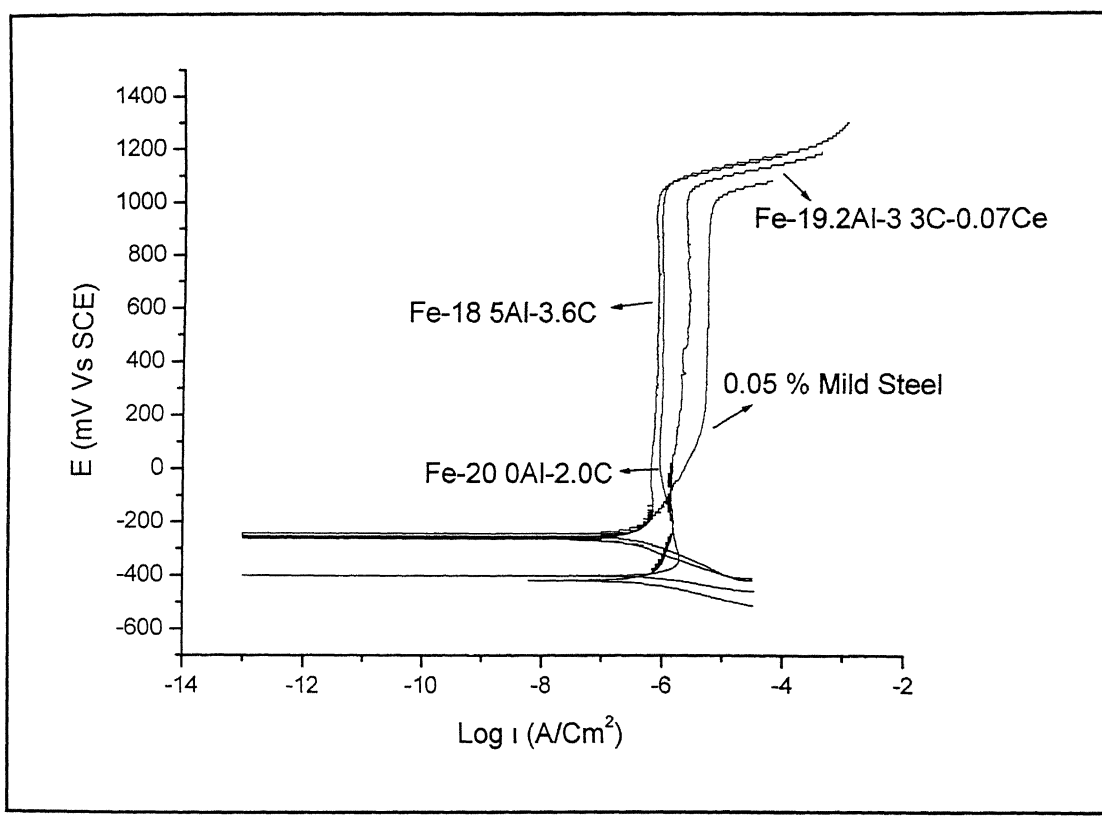

Figure 40 Potentiodynamic polarization behaviour of the rolling plane of as received ESR127, ESR74 and ESR137 alloys in borate buffered solution. The polarisation curve of mild steel has also been presented for comparison purposes.

4.3 Corrosion rates by immersion testing

Long duration immersion testing

Figure 43 indicates the corrosion rate as a function of time plotted for all the samples Fe-18.5Al-3.6C (ESR127), Fe-20.0Al-2.0C (ESR74), and Fe-19.2Al-3.3C-0.07Ce (ESR137) in freely aerated 0.5N H_2SO_4. The experiment was performed for a total duration of 85 hours. The rates of corrosion were high for the first 12 hours for ESR127 and ESR74. Thereafter the corrosion rate decreased and after that it was almost constant in the last few days of the experiment. In contrast, the Ce alloyed aluminide (ESR137) exhibited a lower corrosion rate, that was almost constant throughout the experiment period. In order to understand this behaviour short term immersion studies were also carried out.

Short duration immersion testing

The corrosion rates of the alloys were determined by constant immersion testing method in freely aerated 0.5N H_2SO_4. Two sets of samples of almost equal in size and shape were immersed in the electrolyte for a period of 11 hours and the the weight loss were measured after every 45 minutes. The results thus obtained was utilized to obtain the cumulative corrosion rate upto that point of time. The corrosion rate as a function of time is shown in the Figure 42

In the case of carbon alloyed iron aluminide, the corrosion rate increased initially and after attaining a peak of about 2 hours, decreased and then attained a steady state in an oscillatory mode. The distribution of carbides is expected to enhance selective dissolution. Selective dissolution could imply either selective dissolution of one phase or selective dissolution from selective locations (carbide-matrix interface) in the material. Once a stable equilibrium conditions are attained, the rate of corrosion would then decrease. The decrease in the corrosion rate in the final stages indicates that the carbon alloyed alloy may have attained a equilibrium surface layer in the solution. Another possible reason for the decrease in corrosion rate would be due to the decrease in corrodibility of the solution with time, though this seems unlikely in the present case as

the solution used for testing was relatively strong. The surfaces of the immersed samples were observed in the SEM after 2 hours of exposure in the acidic medium. (Figure 41). It is clear that particle matrix interfaces were selective locations for corrosion. In some cases, these led to the formation of corrosion pits at the interfaces .The carbide particles were not corroded with respect to matrix. This is reasonable as carbon is a relatively noble material and the carbide consists of a significant amount of carbon. The enhanced selective corrosion at the carbide–matrix interfaces could be due the distance effect in galvanic corrosion. The matrix is the anode and carbide the cathode in the galvanic cell. Therefore during the exposure in the solution, the matrix preferentially corrodes specially at the carbide-matrix interfaces. Interestingly, these selective dissolution sites can act as pits with time and these are potential sites for crack initiation by environmental degradation mechanism (stress corrosion cracking, hydrogen embrittlement etc). The corrosion rate was lower in the case of Ce-alloyed iron aluminide. Microstructural studies indicated a finer distribution of carbides. This may not be the reason for the lower corrosion rate observed in the Ce-alloyed aluminide because the carbides in this alloy also accelerated corrosion of the matrix. This is reasonable because the corrosion rate of these alloys are higher than that for mild steel. Therefore, the effect of Ce addition on corrosion must be related to modification in the surface film as discussed earlier.

For comparison purposes the immersion study was also conducted for mildsteel The data obtained from the immersion studies are given in Appendix C.

The effect of Ce on the corrosion of carbon alloyed intermetallics can be summarised as follows: The initial fast rate of corrosion of matrix may lead to Ce enrichment on the surface. Ce enrichment probably induces a more protective film formation on the surface. Therefore, the corrosion rate is lowered and the effect would become more apparent with increasing immersion time. Long term immersion testing of the Ce-alloyed aluminides provide a better idea of the corrosion behaviour than the potentiodynamic polarisation method.

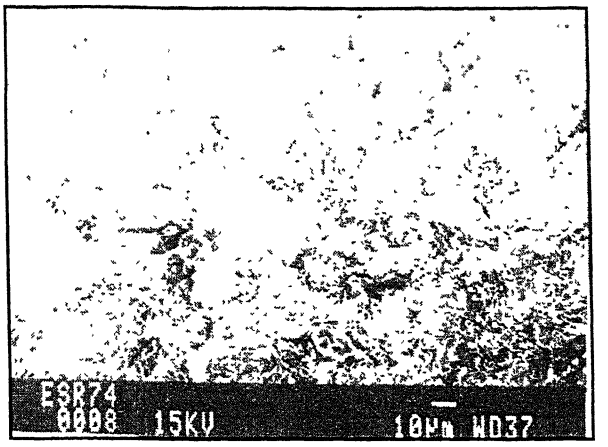

(a)

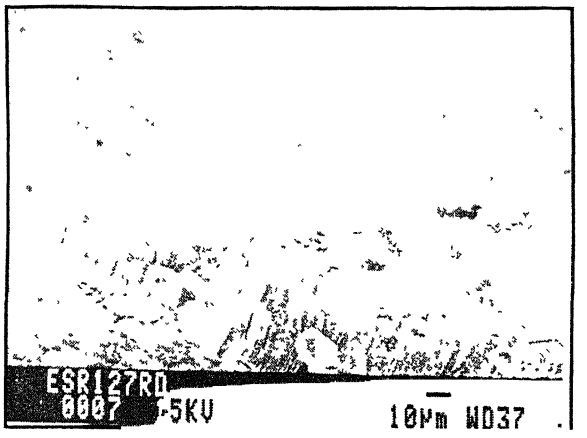

(b)

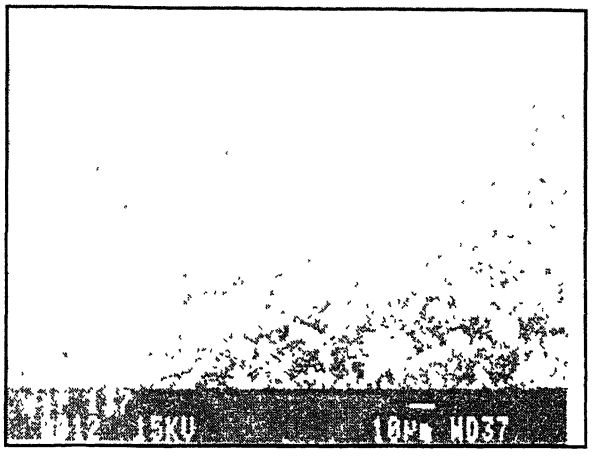

(c)

Figure 41 SEM Micrographs of a) ESR74, b) ESR127 and c) ESR137 after immersion in freely aerated 0.5 N H_2S0_4 solution for 2 hours.

4.4 Comparison of Corrosion rates

The corrosion rates obtained by the immersion testing method (after 2 hour) and the polarization study have been compared in the Table 21. The results tabulated for immersion studies is the highest corrosion value obtained during the period of experiment. It is seen that there is a reasonable agreement in the values obtained from both the experiments. These results indicate that Ce has been instrumental in lowering corrosion, by probably altering the nature of the passive film. It is observed that there is a 75% reduction in the corrosion rates when the intermetallic is alloyed with Ce.

Table 21: The corrosion rate values obtained by Tafel extrapolation method and immersion testing method on the samples ESR127, ESR74 and ESR137 in 0.5N H_2SO_4

	Tafel extrapolation method	Immersion testing method (after 2 h)
Sample	Corrosion rate (mmpy)	Corrosion rate (mmpy)- highest value
ESR74	179	178
ESR127	222	206
ESR137	52	66

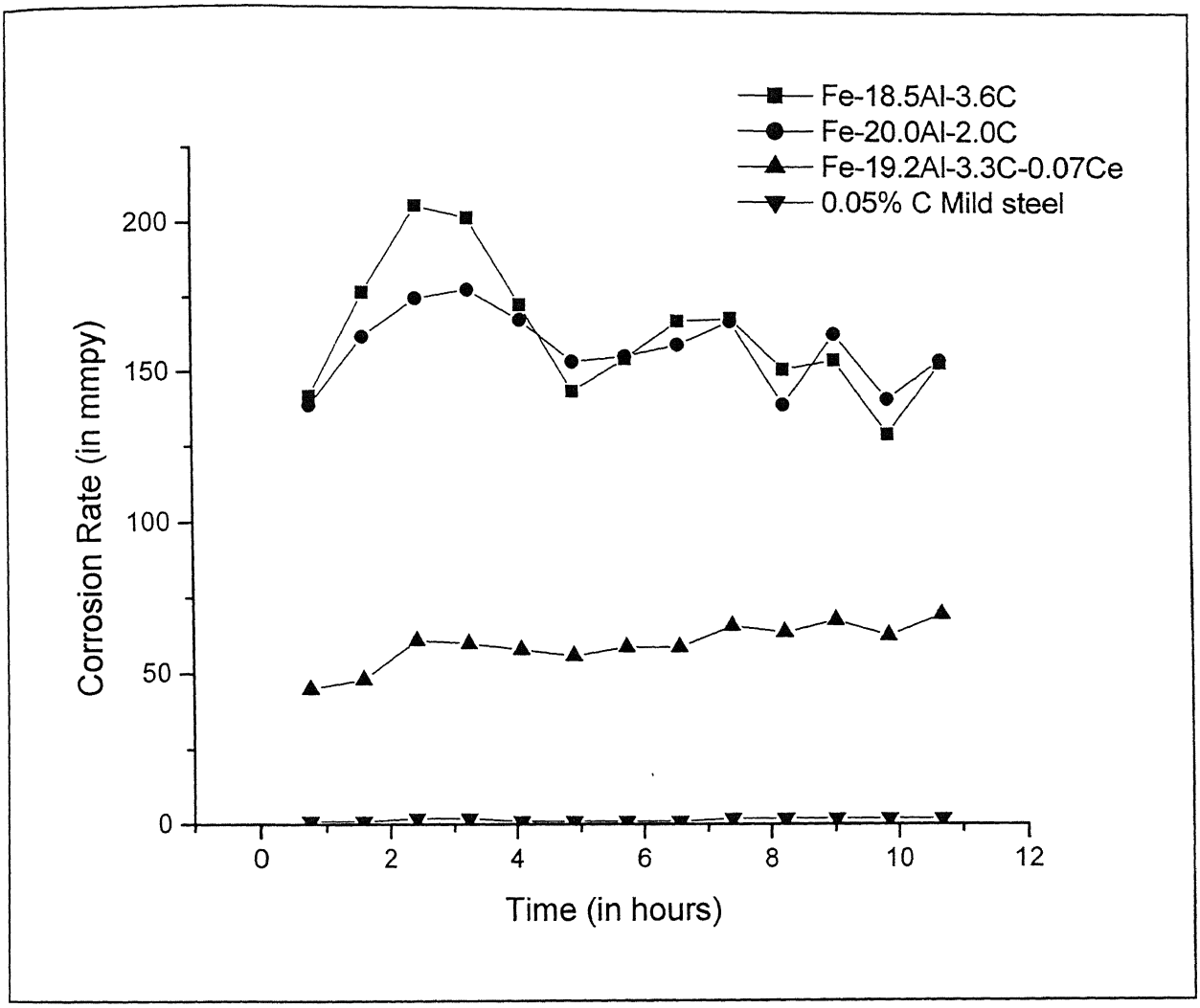

Figure 42 .Corrosion rate as a function of time (upto 11 hours) for the carbon-alloyed iron aluminides and mild steel in freely aerated 0.5N H_2SO_4. The lines connecting the data points are for visual aid only.

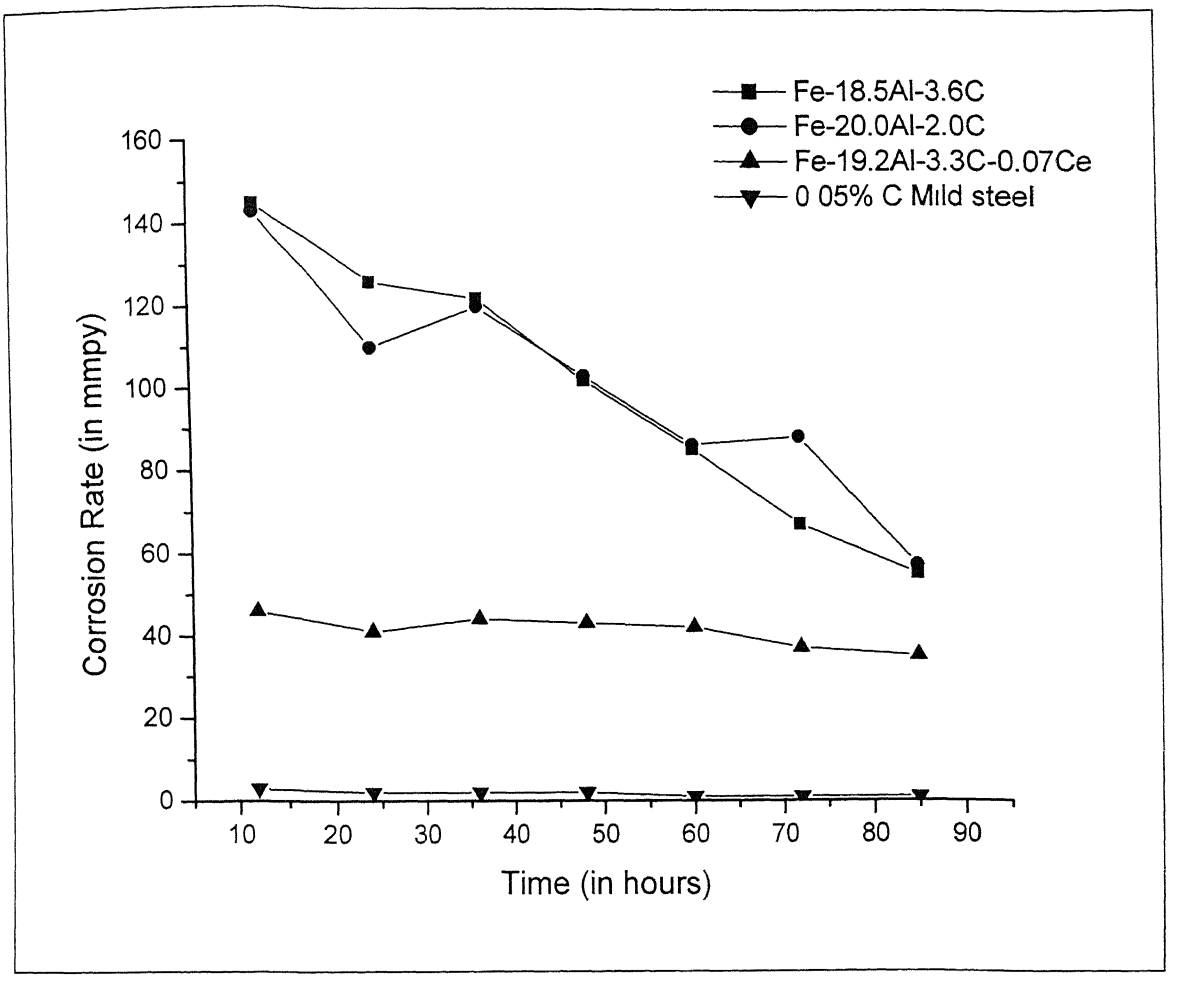

Figure 43 Corrosion rate as a function of time (total duration of 85 hours) for the carbon-alloyed iron aluminides and mild steel in freely aerated 0.5N H_2SO_4.The lines connecting the data points are for visual aid only.

CHAPTER 5

CONCLUSIONS

The following are the conclusions of the present study.

1. Microstructural observations indicated that the alloys Fe-18.5Al-3.6C (ESR127) Fe-20.0Al-2.0C (ESR74) and Fe-19.2Al-3.3C-0.07Ce (ESR137) exhibited a typical two-phase structure consisting of carbides dispersed in a Fe_3Al iron aluminide matrix. The matrix contained recrystallised grains. Two different types of morphology of the second phase carbide particles were observed in the alloys Fe-18.5Al-3.6C (ESR127) and Fe-20.0Al-2.0C (ESR74). Larger spherical and smaller nodular shaped precipitates. Larger bulky carbides were equally distributed throughout the matrix with many smaller precipitates interspersed in between. However, in case of the Ce added alloy Fe-19.2Al-3.3C-0.07Ce (ESR137), the microstructure was different when compared to that of ESR127 and ESR74 alloys. The carbide grain sizes were much finer and they were found uniformly distributed throughout the matrix. Therefore, the addition of Ce to the iron aluminides affected the morphology and size of the carbides.

2. Stereological analysis was carried out on the rolling plane of the alloys. Examination of these microstructure using stereological methods confirmed that the alloys possessing higher carbon content, i.e. Fe-18.5Al-3.6C (ESR127) and Fe-19.2Al-3.3C-0.07Ce (ESR137), possessed a higher volume fraction of carbide and higher exploded surface area per unit volume, when compared to the lower carbon alloy Fe-20.0Al-2.0C (ESR74). Second phase carbide phases in the samples ESR127 and ESR137 were more contiguous and proximate than the carbides in ESR74. This was due to the higher amount of carbon in ESR127 and ESR137. Moreover, in case of the Ce added sample, ESR137, the role played by Ce in finer and uniform distribution of carbides

can also be the reason for the observed higher contiguity in the Fe-19.2Al-3.3C-0.07Ce (ESR137) sample.

3. The structure of the matrix and carbides was understood by X-ray diffraction. patterns confirmed that the presence of carbon leads to the formation of Fe_3AlC precipitates in the matrix. The Ce-alloyed intermetallics did not exhibit any additional diffraction peaks apart from the peaks obtained in the case of the base intermetallics. Therefore, it was concluded that Ce-additions essentially enter into solid solution in the Fe_3Al matrix or in the interfacial region between carbide and the matrix.

4. The microhardness of the bulky carbides and the matrix were measured for the alloys Fe-20.0Al-2.0C and Fe-18.5Al-3.6C. It was observed that the carbides and matrix of the sample Fe-20.0Al-2.0C exhibited higher hardness. The increase in hardness of the carbides could be probably due to the higher aluminium content of the alloy which forms a hard $Fe_{4-y}Al_yC_x$ phase. The hardness of the matrix in all the alloys was comparable. Microhardness measurements of the finer carbides in the Ce added alloy Fe-19.2Al-3.3C-0.07Ce was not possible because proper indentations could not be made due to the small size of these carbides.

5. The potentiodynamic polarization behavior of alloys ESR74, ESR127 and ESR137 alloy was studied in freely-aerated 0.5N H_2SO_4 (pH of 0.74). All the three alloys exhibited active-passive behaviour. The passivation parameters were generally comparable between the two alloys ESR74 and ESR127. This is reasonable because the carbon contents are not significantly different and, moreover, the carbide distribution in these alloys was similar. The lower carbon content alloy Fe-20.0Al-2.0C, exhibited a comparatively lower critical current density. The Ce-alloyed iron aluminide Fe-19.2Al-3.3C-0.07Ce (ESR137) exhibited a lower passive range when compared to the other carbon alloyed iron aluminides.

6. The other two directions, i.e the short transverse section (ST) and longitudinal section (LT) of the Fe-19.2Al-3.3C-0.07Ce alloy, were also subjected to potentiodynamic experiments in freely aerated 0.5N H_2SO_4 (pH of 0.74). The lower values of i_{pass} for the rolling plane and the long transverse plane indicate that the addition of Ce influences the nature of the passive film. An interesting result was the relatively better passivation properties (i.e. higher E_b and the passivation range) obtained in the LT section for the Ce alloyed aluminide.

7. The electrochemical behavior of the as-received ESR74, ESR127 and ESR137 alloy was also studied in a borate buffered solution (1.5N H_3BO_3 + 0.1N $Na_2B_4O_7.10H_2O$ + 0.01N KNO_3) of pH 7.6. All the alloys exhibited stable passive behaviour and the alloys passivated readily on immersion. The passive current densities of the alloys were similar but lower in the buffered solution when compared to the acidic solution. The break down potential for all the alloys were around 1000 mV vs SCE. All the aluminides exhibited similar behaviour and the effect of Ce could not be revealed using this solution.

8. The ideal scan rate for the potentiodynamic polarization experiments for all the alloys was identified as 1mV/sec. Similarly, experimental observations indicated that the round bottom cell is ideally suited when compared to the flat cell for performing the electrochemical experiments for these alloys. Hydrogen evolution sometimes blocked the fine capillary used for potential measurement.

9. Corrosion kinetics was studied by weight loss method. In the long term experiment of 85 hours, the rates of corrosion were high for the first 12 hours for ESR127 and ESR74. Thereafter, the corrosion rate decreased and it was almost constant in the last few days of the experiment. In contrast, the Ce alloyed aluminide (ESR137) exhibited a lower corrosion rate that was almost constant throughout the experiment period. In the short term experiment of 11 hours, the corrosion rates for the alloys ESR127 and ESR74 increased initially

and after attaining a peak of about 2 hours decreased. The corrosion rate attained a steady state in an oscillatory mode.

10. The presence of carbide leads to local galvanic corrosion. The enhanced selective corrosion at the carbide–matrix interfaces could be due to the distance effect in galvanic corrosion. The uniform distribution of carbides is expected to enhance selective dissolution. The decrease in the corrosion rate in the final stages indicates that the carbon-alloyed alloy may have attained an equilibrium surface layer in the solution. The corrosion rate was lower in the case of Ce alloyed iron aluminide.

11. The addition of Ce resulted in a finer distribution of the carbides (i.e. smaller sizes) through the alteration of the microstructure. As the corrosion rate for Ce-alloyed material was lower, it appears that Ce addition modified the surface film. The effect of Ce on the corrosion of carbon alloyed intermetallics can be summarised as follows: The initial fast rate of corrosion of matrix leads to Ce enrichment on the surface. Ce enrichment induces a more protective film formation on the surface. Therefore, the corrosion rate is lowered. The effect becomes more apparent with increasing immersion time.

SUGGESTIONS FOR FUTURE WORK

Some additional work, which are needed to be undertaken in order to resolve certain issues raised in this thesis, are listed below.

1. Stereological analysis can also be performed for the short and long transverse sections of the three alloys ESR74,ESR127 and ESR137.
2. The electrochemical polarization behaviour of the alloy can also be performed using different electrolytes other than H_2SO_4, to understand surface nature.
3. The high temperature oxidation behaviour of the Ce-alloyed intermetallics should be studied to validate its potential as candidate high temperature material.
4. The microstructure of both the Ce alloyed and non-Ce alloyed samples can be varied using thermo mechanical treatments, and the effect of change in microstructure on the mechanical and electrochemical behaviour can be studied.
5. High temperature hydrogen attack in the Ce-alloyed iron aluminides can be studied to understand the utility of these alloys at a high temperature in atmosphere containing hydrogen.
6. To understand the role of Ce in the protective film formation, electrochemical impedance spectroscopy can be performed by long term testing of the Ce alloyed sample.

REFERENCE

1. N. S. Stoloff, "Ordered alloys – physical metallurgy and structural applications", *International Metal Review*, **29**, 1984, pp 123-135.
2. T. Yamamoto. "The development of Sendust and other ferromagnetic alloys". Chiba: *Committee of Academic achievements*, 1980, pp 1-6.
3. C. T. Liu, J.O. Stiegler and F.H. Froes, "Ordered Intermetallics", *Metals Handbook, 10th ed.,* ASM, Metals Park, USA, **2**, 1990, pp. 913-942
4. G. Sauthoff, *Z. Metallkd*, **80**, 1989, pp 337-344.
5. A. J. Bradley and A.H. Jay, *J of Iron and Steel Institute,* **125**, 1932, p 339
6. C Sykis and J. Bampfylde, *J of Iron and Steel Institute*, **130**, 1934, p 389
7. C. T. Liu and K.S. Kumar, "Ordered Intermetallic Alloys, Part 1, Nickel and Iron aluminides", *JOM*, **45**, 1993, pp. 38-44
8. C. T. Liu, C.G. McKamey and E. H. Lee, "An environmental effect as the major cause room temperature embrittlement in FeAl", *Scripta Metall.,* **23**, 1996, pp. 875-880
9. C. G. McKamey and C.T.Liu. "Chromium addition and environmental embrittlement Fe_3Al", *Scripta Metall. Mater.* **24**, 1992, pp. 119-2122.
10. Zhonghua, S. Yangshan, L. Guijun, and G. Jun, "Ductility improvement of Fe_3Al based alloys with surface coating", *Scripta Mater.*, **34**, 1996, pp 1071-1075.
11. R. Balasubramaniam, "On the role of chromium in minimizing room temperature hydrogen embrittlement in iron aluminides", *Scripta Mater.*, **34**, 1996, pp.127-133.
12. R. Balasubramaniam, "Alloy development to minimize room temperature hydrogen embrittlement in iron aluminides", *J. Alloys and Comp.*, 1994, pp. 253-254.
13. R G. Baligidad, U. Prakash, A. Radhakrishna and V. Ramakrishna Rao, "Effect of carbides on embrittlement of Fe_3Al based intermetallic alloys", *Scripta Mater.*,**36**, 1997, pp. 667-671
14. R. G. Baligidad, U. Prakash, A. Radhakrishna and V. Ramakrishna Rao, "Effect of carbon contents on high temperature tensile properties of Fe_3Al based intermetallic alloy", *Scripta Mater.,* **36**, 1997, pp.105-109.
15. S. Yangshan, Y. S. Zhengjun, Z. Zhonghua and H. Haibo, "Mechanical Properties of Fe_3Al based Alloys with Ce addition", *Acta Metall. Mater.*, **33**, 1995, pp. 811 – 812

16. M. Palm and G. Inden "Experimental determination of phase equilibria in the Fe-Al-C system, *Intermetallics,* **3**, 1995, pp. 443-454.

17. V. Raghavan, Phase diagram of ternary iron alloys, Part 1, Indian Institute of Metals, 1991, pp. 89-97.

18. R.G. Baligidad, U. Prakash and A. Radhakrishna, "Effect of processing on mechanical properties of an Fe–8.5 wt.% Al–1.1 wt.% C alloy" *Mater. Sci. Engg. A*, **255**, 1998, pp 162-168.

19. V.Shankar Rao, R. G.Baligidad and V. S.Raja,"Effect of carbon on corrosion behaviour of Fe_3Al intermetallics in 0.5N sulphuric acid,"*Corr.Sci*,**44**, 2002 pp.521-533.

20. C. Sykes and J. Bampyfylde, "The physical properties of iron aluminium alloys", *J. Iron Steel Inst*, **130**, 1932, pp. 389-394

21. C. T. Liu, C. G. McKamey and E. H. Lee, "Environmental effects on room temperature ductility and fracture mode in Fe_3Al alloys", *Scripta Metall. Mater*, **24**, 1990, pp. 385-390

22. Y. F. Zhu, C. T. Liu and C. H. Chen, "Direct evidence of hydrogen generation from the reaction of water with FeAl", *Scripta Mater.*, **35**, 1996, 1435-1439.

23. A. Agarwal, M. J. Akhtar and R. Balasubramaniam, "Effect of alloying on aqueous corrosion and mechanical behaviour of iron aluminide Fe_3Al", *J Mat. Sci.*, **31**, 1996, pp. 5207-5213

24. V.K. Sikka, "Processing and applications of iron aluminides", in *Processing, Properties and Applications of Iron aluminides*, eds J.H. Schneibel and M.A. Crimp, TMS, Warrendable, USA, 1994, pp 3-18.

25. A. Agarwal and R. Balasubramaniam, "Role of surface passive films on the hydrogen embrittlement of iron aluminides".*Bull. Mater.Sci.*, **19**, 1996, pp 91-102

26. E. Underwood, Quantitative Stereology, Addison-Wesley Publishing Company, New York, USA,1970,pp.25-103

27. C G McKamey, J.A. Horton and C. T. Liu, "Effect of chromium on room temperature ductility and fracture mode in Fe_3Al", *Scripta Metall.*, **22**, 1988, pp 1679-1681.

28. S. Mukherjee and R. Balasubramaniam, "Deciphering the potentiodynamic polarisation curves of iron aluminides Fe_3Al and Fe_3Al+Cr ", *Bull. Mater.Sci.*, **19**, 1996, pp 831-835

29. C. G. McKamey and D.H. Pierce, "Effect of recrystallisation on room temperature tensile properties of Fe_3Al based alloy", *Scripta Metall. Mater.*, **28**, 1993, pp 1173-1176.

30. D. Lin, A. Shan and D. Li, "Superplasticity in Fe_3Al-Ti alloy with large grains",*Scripta Metall Mater.*, **31**, 1994, pp 1455-1460.

31. A. Agarwal, R. Balasubramaniam and S. Bhargava, "Effect of thermomechanical treatment on the room temperature mechanical behaviour of iron aluminide", *Met.Mater Trans.*, **27A**, 1994, pp 2985-2994

32. A. Agarwal and R. Balasubramaniam, "Fracture characteristics of alloyed iron aluminides", *Pract. Metallogr.*, **33**, 1996, pp 453-466.

33. M.A. Crimp and K.M. Vedula, "Effect of boron on the tensile properties of B2 FeAl", *Mat.Sci. Eng.*,**78**, 1986, pp 1993-1999.

34. C. T. Liu and E P. George. "Environmental embrittlement in boron free and boron doped FeAl alloys", *Scripta Metall. Mater.*, **24**, 1990 pp 1285-1290.

35. P. Banerjee and R. Balasubramaniam, "Mechanical behaviour of chromium and titanium alloyed iron aluminides with michmetal addition", *Scripta Materialia*, **38**, 1998, pp 1143-1147.

36. P. Banerjee, "Hydrogen behaviour in Chromium and Titanium Alloyed Iron Aluminides", M.Tech Thesis, I.I.T, Kanpur, 1997.

37. X. Yu and Y. Sun, "The oxidation improvement of Fe_3Al based alloy with Ce addition at temperature above 1000°C ", *Materials Sci and Engg.***363**, 2003, pp 30-39

38. N. Babu, "Room Temperature Aqueous Corrosion and High Temperature Oxidation Behaviour of Iron Aluminides", M.Tech thesis, I.I.T Kanpur, 1998.

39. E. R. Weibel, Stereological Methods, v. 2, Academic Press, 1980, pp. 1-18

40. R. G. Baligidad, U. Prakash and A. Radhakrishna, *Mater. Sci. Engg. A*, **249**, 1998, pp 97-102

41. R. G. Baligidad, U. Prakash, V. R. Rao and P. K. Rao, *ISIJ International*, **36**, n. 12, 1996, pp. 1453-1458.

42. R. G. Baligidad, U. Prakash and A. Radhakrishna, "Thermal stability and elevated temperature mechanical properties of electroslag remelted" Fe-16wt.%Al-(0.14-0.5)wt.%C intermetallic alloys *Mater. Sci. Engg. A*, **230**, 1996, pp. 188-193

43. M. Sen, R. Balasubramaniam and A.V. Ramesh Kumar, "Corrosion of carbon alloyed iron aluminides, "*Bull. Mater. Sci.*, **23**, 2000, pp. 399-403.

44. R. G. Baligidad, U. Prakash and A. Radhakrishna, "On elevated temperature stability of high carbon Fe-Al alloys" *Mater. Sci. Engg. A*, **265**, 1999, pp. 301-305

45. R. G. Baligidad, and A. Radhakrishna, *Mater. Sci. Engg. A*, **281**, 1999, pp. 97-102

46. K R. Trethwey and J. Chamberlain, *Corrosion for Students of Science and Engineering*, John Wiley & Sons, Inc., New York, 1988

47. D. A. Jones, *Principles and Prevention of Corrosion*, Maxwell Macmillan International Editions, NY, 1992, pp. 117-524.

48. M. G. Fontana and N.D. Greene, *Corrosion Engineering*, McGraw-Hill International Book Company, 2nd edition, 1983. pp

49. Metals Test Methods and Analytical Procedures, *"Annual Book of ASTM Standard"*, ASTM, Philadelphia, USA, 03.02,Section 3,1999.p.58.

50. R. G .Baligidad, U. Prakash, V. R Rao, P.K. Rao and N.B. Ballal, "Electroslag remelting of Fe-28at% Al intermetallic alloy", *Iron and Steel making*, **21**, 1994, pp 324-331

51. P. Kofstad, "High Temperature Corrosion, *Elsevier Applied Science*, New York, USA, 1998,pp.404-405.

52. T. Laha, A. Tewari, R. Balasubramaniam, M N Mungole, R G Baligidad "Microstructural Evolution in Iron Aluminide Fe-28Al-2C after High Temperature Hydrogen Treatment"2004 *Met.Mater.Trans.A*, to be published.

53. D A R Kay, W.K and A McLean, 1975, "Rare Earth-oxygen –sulfur reactions in molten steel,"in Sulfide Inclusions in Steel, Proceedings of an International Symposium, J.J.deBarbadillo and E Snape (Eds.),American Society for Metals, Metals Park, USA, pp.23-43

54. W. B. Pearson, "Handbook of lattice spacings and structures of metals" Pergamon 1959 pp 42-51.

55. N. D. Tomashov and G.P. Chernova, *"Passivity and Protection of Metals Against Corrosion"*, Plenum Press, USA, (1967),pp.14-28.

APPENDIX A

Table A-1 Volume fraction Studies of bulky carbides

	ESR 127RD		Grid 10x10		ESR 74RD		Grid 10X10		ESR 137RD			Grid 10x10
FOV's	obsvd points	x values	(x - x)	Square (x-x)	Obsvd points	x values	(x - x)	Square(x-x)	obsvd points	x values	(x - x)	Square(x-x)
1	32	0 32	-0 01	0 00	17	0.17	-0 03	0 00	30	0 3	-0 05	0 00
2	33	0 33	0 00	0 00	11	0.11	-0 09	0 01	46.5	0.465	0 12	0 01
3	29	0 29	-0 04	0 00	21 5	0 215	0 01	0 00	49 5	0.495	0.15	0 02
4	29	0 29	-0 04	0 00	20 5	0 205	0 00	0 00	34 5	0 345	0.00	0 00
5	34 5	0 345	0 01	0 00	22	0.22	0 02	0 00	40	0 4	0.05	0 00
6	32 5	0 325	-0 01	0 00	25 5	0.255	0 05	0.00	31 5	0 315	-0 03	0 00
7	30 5	0 305	-0 03	0 00	23	0.23	0 03	0 00	27	0 27	-0 08	0.01
8	35	0 35	0 02	0 00	31.5	0 315	0 11	0 01	24	0.24	-0 11	0 01
9	40 5	0 405	0 07	0 01	25	0 25	0 05	0.00	33 5	0 335	-0 01	0 00
10	39 5	0 395	0 06	0 00	21	0 21	0 01	0.00	36 5	0 365	0.02	0 00
11	33 5	0.335	0 00	0 00	25 5	0 255	0 05	0.00	26 5	0 265	-0 08	0 01
12	27	0 27	-0 06	0 00	14	0 14	-0 06	0 00	35	0 35	0 00	0 00
13	22	0 22	-0 11	0 01	15 5	0 155	-0 05	0.00	37	0 37	0 02	0 00
14	29	0 29	-0 04	0 00	11	0 11	-0 09	0 01	33 5	0 335	-0 01	0 00
15	34	0 34	0 01	0 00	19	0 19	-0 01	0 00	28	0 28	-0 07	0 00
16	30	0 3	-0 03	0 00	19 5	0 195	-0 01	0 00	35	0.35	0 00	0 00
17	34	0 34	0 01	0 00	13 5	0 135	-0 07	0 00	30 5	0 305	-0 04	0 00
18	29	0 29	-0 04	0 00	20	0 2	0 00	0 00	35 5	0 355	0 01	0 00
19	36 5	0 365	0 03	0 00	13 5	0 135	-0 07	0 00	30	0 3	-0 05	0 00
20	33 5	0 335	0 00	0 00	17 5	0 175	-0 03	0 00	47 5	0 475	0 13	0 02
21	41	0 41	0 08	0 01	20 5	0 205	0 00	0 00	42	0 42	0 07	0 01
22	29 5	0 295	-0 04	0 00	19	0.19	-0.01	0 00	34 5	0 345	0 00	0 00
23	41	0 41	0 08	0 01	25 5	0 255	0 05	0 00	42	0 42	0 07	0 01
24	45	0 45	0 12	0 01	23	0 23	0 03	0 00	37	0 37	0 02	0 00
25	38	0 38	0 05	0 00	19 5	0 195	-0.01	0 00	29	0 29	-0 06	0 00
26	39 5	0 395	0 06	0 00	22	0 22	0 02	0 00	29 5	0 295	-0 05	0 00
27	37	0 37	0 04	0 00	17	0 17	-0 03	0 00	37 5	0 375	0.03	0 00
28	27 5	0 275	-0 06	0 00	26 5	0 265	0 06	0 00	29	0 29	-0 06	0 00
29	26 5	0 265	-0 07	0 00	25	0 25	0 05	0.00	33	0 33	-0 02	0 00
30	23	0 23	-0 10	0 01	23	0 23	0 03	0 00	34 5	0 345	0 00	0 00
Sum	33 07	9 92		0 0896867		6 08		0 06813667		10 395		0 1135075
Mean		**0.33**				**0.20**				**0.35**		
Variance Vx				0 0030926				0 00234954				0 0039141
Std devn = Sqrt of Variance				0 0556115				0 04847206				0 0625624
no of FOV's (n)				30				30				30
Square root of n				5 4772256				5 47722558				5 4772256
Std error of mean =Stddevn/Sqr				0 0101532				0.00884975				0 0114223
95% confidence interval				**0.0406129**				**0.03539898**				**0.0456891**

Table A-2 **Grain size measurement**

	ESR	127RD	8 lines each 2300 m		ESR	74RD	8 lines each 2300 m	
FOV's	obsvd	x values	(x - x)	Sq (x-x)	Obsvd	x values	(x - x)	Square(x-x)
	points				points			
1	33	557 58	-17 3	300 4	38	484.2	3.73	13.91
2	31	593 55	18 6	347 5	41	448.8	-31.70	1004 95
3	48	383.33	-191 6	36700.9	41	448 8	-31 70	1004 95
4	47	391 49	-183 4	33642.5	38	484.2	3 73	13.91
5	43	427 91	-147.0	21609.4	30	613.3	132.85	17649.64
6	31	593 55	18 6	347.5	48	383.3	-97.15	9437.74
7	28	657 14	82.2	6762.5	28	657.1	176 66	31209 28
8	28	657 14	82 2	6762.5				
9	31	593 55	18 6	347.5	43	427 9	-52.57	2764.07
10	30	613 33	38 4	1476 5	48	383.3	-97.15	9437.74
11	35	525 71	-49 2	2420 0	41	448.8	-31 70	1004.95
12	46	400.00	-174 9	30592 9	47	391.5	-88.99	7919.58
13	42	438 10	-136 8	18717 8	38	484.2	3.73	13 91
14	51	360 78	-214 1	45849 0	40	460 0	-20.48	419 49
15	47	391 49	-183 4	33642 5	34	541.2	60.70	3683 89
16	34	541 18	-33 7	1137.8	36	511.1	30.63	938 18
17	36	511 11	-63 8	4070.1	41	448.8	-31.70	1004 95
18	34	541 18	-33 7	1137 8	40	460 0	-20 48	419.49
19	27	681 48	106 6	11357.9	41	448.8	-31 70	1004 95
20	25	736 00	161 1	25950.6	39	471 8	-8.69	75.46
21	31	593 55	18 6	347 5				
22	27	681 48	106 6	11357.9	40	460.0	-20 48	419.49
23	29	634 48	59 6	3549.1	32	575 0	94.52	8933 77
24	33	557 58	-17 3	300 4	30	613 3	132.85	17649.64
25	30	613 33	38.4	1476.5	36	511.1	30 63	938.18
26	24	766 67	191.8	36771.3				
27	26	707 69	132.8	17631 6	39	471 8	8 69	75 46
28	27	681 48	106 6	11357 9	49	375.5	-104.97	11018 95
29	26	707 69	132.8	17631 6	39	471.8	-8.69	75.46
30	26	707 69	132.8	17631 6	37	497.3	16 82	282 77
Sum		17247 25		401228 87		12973.00		128414.72
Mean		**574.91**				**480.48**		
Variance Vx				13835 48				4939 03
Std devn = Sqrt of Variance				117 62				70.28
no of FOV's (n)				30.00				27 00
Square root of n				5.48				5 20
Std error of the mean =Stddevn/Sqrtn				21 48				13 53
95% confidence interval				**85.90**				**54.10**

Mean grain size of 127 RD	574.91 microns
Mean grain size of 74 RD	480.48 microns

Table A-3 **Exploded Surface area of Carbides**

	ESR	127RD	Grid	H 2000	V 46		ESR	137RD	Grid	H 2000	V 46		ESR	74RD	Grid	H 2000	V 46
FOV's	obsvd points	P_L	Sv	(x - x)	Square (x-x)	FOV's	obsvd points	P_L	Sv	(x - x)	Square (x-x)	FOV's	obsvd points	P_L	Sv	(x - x)	Square (x-x)
1	265	0 1286	0 2573	0 01	0 0001	1	238	0 115534	0 231068	-0 01	0 0000	1	261	0 126699	0.253398	0 02	0 0005
2	265	0 1286	0 2573	0 01	0 0001	2	266	0 129126	0 258252	0 02	0 0004	2	211	0 102427	0 204854	-0 03	0 0006
3	276	0 134	0.268	0 02	0 0004	3	265	0 128641	0 257282	0 02	0 0004	3	274	0 13301	0.266019	0 04	0 0013
4	275	0 1335	0 267	0 02	0 0004	4	251	0 121845	0 243689	0 01	0 0000	4	231	0 112136	0 224272	-0 01	0 0000
5	240	0 1165	0 233	-0 01	0 0002	5	292	0 141748	0 283495	0 05	0 0021	5	308	0 149515	0 299029	0 07	0 0048
6	263	0 1277	0 2553	0 01	0 0001	6	242	0 117476	0 234951	0 00	0 0000	6	193	0 093689	0.187379	-0 04	0 0018
7	289	0 1403	0 2806	0 03	0 0011	7	219	0 106311	0 212621	-0 02	0 0006	7	375	0 182039	0 364078	0 13	0 0180
8	266	0 1291	0 2583	0 01	0 0001	8	228	0 11068	0 221359	-0 02	0 0003	8	221	0 107282	0 214563	-0 02	0 0002
9	265	0 1286	0 2573	0 01	0 0001	9	230	0 11165	0 223301	-0 01	0 0002	9	191	0 092718	0 185437	-0 04	0 0020
10	229	0 1112	0 2223	-0 03	0 0006	10	0	0	0	0 00	0 0000	10	179	0 086893	0 173786	0 00	0 0000
11	276	0 134	0 268	0 02	0 0004	11	263	0 12767	0 25534	0 02	0 0003	11	253	0 122816	0 245631	0 02	0 0002
12	236	0 1146	0 2291	-0 02	0.0003	12	281	0 136408	0 272816	0 04	0 0012	12	247	0 119903	0.239806	0 01	0 0001
13	0	0	0	0 00	0 0000	13	265	0 128641	0 257282	0 00	0 0000	13	195	0.09466	0.18932	0 00	0 0000
14	231	0 1121	0 2243	-0 02	0 0005	14	235	0 114078	0 228155	-0 01	0 0001	14	183	0 088835	0 17767	-0 05	0 0027
15	260	0 1262	0 2524	0 01	0 0000	15	213	0.103398	0 206796	-0 03	0 0009	15	224	0.108738	0 217476	-0 01	0 0002
16	250	0 1214	0 2427	0 00	0 0000	16	264	0 128155	0 256311	0 02	0 0004	16	168	0 081553	0 163107	-0 07	0 0045
17	218	0.1058	0 2117	-0 04	0 0013	17	216	0 104854	0 209709	-0 03	0 0008	17	239	0.116019	0.232039	0 00	0 0000
18	230	0 1117	0 2233	-0.02	0 0006	18	216	0.104854	0 209709	-0.03	0 0008	18	232	0 112621	0 225243	0 00	0 0000
19	245	0 1189	0.2379	-0 01	0 0001	19	230	0 11165	0 223301	-0 01	0 0002	19	238	0.115534	0 231068	0 00	0 0000
20	262	0 1272	0 2544	0 01	0.0000	20	253	0 122816	0 245631	0 01	0 0001	20	218	0 105825	0 21165	-0 02	0 0003
21	247	0 1199	0 2398	-0 01	0.0001	21	247	0 119903	0 239806	0 00	0 0000	21	311	0 150971	0.301942	0 07	0 0052
22	251	0 1218	0 2437	0 00	0 0000	22	245	0 118932	0 237864	0 00	0 0000	22	227	0 110194	0 220388	-0 01	0 0001
23	259	0 1257	0.2515	0 00	0 0000	23	240	0 116505	0.23301	0 00	0 0000	23	272	0 132039	0 264078	0 03	0 0012
24	288	0 1398	0.2796	0.03	0 0010	24	205	0 099515	0 199029	-0 04	0 0015	24		0	0	0 00	0.0000
25	253	0.1228	0 2456	0 00	0 0000	25	239	0.116019	0.232039	-0 01	0 0000	25		0	0	0 00	0 0000
26	0	0	0	0 00	0 0000	26	271	0 131553	0 263107	0 00	0 0000	26		0	0	0 00	0.0000
27	295	0 1432	0.2864	0 04	0 0015	27	264	0 128155	0 256311	0 02	0.0004	27		0	0	0 00	0 0000
28	238	0.1155	0 2311	-0 02	0 0003	28	237	0.115049	0 230097	-0 01	0 0001	28		0	0	0 00	0.0000
29	234	0.1136	0 2272	-0.02	0 0004	29	233	0 113107	0.226214	-0 01	0 0001	29		0	0	0 00	0 0000
30	229	0 1112	0 2223	-0 03	0 0006	30	245	0 118932	0 237864	0 00	0 0000	30		0	0	0 00	0.0000
					0 01050816						0 0109347						0 0437779
Mean			**0.24740**			**Mean**			**0.23746**			**Mean**			**0.23010**		
Variance Vx					0 00037529	Variance Vx					0 00039052	Variance Vx					0 001903
Std devn = Sqrt of Variance					0 01937244	Std devn = Sqrt of Variance					0.01976171	Std devn = Sqrt of Variance					0 043627
no of FOV's (n)					28	no of FOV's (n)					29	no of FOV's (n)					
Square root of n					5 29150262	Square root of n					5.38516481	Square root of n					4.795831
Std error of mean =Stddevn/Sqrt n					0 00366105	Std error of mean =Stddevn/Sqrt n					0 00366966	Std error of mean =Stddevn/Sqrt n					0 009097
95% confidence interval					**0.01464419**	**95% confidence interval**					**0.01467863**	**95% confidence interval**					**0.036388**

;R 127RD				Grid	H 2000	V 46
;β	Pʟaβ	Paα	Pʟaα	Cont (x)	(x - x)	Squ (x-x)
35	0 1286	31	0 015	0 1896	0 03	0 0009
35	0 1286	29	0 0141	0 1796	0 02	0 0004
76	0 134	19	0 0092	0 121	-0 04	0 0016
75	0 1335	27	0 0131	0 1641	0 00	0 0000
40	0 1165	29	0 0141	0 1946	0 03	0 0012
63	0 1277	24	0 0117	0 1543	-0 01	0 0000
89	0 1403	34	0 0165	0 1905	0 03	0 0009
66	0 1291	29	0 0141	0 179	0 02	0 0003
65	0 1286	23	0 0112	0 1479	-0 01	0 0002
29	0 1112	45	0 0218	0 2821	0 12	0 0148
76	0 134	24	0 0117	0 1481	-0 01	0 0002
36	0 1146	32	0 0155	0 2133	0 05	0 0028
0	0		0	0	0 00	0 0000
'31	0 1121	30	0 0146	0 2062	0 05	0.0021
'60	0 1262	29	0 0141	0 1824	0 02	0 0005
:50	0 1214	28	0 0136	0 183	0 02	0 0005
:18	0 1058	29	0 0141	0 2101	0 05	0 0025
:30	0 1117	19	0 0092	0 1418	-0 02	0 0003
:45	0.1189	18	0 0087	0 1281	-0 03	0 0010
:62	0.1272	15	0 0073	0 1027	-0 06	0 0033
247	0 1199	22	0 0107	0 1512	-0 01	0 0001
251	0 1218	24	0 0117	0 1605	0 00	0 0000
259	0.1257	30	0 0146	0 1881	0 03	0 0008
288	0 1398	18	0.0087	0 1111	-0 05	0 0024
253	0.1228	19	0 0092	0.1306	-0 03	0 0009
0	0		0	0	0 00	0 0000
295	0 1432	21	0 0102	0 1246	-0 04	0 0013
238	0 1155	15	0 0073	0 1119	-0 05	0 0023
234	0 1136	14	0 0068	0 1069	-0 05	0 0029
229	0.1112	11	0 0053	0.0876	-0 07	0 0053
						0 049406
				0.16040		
ce Vx						0 001764
vn = Sqrt of Variance						0.042006
OV's (n)						28
e root of n						5.291503
or of mean =Stddevn/Sqrt n						0 007938
onfidence interval						**0.031753**

	ESR 137RD				Grid	H 2000	V 46
FOV's	Paβ	Pʟaβ	Paα	Pʟaα	Cont (x)	(x - x)	Squ (x-x)
1	238	0 115534	20	0 009709	0 143885	0.03	0 0009
2	266	0 129126	27	0 013107	0 16875	0 05	0 0030
3	265	0 128641	17	0 008252	0 113712	0 00	0 0000
4	251	0 121845	24	0 01165	0 160535	0 05	0 0022
5	292	0 141748	18	0 008738	0 109756	0 00	0 0000
6	242	0 117476	14	0 006796	0 103704	-0 01	0 0001
7	219	0 106311	25	0 012136	0 185874	0 07	0 0052
8	228	0 11068	13	0 006311	0 102362	-0 01	0 0001
9	230	0 11165	10	0 004854	0 08	-0 03	0 0012
10	0	0		0	0	0 00	0 0000
11	263	0 12767	12	0 005825	0 083624	-0 03	0 0009
12	281	0 136408	20	0 009709	0 124611	0 01	0 0001
13	265	0 128641	17	0 008252	0 113712	0 00	0 0000
14	235	0 114078	13	0 006311	0 099617	-0 01	0 0002
15	213	0 103398	13	0 006311	0 108787	-0 01	0 0000
16	264	0 128155	16	0 007767	0 108108	-0 01	0 0000
17	216	0 104854	9	0 004369	0 076923	-0 04	0 0014
18	216	0 104854	13	0 006311	0 107438	-0 01	0 0000
19	230	0 11165	15	0 007282	0 115385	0 00	0 0000
20	253	0 122816	36	0 017476	0 221538	0 11	0 0116
21	247	0.119903	22	0 01068	0 151203	0 04	0 0014
22	245	0.118932	34	0 016505	0.217252	0.10	0 0107
23	240	0 116505	23	0 011165	0 160839	0 05	0 0022
24	205	0 099515	10	0 004854	0.088889	-0 03	0 0006
25	239	0 116019	7	0 003398	0 055336	-0.06	0.0034
26	271	0 131553	7	0 003398	0 049123	-0 06	0.0042
27	264	0.128155	5	0 002427	0 036496	-0 08	0 0060
28	237	0 115049	5	0 002427	0.040486	-0.07	0.0054
29	233	0.113107	12	0 005825	0 093385	-0 02	0.0004
30	245	0.118932	11	0 00534	0.082397	-0 03	0.0010
							0 062281
Mean					**0.11392**		
Variance Vx							0.002148
Std devn = Sqrt of Variance							0 046342
no of FOV's (n)							29
Square root of n							5 385165
Std error of mean =Stddevn/Sqrt n							0 008606
95% confidence interval							**0.034422**

	ESR 74RD						
FOV'	Paβ	Pʟaβ	Paα	Pʟaα	Cont (x)	(x-x)	Squ (x-x)
1	261	0 126699	14	0 006796	0 096886	0 03	0 00101
2	211	0 102427	3	0 001456	0 02765	-0 04	0 00141
3	274	0 13301	8	0 003883	0 055172	-0 01	0 00010
4	231	0 112136	10	0 004854	0 079681	0 01	0 00021
5	308	0 149515	10	0 004854	0 060976	0 00	0 00002
6	193	0 093689	4	0 001942	0 039801	-0 03	0 00064
7	375	0 182039	11	0 00534	0 055416	-0 01	0 00009
8	221	0 107282	11	0 00534	0 090535	0 03	0 00065
9	191	0 092718	5	0 002427	0 049751	-0 02	0 00024
10	179	0 086893	10	0 004854	0	-0 07	0.00424
11	253	0 122816	10	0 004854	0 07326	0 01	0 00007
12	247	0 119903	10	0 004854	0.074906	0 01	0 00010
13	195	0 09466	6	0 002913	0 057971	-0 01	0 00005
14	183	0 088835	7	0 003398	0 071066	0 01	0 00004
15	224	0 108738	7	0 003398	0 058824	-0 01	0.00004
16	168	0 081553	6	0 002913	0 066667	0 00	0 00000
17	239	0 116019	7	0.003398	0.055336	-0 01	0 00010
18	232	0 112621	0	0	0		0 00000
19	238	0 115534	9	0 004369	0 070313	0 01	0.00003
20	218	0 105825	13	0.006311	0.106557	0.04	0.00172
21	311	0 150971	9	0 004369	0.054711	-0 01	0 00011
22	227	0 110194	9	0 004369	0 073469	0 01	0 00007
23	272	0.132039	7	0 003398	0 048951	-0 02	0.00026
24		0		0	0	0 00	0.00000
25		0		0	0	0 00	0 00000
26		0		0	0	0 00	0.00000
27		0		0	0	-0.07	0.00424
28		0		0	0	-0 07	0.00424
29		0		0	0	-0 07	0 00424
30		0		0	0	-0.07	0 00424
							0 02814
Mean					**0.06514**		
Variance Vx							0.00134
Std devn = Sqrt of Variance							0 03661
no of FOV's (n)							21
Square root of n							4 58258
Std error of mean =Stddevn/Sqrt n							0 00799
95% confidence interval							**0.03195**

APPENDIX B

Figure B-1. Polarisation behaviour of the rolling plane of the ESR137 alloy in 0.5N H_2SO_4 obtained using a flat cell at a scan rate of 0.166 mV / sec .

Figure B-2 Polarisation behaviour of the rolling plane of the ESR74 alloy in 0.5N H_2SO_4obtained using a flat cell at a scan rate of 0.166 mV / sec

Figure B-3 Polarisation behaviour of the rolling plane of the ESR127 alloy in 0.5N H_2SO_4 obtained using a flat cell at a scan rate of 0.166 mV / sec

APPENDIX B

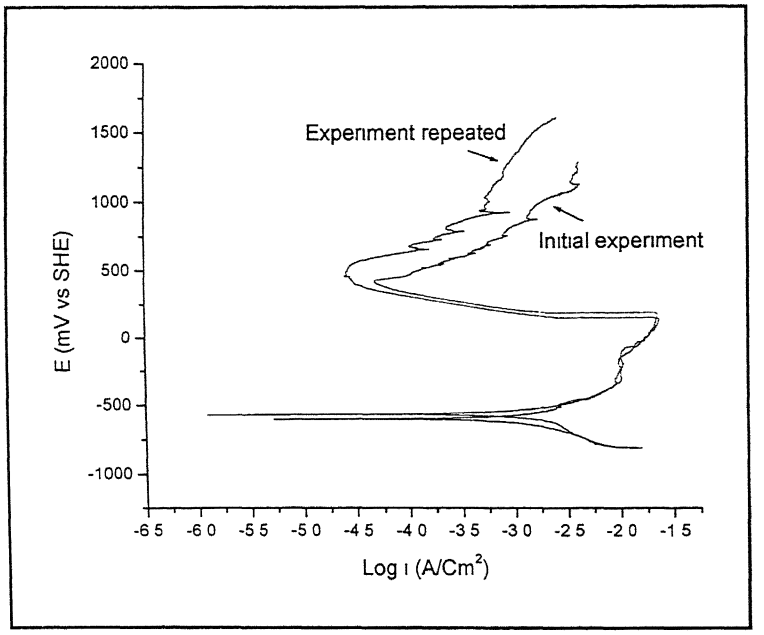

Figure B-1. Polarisation behaviour of the rolling plane of the ESR137 alloy in 0.5N H_2SO_4 obtained using a flat cell at a scan rate of 0.166 mV / sec .

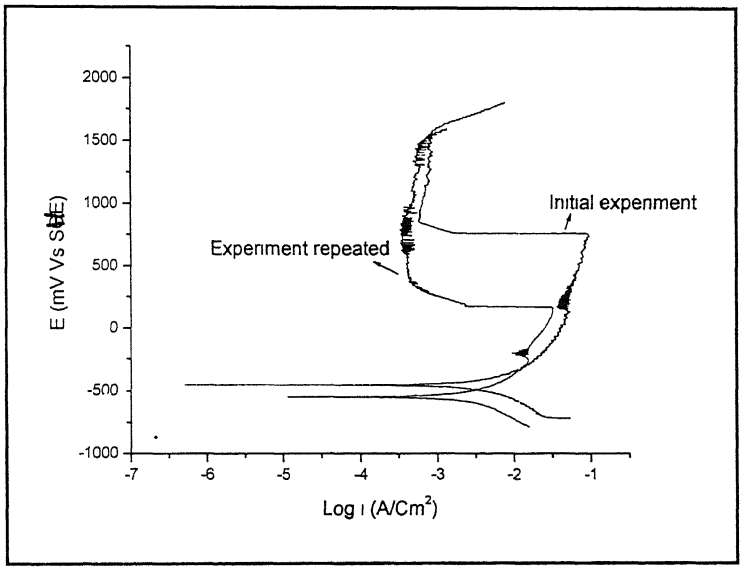

Figure B-2. Polarisation behaviour of the rolling plane of the ESR74 alloy in 0.5N H_2SO_4 obtained using a flat cell at a scan rate of 0.166 mV / sec .

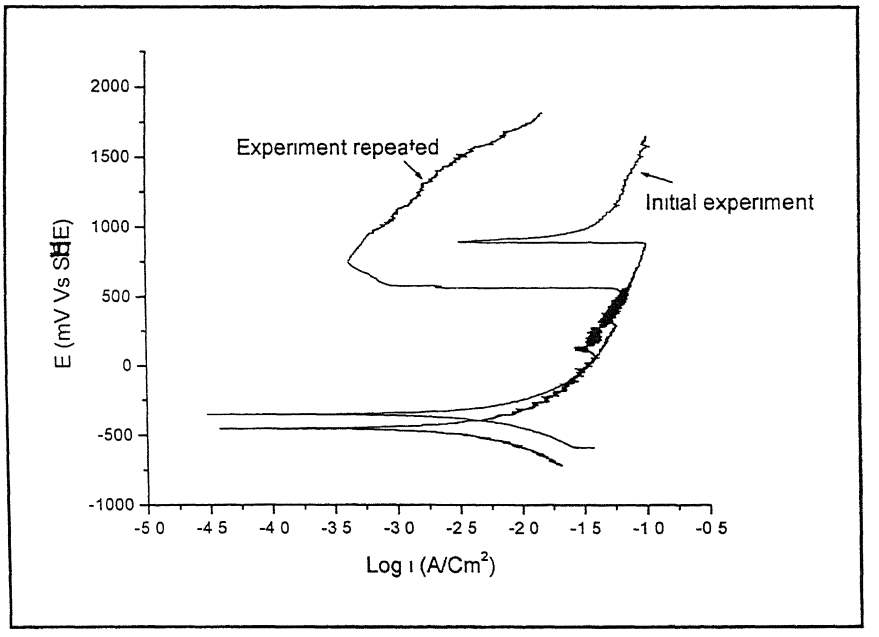

Figure B-3. Polarisation behaviour of the rolling plane of the ESR127 alloy in 0.5N H_2SO_4 obtained using a flat cell at a scan rate of 0.166 mV / sec .

APPENDIX C

Table C-1 **Short term immersion testing conducted on ESR 127 (Sample-1)**

date 10.10.03 **COMPOSITION (in Wt%) = Fe- 18.52Al-3.65C (at%)**

Elect 0 5N sulfuric acid **Area of the specimen exposed =** 1 174902 Sqinches

Sl No	Date of experime	Starting time in hours	Time when reading was taken	Exposure time (t) in mts	Exposure time (in hrs)	Cumulative exposure time in mts	Cumulative exposure time in hrs	Intitial wieght (g)	Wt at time t (g)	Weight change in gms	Change wt in mg	Exp area specimen in sqinch	Corrosion rate m/year	Corrosion rate mmpy
1	09 10 03	11 00 am	11.45 am	45	0 75	45 00	0.75	9 6955	9.6286	0.067	66.90	1.174902	5578	142
2	09.10 03	12.00 am	12 50 pm	50	0 83	95.00	1.35	9 6286	9 5355	0.093	93.10	1.174902	6986	177
3	09.10.03	01 00 pm	01 50 pm	50	0.83	145.00	2 25	9 5355	9 4275	0 108	108.00	1.174902	8104	206
4	09.10.03	02.00 pm	02.50 pm	50	0 83	195 00	3 15	9 4275	9.3213	0.106	106.20	1.174902	7969	202
5	09 10.03	03.00 pm	03.50 pm	50	0 83	245.00	4.05	9 3213	9 2307	0.091	90.60	1.174902	6799	173
6	09.10.03	04 00 pm	04 50 pm	50	0.83	295.00	4 55	9.2307	9 1554	0 075	75.30	1.174902	5650	144
7	09.10 03	05.00 pm	05.50 pm	50	0.83	345.00	5.45	9.1554	9 0740	0 081	81.40	1.174902	6108	155
8	09.10.03	06.00 pm	06.50 pm	50	0.83	395.00	6.35	9 0740	8.9858	0.088	88.20	1.174902	6618	168
9	09.10.03	07.00 pm	07.50 pm	50	0.83	445.00	7.25	8.9858	8.8972	0.089	88.60	1.174902	6648	169
10	09.10.03	08.02 pm	08.50 am	48	0.80	493.00	8.13	8 8972	8.8206	0.077	76.60	1 174902	5987	152
11	09.10.03	09.00 pm	09.50 am	50	0.83	543.00	9 03	8.8206	8 7393	0 081	81.30	1.174902	6101	155
12	09.10.03	10.00 pm	10.50 pm	50	0.83	593.00	9.53	8.7393	8.6711	0.068	68.20	1.174902	5118	130
13	09.10.03	11.00 pm	11.50 pm	50	0.83	643.00	10.43	8.6711	8.5901	0.081	81.00	1.174902	6078	154

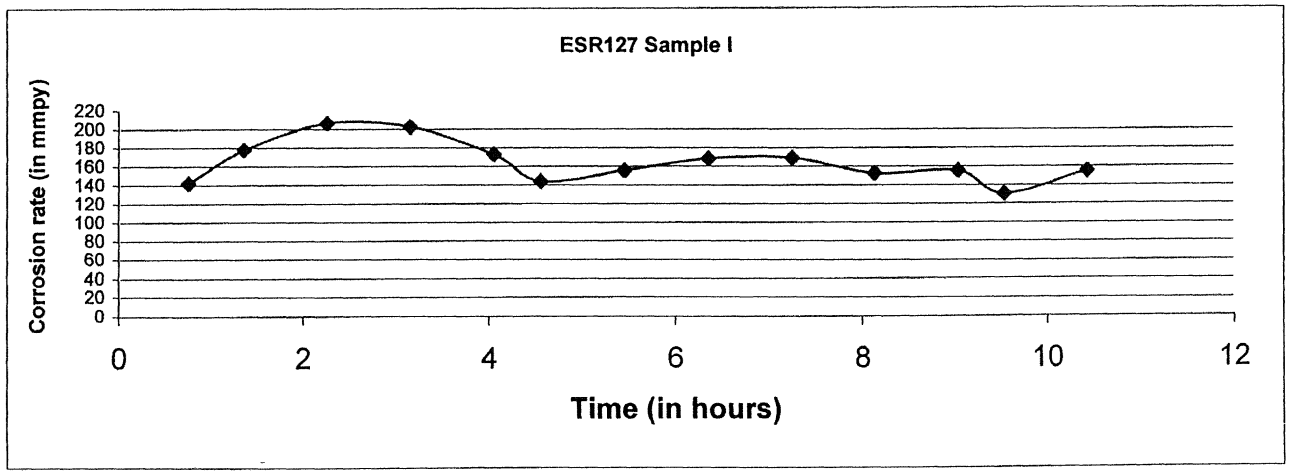

Table C-2 **Short term immersion testing conducted on ESR 127 (Sample-2)**

ESR 127 **Sample - II**

date 10 10 03 **COMPOSITION (in Wt%) = Fe- 18.52Al-3.65C (at%)**

Elect. 0 5N sulfuric acid **Area of the specimen exposed =** 0.771902 Sqinches

Sl No	Date of experime	Starting time in hours	Time when reading was taken	Exposure time (t) in mts	Exposure time (in hrs)	Cumulative exposure time in mts	Cumulative exposure time in hrs	Intitial wieght (g)	Wt at time t (g)	Weight change in gms	Change wt in mg	Exp area specimen in sqinch	Corrosion rate m/year	Corrosion rate mmpy
1	09 10 03	11 00 am	11.45 am	45	0 75	45 00	0 75	5 3762	5 3303	0.046	45.90	0.771902	5825	148
2	09 10.03	12 00 am	12 50 pm	50	0 83	95 00	1 35	5 3303	5 2658	0 065	64.50	0 771902	7367	187
3	09 10 03	01 00 pm	01 50 pm	50	0 83	145 00	2 25	5 2658	5 1999	0 066	65 90	0 771902	7527	191
4	09.10 03	02 00 pm	02 50 pm	50	0 83	195 00	3 15	5 1999	5 1314	0 069	68.50	0.771902	7824	199
5	09 10.03	03 00 pm	03.50 pm	50	0 83	245 00	4 05	5 1314	5 0714	0 060	60.00	0.771902	6853	174
6	09.10.03	04 00 pm	04 50 pm	50	0 83	295.00	4 55	5.0714	5.0135	0.058	57.90	0 771902	6613	168
7	09 10 03	05 00 pm	05 50 pm	50	0.83	345 00	5 45	5 0135	4 9567	0.057	56.80	0.771902	6487	165
8	09.10 03	06.00 pm	06.50 pm	50	0 83	395 00	6 35	4 9567	4.8974	0 059	59 30	0 771902	6773	172
9	09.10.03	07.00 pm	07.50 pm	50	0 83	445 00	7 25	4 8974	4.8402	0.057	57.20	0.771902	6533	166
10	09.10.03	08 02 pm	08.50 am	48	0 80	493.00	8 13	4.8402	4.7901	0.050	50.10	0.771902	5961	151
11	09 10.03	09 00 pm	09.50 am	50	0 83	543.00	9 03	4 7901	4 7368	0.053	53 30	0 771902	6088	155
12	09 10.03	10.00 pm	10.50 pm	50	0 83	593 00	9 53	4 7368	4 6877	0 049	49.10	0 771902	5608	142
13	09 10.03	11.00 pm	11 50 pm	50	0 83	643 00	10 43	4 6877	4.6391	0.049	48.60	0.771902	5551	141

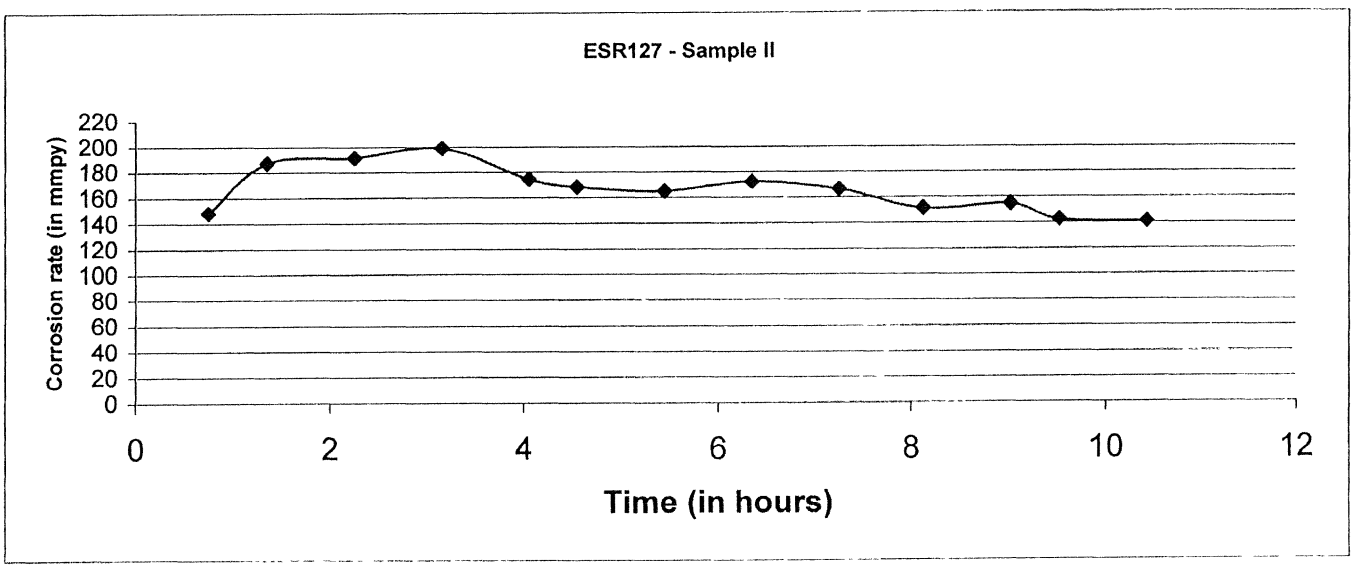

Table C-3 **Short term immersion testing conducted on ESR137 (Sample-1)**

Date 09 10 03 **COMPOSITION (in Wt%) = Fe-19.24 Al-3.29C-0.07Ce (at%)**

Elect 0 5N Sulfuric acid **Area of the specimen exposed =** 0 864127 Sqinches

Sl No	Date of experime	Starting time in hours	Time when reading was taken	Exposure time (t) in mts	Exposure time in hours	Cumulative exposure time in hours	Cumulative exposure time in mts	Intitial wieght (g)	Wt at time t (g)	Weight change in gms	Change wt in mg	Exp area specimen in sqinch	Corrosion rate m/year	Corrosion rate mmpy
1	09 10 03	11.00 am	11 45 am	45	0 75	0 75	45 00	6.8410	6 8253	0 016	15 70	0 864127	1780	45
2	09 10 03	12 00 am	12 50 pm	50	0 83	1 35	95 00	6 8253	6 8047	0 021	20.60	0.864127	2102	53
3	09 10.03	01.00 pm	01 50 pm	50	0 83	2 25	145 00	6 8047	6 7810	0.024	23.70	0 864127	2418	61
4	09 10 03	02 00 pm	02 50 pm	50	0 83	3 15	195 00	6 7810	6.7570	0.024	24 00	0.864127	2449	62
5	09.10 03	03 00 pm	03 50 pm	50	0 83	4 05	245.00	6 7570	6 7347	0 022	22 30	0.864127	2275	58
6	09 10.03	04 00 pm	04 50 pm	50	0 83	4 55	295 00	6 7347	6 7126	0 022	22.10	0.864127	2255	57
7	09 10 03	05.00 pm	05.50 pm	50	0 83	5 45	345 00	6 7126	6 6904	0 022	22.20	0 864127	2265	58
8	09 10 03	06.00 pm	06 50 pm	50	0 83	6.35	395 00	6 6904	6.6675	0 023	22.90	0.864127	2336	59
9	09 10 03	07 00 pm	07 50 pm	50	0 83	7 25	445.00	6 6675	6 6433	0 024	24.20	0.864127	2469	63
10	09.10.03	08.02 pm	08 50 am	48	0 80	8 13	493 00	6 6433	6 6203	0.023	23.00	0.864127	2444	62
11	09.10 03	09.00 pm	09.50 am	50	0 83	9 03	543 00	6 6203	6 5978	0.023	22.50	0 864127	2296	58
12	09.10 03	10 00 pm	10 50 pm	50	0 83	9 53	593 00	6 5978	6.5748	0.023	23 00	0 864127	2347	60
13	09 10 03	11.00 pm	11 50 pm	50	0 83	10.43	643 00	6.5748	6.5518	0 023	23.00	0 864127	2347	60

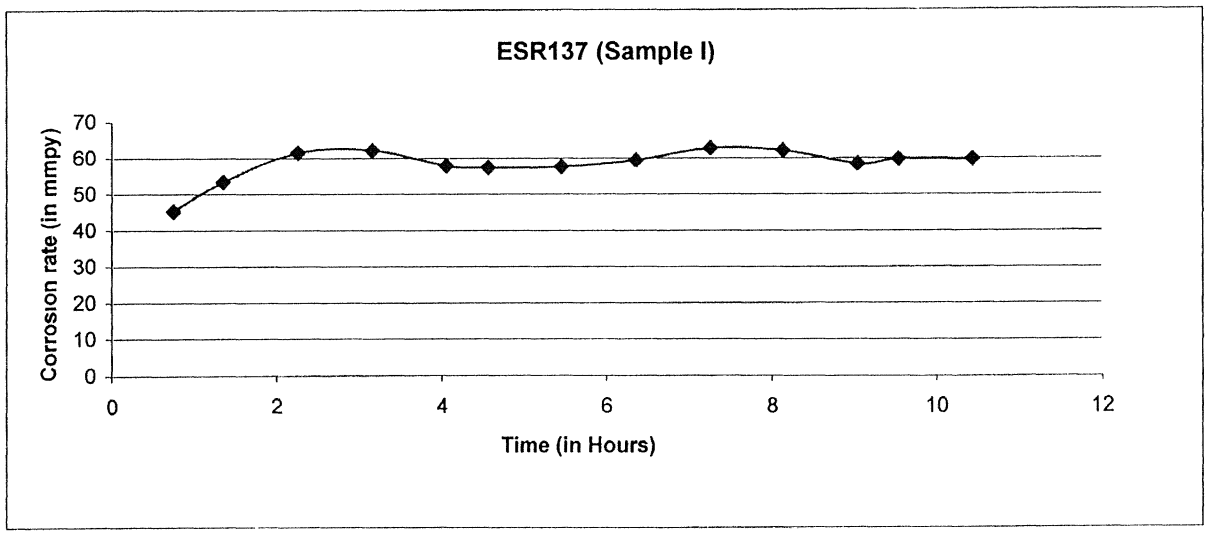

Table C-4 **Short term immersion testing conducted on ESR137 (Sample-2)**

ESR 137 **Sample - 2**

Date 09.10 03 **COMPOSITION (in Wt%) = Fe-19.24 Al-3.29C-0.07Ce (at%)**

Elect 0 5N Sulfuric acid **Area of the specimen exposed =** 0.937752 Sqinches

Sl No	Date of experime	Starting time in hours	Time when reading was taken	Exposure time (t) in mts	Exposure time in hours	Cumulative exposure in hours	Cumulative exposure time in mts	Intitial wieght (g)	Wt at time t (g)	Weight change in gms	Change wt in mg	Exp area specimen in sqinch	Corrosion rate m/year	Corrosion rate mmpy
1	09.10 03	11 00 am	11 45 am	45	0 75	0 75	45 00	7 2635	7 2465	0 017	17 00	0.937752	1776	45
2	09 10 03	12 00 am	12 50 pm	50	0.83	1 35	95 00	7 2465	7 2262	0 020	20.30	0.937752	1909	48
3	09.10 03	01 00 pm	01.50 pm	50	0 83	2 25	145 00	7 2262	7 2005	0 026	25 70	0 937752	2416	61
4	09 10.03	02.00 pm	02 50 pm	50	0 83	3 15	195 00	7 2005	7 1753	0 025	25 20	0 937752	2369	60
5	09 10.03	03 00 pm	03 50 pm	50	0 83	4.05	245 00	7 1753	7 1511	0 024	24 20	0.937752	2275	58
6	09 10 03	04.00 pm	04.50 pm	50	0.83	4 55	295 00	7 1511	7 1278	0.023	23.30	0 937752	2191	56
7	09.10 03	05 00 pm	05 50 pm	50	0.83	5 45	345 00	7.1278	7.1030	0 025	24 80	0 937752	2332	59
8	09 10 03	06 00 pm	06 50 pm	50	0 83	6 35	395 00	7 1030	7 0782	0 025	24.80	0 937752	2332	59
9	09.10.03	07 00 pm	07 50 pm	50	0 83	7 25	445 00	7 0782	7.0504	0 028	27.80	0.937752	2614	66
10	09.10.03,	08 02 pm	08.50 am	48	0.80	8.13	493 00	7 0504	7 0245	0.026	25.90	0.937752	2536	64
11	09.10.03	09.00 pm	09 50 am	50	0 83	9 03	543 00	7 0245	6 9960	0.028	28.50	0.937752	2679	68
12	09 10.03	10.00 pm	10 50 pm	50	0.83	9.53	593 00	6.9960	6.9696	0 026	26 40	0 937752	2482	63
13	09 10 03	11 00 pm	11 50 pm	50	0 83	10.43	643.00	6 9696	6.9403	0 029	29 30	0 937752	2755	70

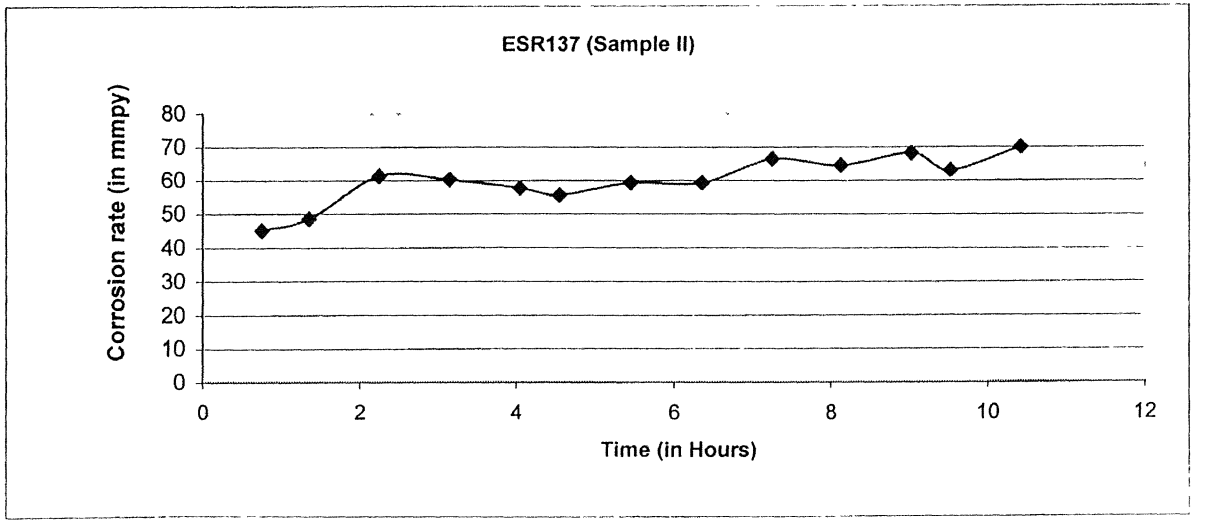

Table C-5 **Short term immersion testing conducted on ESR74 (Sample-1)**

date 10 10 03 **COMPOSITION (in Wt%) = Fe-19.9 Al-2.0 C (at%)** (ESR74)

Electrolyte 0 5N Sulfuric acid **Area of the specimen exposed =** 0 561101 Sqinches

Sl No	Date of experime	Starting time in hours	Time when reading was taken	Exposure time (t) in mts	Exposure time (in hrs)	Cumulative exposure time in mts	Cumulative exposure time in hrs	Intitial wieght (g)	Wt at time t (g)	Weight change in gms	Change wt in mg	Exp area specimen in sqinch	Corrosion rate m/year	Corrosion rate mmpy
1	09 10 03	11 00 am	11 45 am	45	0 75	45 00	0 75	3 5074	3 4760	0 031	31.40	0.561101	5482	139
2	09.10 03	12.00 am	12 50 pm	50	0 83	95.00	1 35	3 4760	3 4353	0 041	40.70	0.561101	6395	162
3	09 10 03	01.00 pm	01 50 pm	50	0 83	145.00	2 25	3 4353	3 3915	0.044	43.80	0 561101	6882	175
4	09 10.03	02 00 pm	02 50 pm	50	0 83	195.00	3 15	3.3915	3 3469	0 045	44 60	0 561101	7008	178
5	09.10.03	03 00 pm	03.50 pm	50	0.83	245.00	4 05	3 3469	3 3047	0 042	42.20	0.561101	6631	168
6	09.10 03	04.00 pm	04 50 pm	50	0 83	295.00	4 55	3 3047	3.2660	0.039	38.70	0.561101	6081	154
7	09 10 03	05.00 pm	05 50 pm	50	0 83	345 00	5.45	3 2660	3.2269	0.039	39.10	0.561101	6144	156
8	09 10 03	06 00 pm	06 50 pm	50	0 83	395 00	6.35	3.2269	3 1867	0 040	40 20	0 561101	6316	160
9	09 10.03	07.00 pm	07 50 pm	50	0 83	445.00	7.25	3.1867	3.1445	0 042	42.20	0.561101	6631	168
10	09.10.03	08.02 pm	08.50 am	48	0 80	493 00	8 13	3 1445	3.1108	0.034	33.70	0.561101	5516	140
11	09.10.03	09.00 pm	09.50 am	50	0.83	543.00	9 03	3.1108	3.0697	0.041	41 10	0.561101	6458	164
12	09.10.03	10.00 pm	10.50 pm	50	0.83	593.00	9.53	3.0697	3.0342	0.036	35.50	0 561101	5578	142
13	09.10.03	11.00 pm	11.50 pm	50	0.83	643 00	10.43	3 0342	2 9953	0 039	38.90	0.561101	6112	155

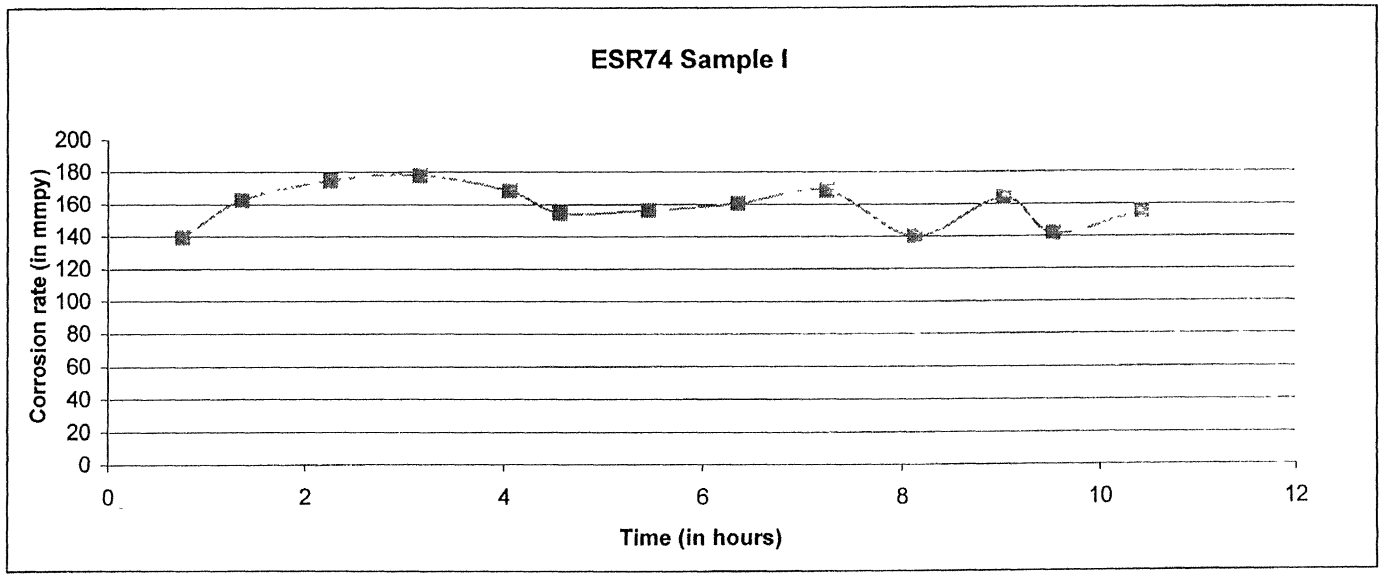

Table C-6 **Short term immersion testing conducted on ESR74 (Sample-2)**

Sample - II

date .10 10.03

Elect. 0 5N Sulfuric acid

COMPOSITION (in Wt%) = Fe- 19.9Al-2.0C (at%) (ESR74)

Area of the specimen exposed = 1 041602 Sqinches

Sl No	Date of experime	Starting time in hours	Time when reading was taken	Exposure time (t) in mts	Exposure time (in hrs)	Cumulative exposure time in mts	Cumulative exposure time in hrs	Intitial wieght (g)	Wt at time t (g)	Weight change in gms	Change wt in mg	Exp area specimen in sqinch	Corrosion rate m/year	Corrosion rate mmpy
1	09 10 03	11 00 am	11 45 am	45	0 75	45.00	0 75	6 6400	6 5933	0 047	46 70	1 041602	4392	112
2	09 10.03	12 00 am	12 50 pm	50	0 83	95 00	1 35	6 5933	6 5297	0 064	63 60	1 041602	5383	137
3	09 10 03	01 00 pm	01 50 pm	50	0 83	145 00	2 25	6 5297	6 4627	0 067	67.00	1 041602	5671	144
4	09 10.03	02 00 pm	02.50 pm	50	0 83	195 00	3 15	6 4627	6 3960	0 067	66.70	1.041602	5646	143
5	09 10.03	03 00 pm	03 50 pm	50	0 83	245 00	4 05	6 3960	6 3373	0.059	58.70	1.041602	4969	126
6	09.10 03	04 00 pm	04 50 pm	50	0 83	295 00	4 55	6 3373	6 2847	0.053	52.60	1.041602	4452	113
7	09.10 03	05.00 pm	05.50 pm	50	0.83	345.00	5.45	6.2847	6 2304	0.054	54 30	1.041602	4596	117
8	09 10.03	06 00 pm	06.50 pm	50	0 83	395 00	6 35	6 2304	6 1712	0 059	59 20	1.041602	5011	127
9	09 10.03	07 00 pm	07 50 pm	50	0.83	445 00	7.25	6 1712	6 1120	0.059	59.20	1.041602	5011	127
10	09.10.03	08.02 pm	08 50 am	48	0 80	493 00	8.13	6 1120	6 0601	0.052	51.90	1.041602	4576	116
11	09 10.03	09 00 pm	09.50 am	50	0.83	543 00	9.03	6.0601	6.0065	0.054	53.60	1.041602	4537	115
12	09.10 03	10.00 pm	10 50 pm	50	0.83	593.00	9 53	6.0065	5 9582	0 048	48.30	1 041602	4088	104
13	09.10 03	11 00 pm	11.50 pm	50	0 83	643 00	10 43	5 9582	5 9088	0.049	49 40	1.041602	4181	106

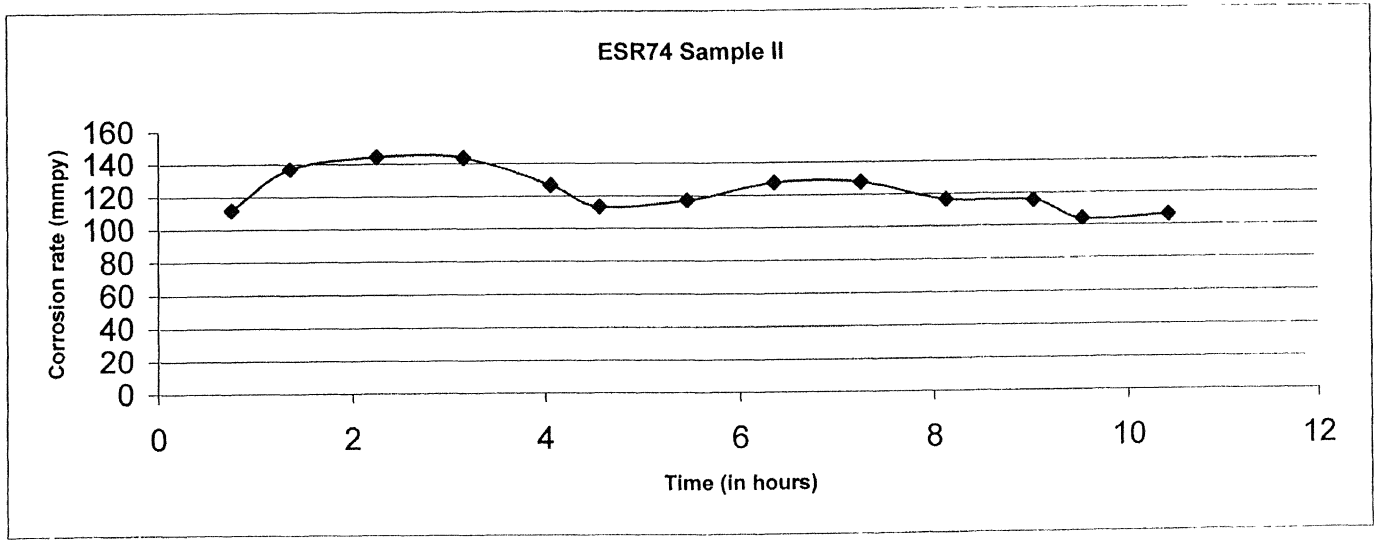

Table C 7 **Long term immersion testing done on ESR 127 sample**

date .23 11 03

Elect. 0.5N

COMPOSITION (in Wt%) = Fe- 18.52Al-3.65C (at%)

Area of the specimen exposed = 0 59644 Sqinches

Sl No	Date of starting experim	Starting time in hours	date of ending of experiments	Time when reading was taken	Exposure time (t) in mts	Exposure time in hrs	Cumulative exposure time in mts	Cumulative exposure time in hrs	Intitial wieght (g)	Wt at time t (g	Weight change in gms	Change wt in mg	Exp area specimen in sqinch	Corrosion rate m/year	Corrosion rate mmpy
1	23 11 03	10.20 hrs	23 11 03	22.20 hrs	720	12 00	720 00	12 00	3 2740	2 7200	0 554	554 00	0 59644	5691	145
2	23 11.03	23.40 hrs	24.11.03	11.40 hrs	720	12 00	1440 00	24 00	2 7200	2 3200	0 400	400 00	0.4929	4972	126
3	24.11.03	13 00 hrs	25 11 03	01 00 hrs	720	12 00	2160 00	36 00	2 3200	1.9870	0 333	333 00	0 42315	4822	122
4	25 11 03	02.00 hrs	25.11 03	14 00 hrs	720	12 00	2880.00	48.00	1 9870	1 7300	0 257	257 00	0 39215	4015	102
5	25 11 03	15 00 hrs	26.11.03	03 00 hrs	720	12 00	3600 00	60 00	1 7300	1 5300	0 200	200 00	0 3658	3350	85
6	25 11 03	04 00 hrs	27.11 03	16 00 hrs	720	12 00	4320.00	72 00	1 5300	1 3900	0 140	140 00	0 32473	2642	67
7	27.11 03	17.00 hrs	28 11 03	08 00 hrs	900	15 00	5220 00	87 00	1 3900	1 2640	0.126	126.00	0 2852	2165	55

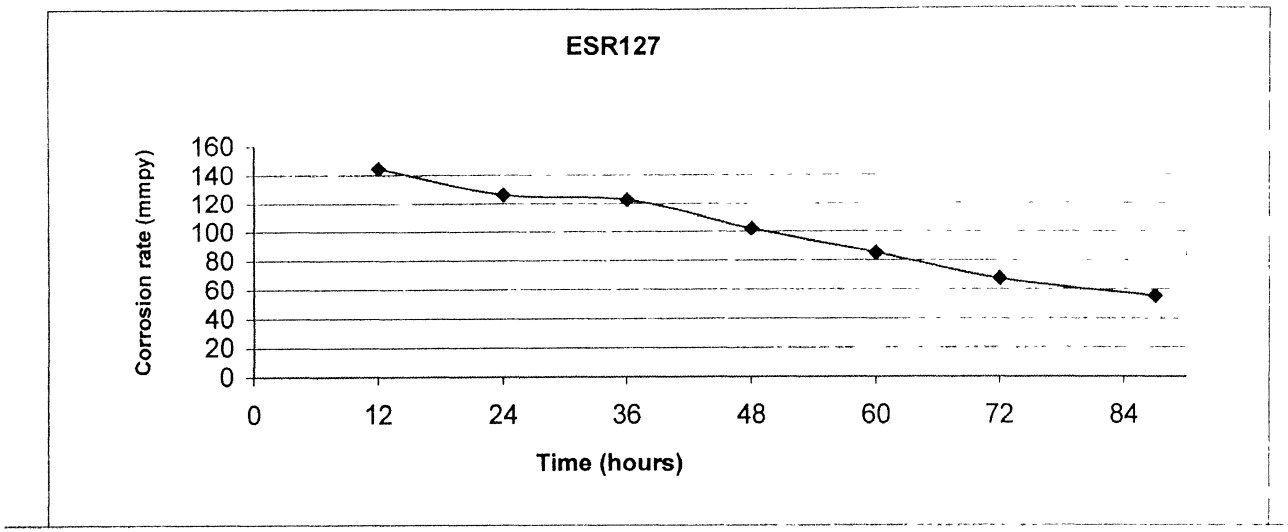

Table C 8 Long term immersion testing done on sample ESR137

date 23 11 03
Elect 0 5N

COMPOSITION (in Wt%) = Fe- 18.52Al-3.65C (at%)
Area of the specimen exposed = 0.788952 Sqınches

Sl No	Date of starting experim	Starting time in hours	date of ending of expmt	Time when reading was taken	Exposure time (t) in mts	Exposure time in hrs	Cumulative exposure time in mts	Cumulative exposure time in hrs	Intitial wieght (g)	Wt at time t (g)	Weight change in gms	Change wt in mg	Exp area specimen in sqinch	Corrosio rate m/year	Corrosion rate mmpy
1	23 11 03	10 20 hrs	23 11 03	22 20 hrs	720	12 00	720 00	12 00	5 0940	4 8620	0 232	232 00	0 7890	1802	46
2	23 11 03	23 40 hrs	24 11 03	11 40 hrs	720	12 00	1440 00	24 00	4 8620	4 6590	0 203	203.00	0.774227	1607	41
3	24.11 03	13.00 hrs	25 11.03	01 00 hrs	720	12 00	2160 00	36 00	4 6590	4 4450	0 214	214 00	0 7595	1727	44
4	25 11 03	02.00 hrs	25 11 03	14.00 hrs	720	12 00	2880 00	48 00	4 4450	4 2410	0 204	204 00	0 7448	1679	43
5	25.11.03	15.00 hrs	26 11 03	03 00 hrs	720	12 00	3600 00	60 00	4 2410	4 0420	0 199	199.00	0.7301	1671	42
6	25.11 03	04 00 hrs	27.11 03	16 00 hrs	720	12 00	4320 00	72 00	4 0420	3 8710	0 171	171.00	0.7153	1465	37
7	27 11 03	17.00 hrs	28 11 03	08 00 hrs	900	15 00	5220.00	87 00	3 8710	3 6720	0 199	199 00	0 7006	1393	35

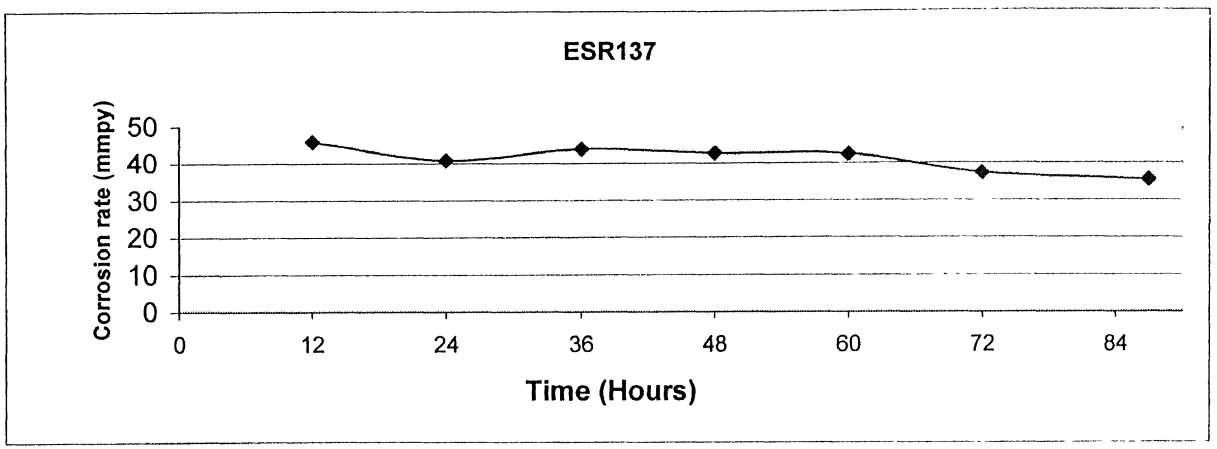

Table C 9 Long term immersion testing done on sample ESR74

date 23.11 03
Elect 0 5N

COMPOSITION (in Wt%) = Fe- 18.52Al-3.65C (at%)
Area of the specimen exposed = 0.731601 Sqinches

Sl No	Date of starting experim	Starting time in hours	date of ending of experiments	Time when reading was taken	Exposur time (t) in mts	Exposure time (in hr	Cumulative exposure time in mts	Cumulative exposure time in hrs	Intitial wieght (g)	Wt at time t(g)	Weight change in gms	Change i wt in mg	Exp area specimen in sqinch	Corrosior rate m/year	Corrosion rate mmpy
1	23 11 03	10 20 hrs	23 11 03	22 20 hrs	720	12 00	720 00	12 00	4 3160	3 6420	0 674	674.00	0 7316	5640	143
2	23.11.03	23 40 hrs	24 11 03	11 40 hrs	720	12 00	1440 00	24 00	3 6420	3 1590	0 483	483.00	0 6820	4336	110
3	24 11 03	13.00 hrs	25 11 03	01 00 hrs	720	12 00	2160 00	36 00	3 1590	2 7333	0.426	425.70	0.5518	4723	120
4	25 11 03	02.00 hrs	25 11 03	14.00 hrs	720	12 00	2880 00	48 00	2 7333	2.4000	0 333	333.30	0.5022	4063	103
5	25.11.03	15.00 hrs	26.11 03	03 00 hrs	720	12 00	3600 00	60 00	2 4000	2 1600	0.240	240 00	0.4340	3386	86
6	25 11 03	04 00 hrs	27 11 03	16 00 hrs	720	12 00	4320 00	72 00	2 1600	1.9640	0.196	196 00	0 3472	3456	88
7	27 11 03	17 00 hrs	28 11 03	08.00 hrs	900	15 00	5220 00	87 00	1 9640	1.8350	0 129	129 00	0.2821	2240	57

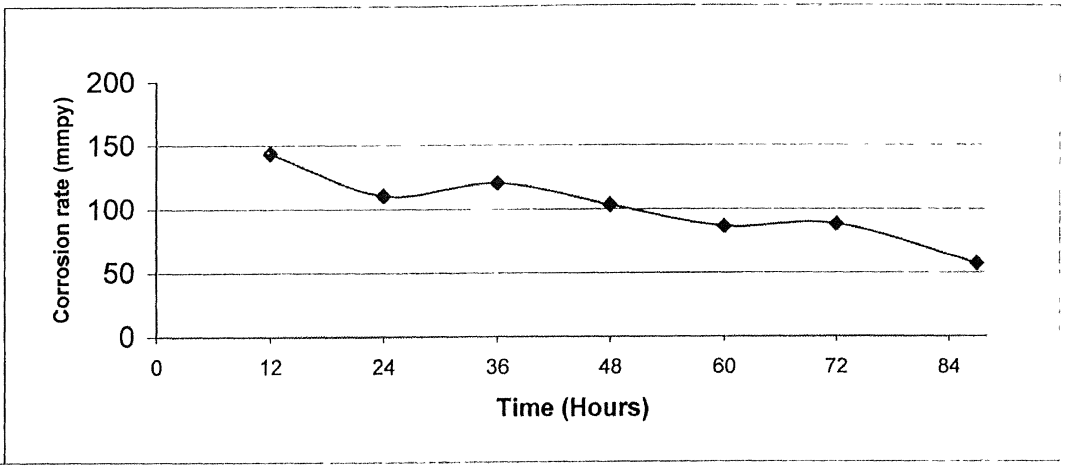

Table C 10 **Short term immersion testing done on 0.05% mild steel sample**

date 10.10 03 **COMPOSITION (in Wt%) = Fe- 0.05%C**

Elect 0 5N **Area of the specimen exposed =** 0 185225 Sqinches

Sl No	Date of experime	Starting time in hours	Time when reading was taken	Exposure time (t) in mts	Exposure time (in hrs)	Cumulative exposure time in mts	Cumulative exposure time in hrs	Intitial wieght (g)	Wt at time t (g)	Weight change in gms	Change wt in mg	Exp area specimen in sqinch	Corrosion rate m/year	Corrosion rate mmpy
1	09 10.03	11 00 am	11 45 am	45	0 75	45.00	0 75	0 3385	0.3383	0.0002	0 20	0 185225	98	2
2	09.10 03	12 00 am	12.50 pm	50	0 83	95 00	1 35	0.3383	0.3382	0.0001	0 10	0.185225	44	1
3	09 10.03	01.00 pm	01 50 pm	50	0 83	145 00	2 25	0 3382	0 3380	0.0002	0 20	0.185225	88	2
4	09 10.03	02.00 pm	02 50 pm	50	0.83	195 00	3 15	0.3380	0.3378	0 0002	0.20	0.185225	88	2
5	09.10 03	03.00 pm	03 50 pm	50	0 83	245.00	4.05	0.3378	0 3376	0.0002	0.20	0 185225	88	2
6	09 10 03	04.00 pm	04 50 pm	50	0 83	295.00	4.55	0 3376	0 3375	0.0001	0 10	0.185225	44	1
7	09.10.03	05.00 pm	05.50 pm	50	0 83	345 00	5.45	0 3375	0.3373	0.0002	0.20	0.185225	88	2
8	09 10 03	06.00 pm	06.50 pm	50	0 83	395.00	6.35	0.3373	0 3372	0.0001	0 10	0.185225	44	1
9	09 10.03	07 00 pm	07 50 pm	50	0 83	445.00	7.25	0.3372	0 3371	0.0001	0.10	0.185225	44	1
10	09.10 03	08 02 pm	08 50 am	48	0.80	493.00	8.13	0.3371	0 3370	0.0001	0.10	0.185225	46	1
11	09.10.03	09.00 pm	09.50 am	50	0.83	543.00	9.03	0.3370	0.3368	0.0002	0.20	0.185225	88	2
12	09.10.03	10.00 pm	10.50 pm	50	0 83	593.00	9.53	0.3368	0.3366	0.0002	0 20	0.185225	88	2
13	09.10 03	11 00 pm	11 50 pm	50	0 83	643.00	10.43	0.3366	0 3365	0 0001	0 10	0.185225	44	1

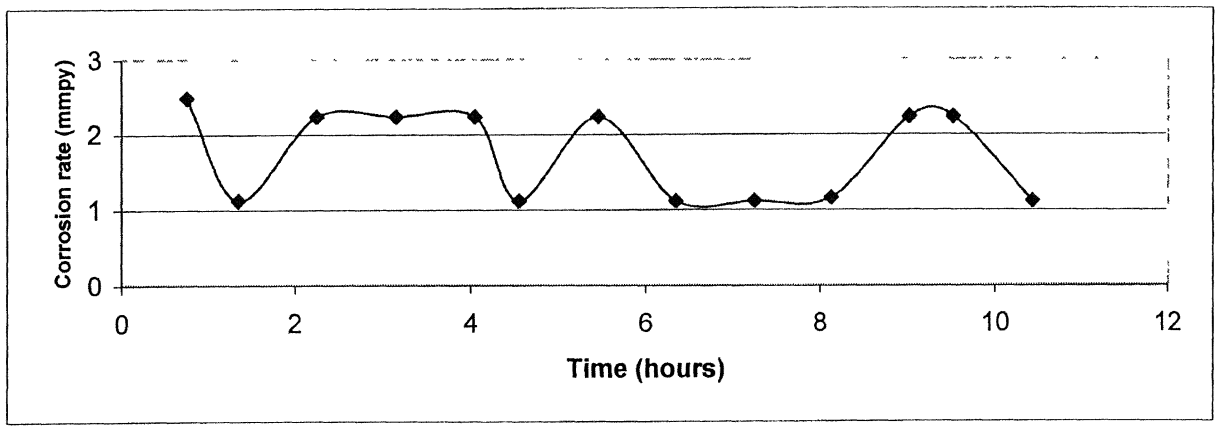

APPENDIX D

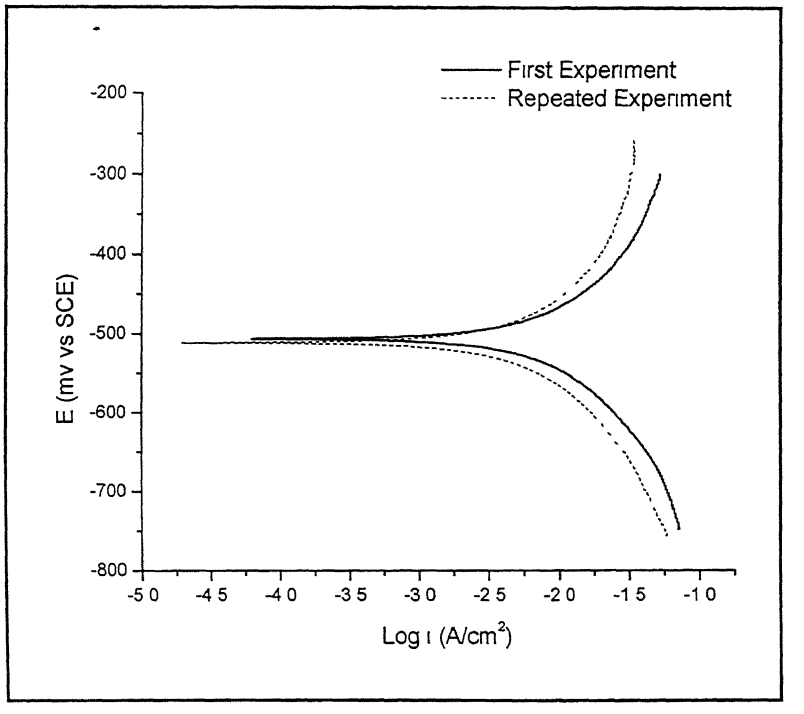

Figure:D-1 .Tafel curves of rolling plane of Fe-20.0Al-2.0C (ESR74) alloy showing repetition of results on duplication of the experiment.

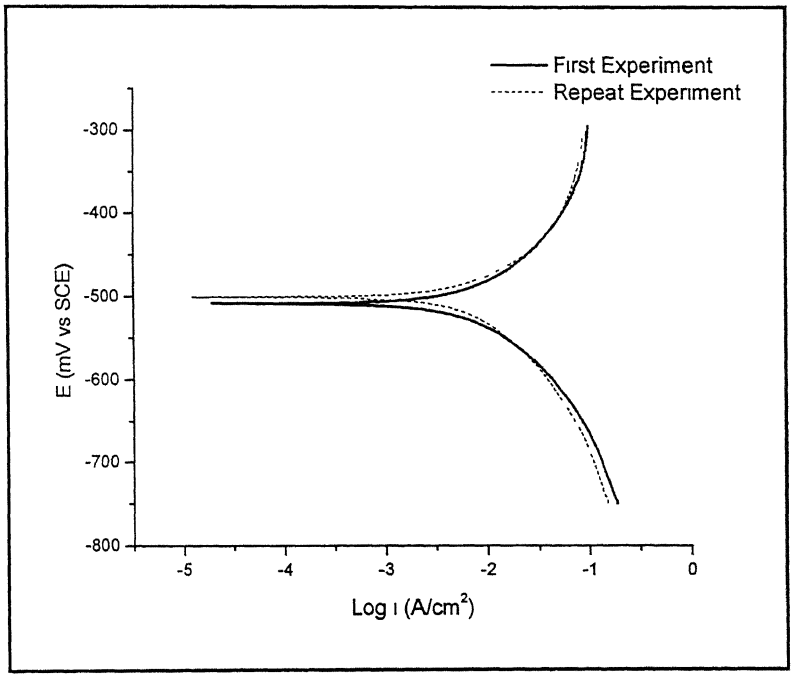

Figure:D-2. Tafel curves of rolling plane of Fe-18.5Al-3.6C (ESR127) alloy showing repetition of results on duplication of the experiment.

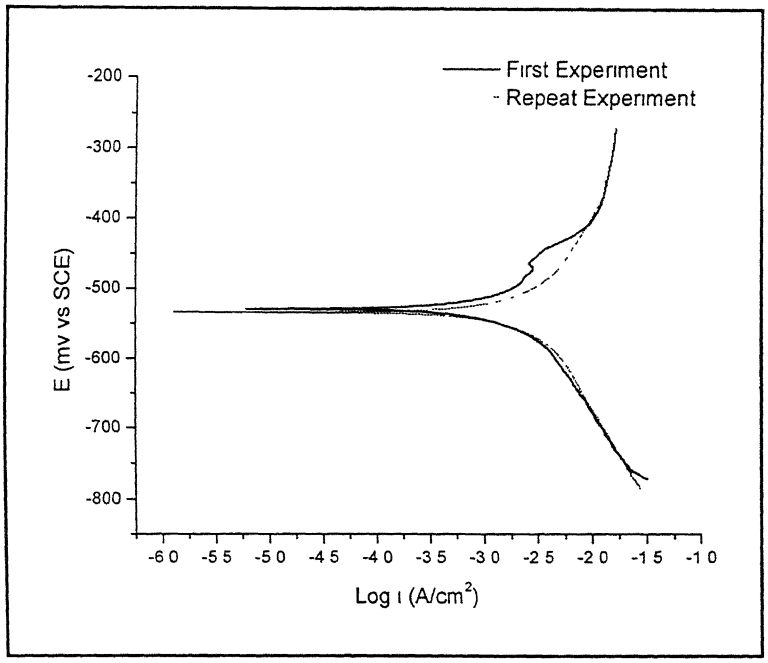

Figure:D-3. Tafel curves of rolling plane of Fe-19.2Al-3.3C-0.07Ce (ESR137) showing repetition of results on duplication of the experiment

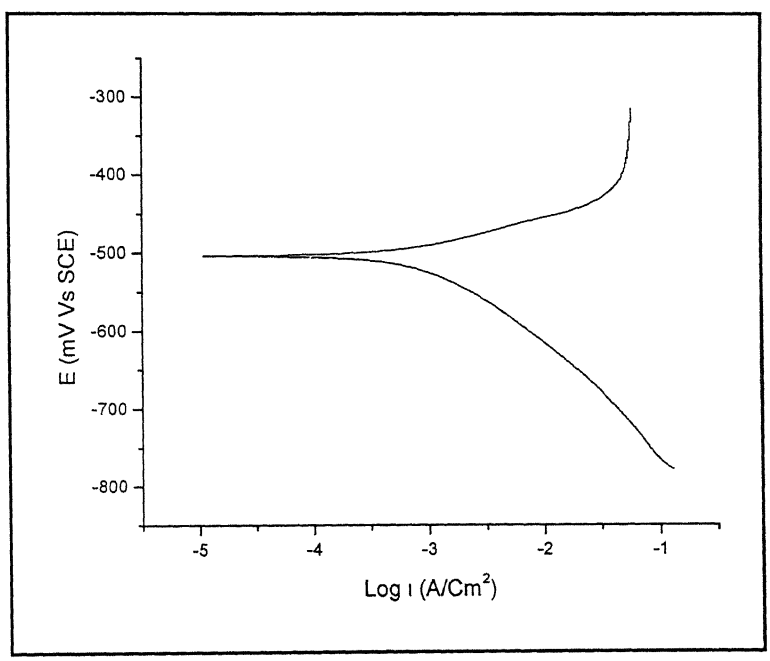

Figure:D-4. Tafel curves of long transverse plane of Fe-19.2Al-3.3C-0.07Ce (ESR137).

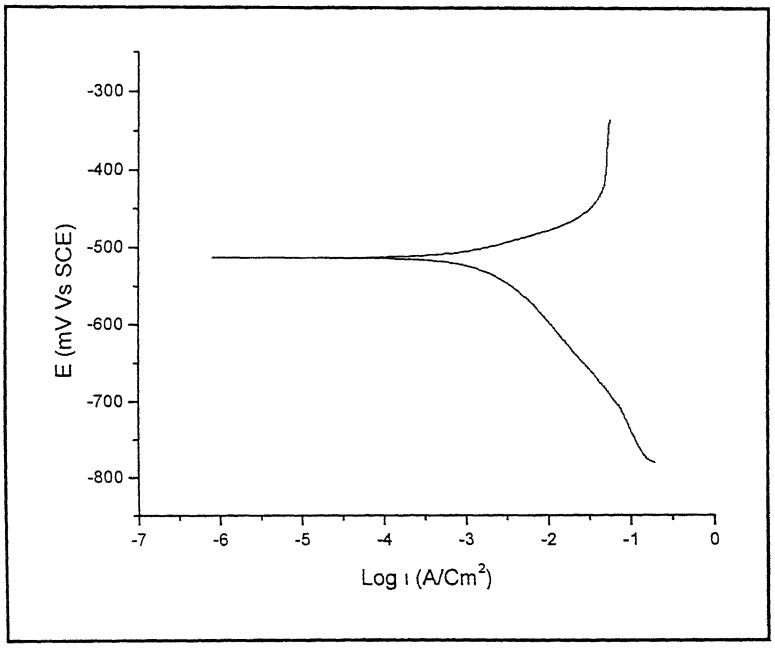

Figure:D-5 Tafel curves of short transverse plane of Fe-19.2Al-3.3C-0.07Ce (ESR137).

APPENDIX E

APPENDIX E

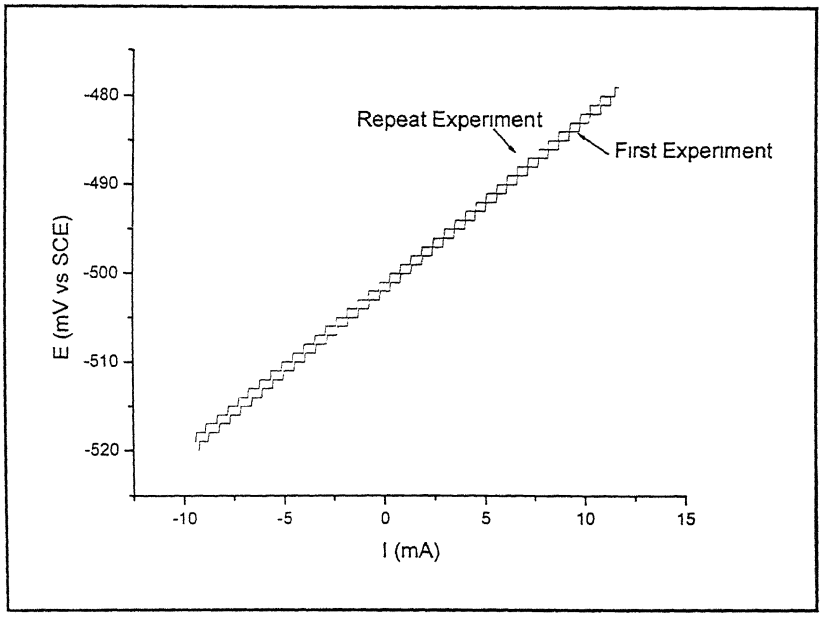

Figure E -1 Linear polarisation curves of ESR127 (Fe -18.5Al-3.6C) sample showing agreement of results on repetition of experiment.

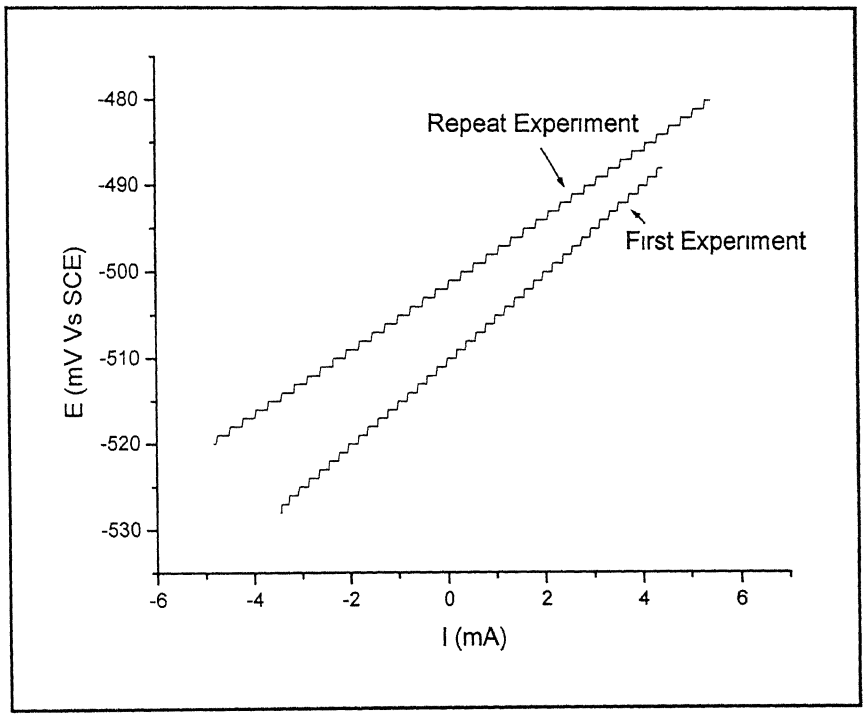

Figure E-2 Linear polarisation curves of ESR74 (Fe -20.0Al-2.0C) sample showing agreement of results on repetition of experiment

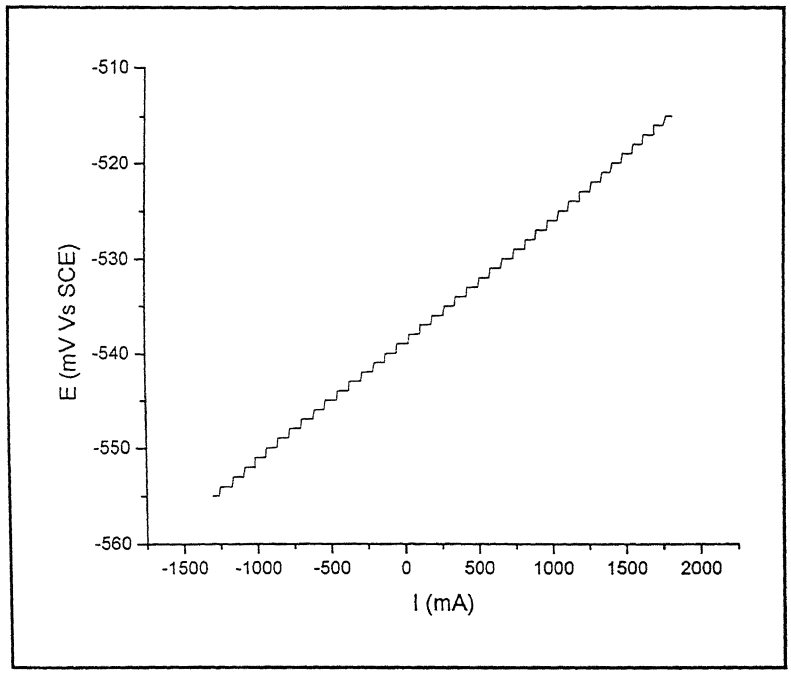

Figure E -3 Linear polarisation curves of rolling direction of ESR137 (Fe-19.2Al-3.3C-0.07Ce) sample

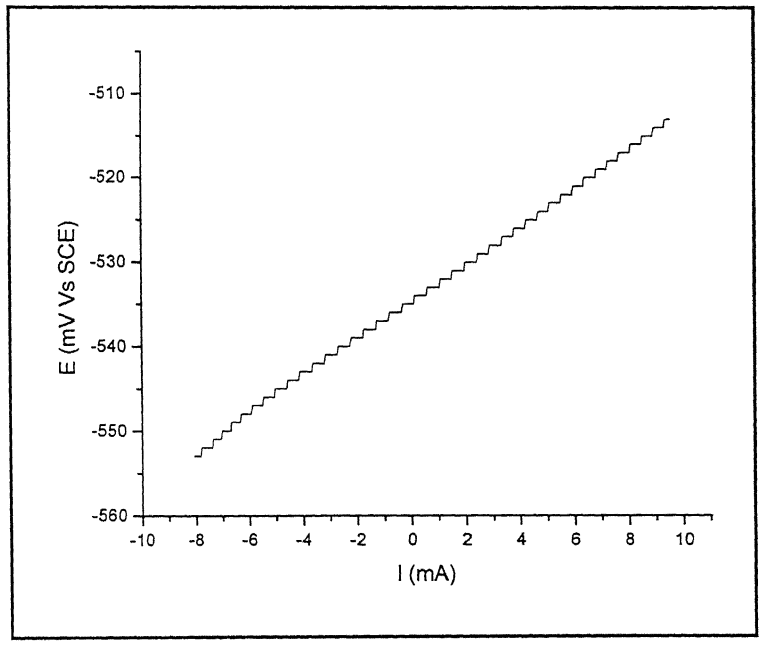

Figure E -4 Linear polarisation curves of short transverse direction of ESR137 (Fe-19.2Al-3.3C-0.07Ce) sample.

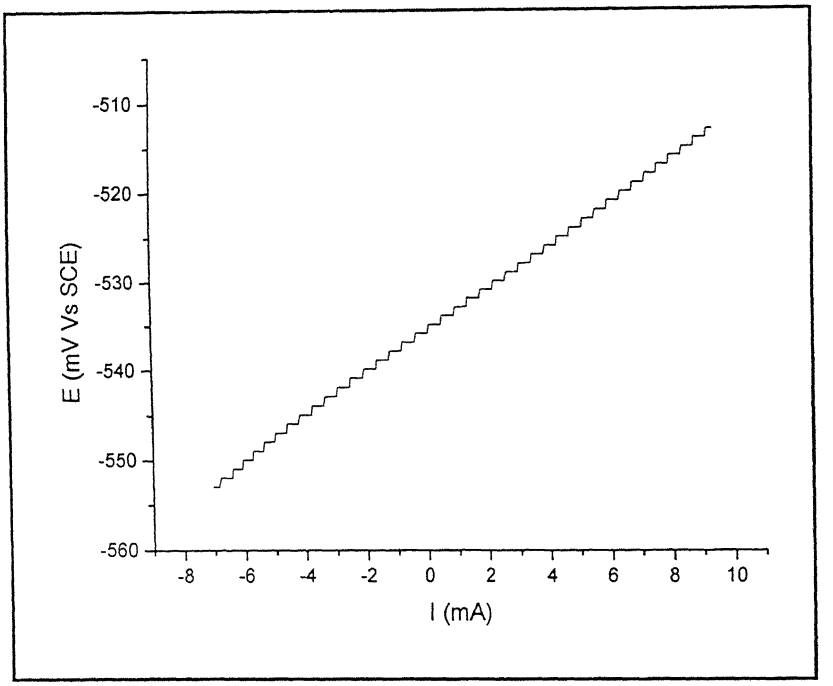

Figure E -5 Linear polarisation curves of long transverse direction of ESR137 (Fe-19.2Al-3.3C-0.07Ce) sample.